STRENGTHENING OF GLASS BY SOL-GEL COATINGS

by

BRIAN DAVID FABES

S. B., Materials Science and Engineering
Massachusetts Institute of Technology
(1984)

Submitted to the Department of Materials Science and Engineering in Partial Fulfillment
of the Requirements of the Degree of Doctor of Philosophy in Ceramics
at the
Massachusetts Institute of Technology
February 8, 1988

Signature of Author _____
Department of Materials Science and Engineering
January 8, 1988

Certified by _____
Donald R. Uhlmann
Thesis Supervisor

Accepted by _____
John B. Vander Sande
Chairman, Departmental Committee on Graduate Students

MASSACHUSETTS INSTITUTE OF TECHNOLOGY
MAR 28 1988
LIBRARIES

Strengthening of Glass by Sol-Gel Coatings

by

Brian David Fabes

Submitted to the Department of Materials Science and Engineering on January 8, 1988
in partial fulfillment of the requirements for the degree of
Doctor of Philosophy in Ceramics

ABSTRACT

The use of alkoxide coatings to increase the fracture strength of oxide glasses has been investigated. Increases in the fracture strength of silica glass to as much as 2.5 times the strength of uncoated glass have been achieved with this novel technique. In an effort to understand the mechanism of strengthening, chemical parameters, such as degree of hydrolysis and solution pH have been studied. These studies have lead to the development of a fracture mechanics model, wherein the densified coating provides a mechanical bridge behind the advancing crack tip. Based on this model, an expression which relates the fracture strength to the original flaw size, shape, and oligomer size has been derived. The presence of a large residual tensile stress, even after firing to 1000°C, is indicated. This stress severely limits the strengthening obtainable with the sol-gel strengthening technique. The residual stress also makes sol-gel strengthened glass highly susceptible to stress corrosion and, as a result, to static fatigue. In addition to the residual stress, the chemical nature of the surface and the method of producing flaws are shown to be important in the strengthening process. The potential for practical application of this strengthening technique is discussed. Finally, the use of sol-gel derived oxynitride films to provide abrasion resistance to already strengthened glass is discussed and investigated. The effectiveness of these hard coatings has been shown to be severely limited by the structural, rather than chemical, nature of the coating.

Thesis Supervisor: Prof. D. R. Uhlmann
Cabot Professor of Materials Science

Table of Contents

List of Figures

List of Tables

Acknowledgements

After three years of work, the list of people whom I would like to thank is extensive. I hope that the number of people deserving recognition will not diminish the sincerity of my appreciation of each one's contribution.

Buzzy Dale, Tricia Majkowski, Linda Kim, Dave McClurg, Eugenie Uhlmann, Kelly Simmons, Heinz Kochling, MaryBeth Macphee, Gillian Brown, and Jim Bevalacqua, all worked in the lab on various aspects of this project. Much of the data presented in the thesis is a result of their efforts. I thank them for their help, and I hope that whatever they learned while working in the lab is as useful to them as their efforts were to me.

My friends and colleagues - Brian Zelinski, Bill Doyle, and Lee Silverman, - deserve special thanks for their interest in my work, joint participation in many experiments, insightful (and often upsetting) comments and, most of all, for their friendships.

There has probably never been a graduate student granted more freedom to explore varying interests than I. This is the result of my advisor, Don Uhlmann, whose intelligence, support, generosity, warmth, and enthusiasm has always shortened the distance between us.

Many people in the Department have been helpful in a variety of ways over the last few years. Three stand out: John Martin, with whom I have collaborated on a large amount of surface science work (most of which is not included in this thesis), Prof. Yet-Ming Chiang, who originally suggested the idea of quantifying the strengthening effects discussed in the thesis, and Linda Sayegh who, on numerous occasions, has helped with administrativce details, guidance, and warm encouragement.

This work was funded by the International Partners in Glass Research. I am grateful to them - especially Pete Vergano, Jim Poole, and Dave Alderson - for their continued support, even when they felt that continued funding was more in my best interest than in theirs.

And as always, my greatest indebtedness is to my Mother, Father, Ellen and Cathy.

I. Introduction

1.1 Sol-Gel Processing

Traditional ceramic processing techniques, such as melting or sintering of powders, evolved almost entirely from physical approaches to materials processing.[1] Recently, however, attention has been paid to ceramic processing techniques which are based on chemical approaches as well.[2,3 e.g.] These new "sol-gel" techniques, which in principle allow for the building up of materials from the molecular level, have opened up a wide range of possibilities for designing and fabricating glasses and ceramics with novel combinations of properties.

Scientifically, sol-gel processing may produce radical changes in our thoughts about some of the oldest materials known. Glass, for instance, is sometimes defined as "an inorganic product of fusion." This definition, however, is based on a processing step, and not on the material itself. Using sol-gel techniques, silica glass has been produced without heating to the glass transition temperature, let alone melting.[3] Technologically, many potential applications have been proposed in the literature.[4-8] These applications include the production of (1) fine ceramic powders with narrow particle size distributions and chemical homogeneity; (2) glasses and ceramics with novel compositions and microstructures and hence properties; (3) materials with very high porosity; (4) extremely pure materials; and (5) novel ceramic coatings for optical, electronic, magnetic, and mechanical applications.

Of all the potential applications, coatings are by far the most natural. Other applications are often limited by two problems. First, large stresses develop during the

drying and sintering of monolithic samples. These stresses often lead to cracking which results in the destruction of the ceramic. Second, the precursors, often metal alkoxides, are generally quite expensive. Coatings, on the other hand, are less likely to crack because of the strong bonds formed with the substrate and their small thickness and concomitant effect on drying stresses; and the small amounts of material needed to produce a thin coating minimize the importance of precursor price. Moreover, since sol-gel processing involves the use of low viscosity solutions, coatings can be easily applied by a variety of techniques such as dip coating, spray coating, and roller coating. Finally, since so many bulk properties depend on the surface condition, there is great potential for altering the properties of materials with coatings.

Applications of sol-gel derived coatings already exist in the optical[9] and electronic[10] industries. And since the mechanical strength of brittle materials is controlled by surface conditions, it seems reasonable that sol-gel coatings might find applications in novel processes for increasing the strength of glasses and ceramics.

1.2 Alkoxide Chemistry

The hydrolysis and polycondensation of metal alkoxides is the most common sol-gel approach to producing glasses and ceramics. In the most extensively studied system, for example, silica glass can be formed by reacting tetraethoxysilane (TEOS) with water and a catalyst. TEOS is a clear, colorless liquid which contains 29 % silica by weight. Because TEOS and water are not miscible, reactions are usually carried out in at least 30 vol % of a mutual solvent, such as methanol, ethanol, isopropanol, or THF.

The first step of the reaction involves hydrolysis (1.1) of a metal alkyl bond to form a silanol ligand:

$$\equiv Si - OEt + H_2O \; <\cdots> \; \equiv Si - OH + EtOH \qquad 1.1$$

Next, a silanol group can condense with an alkoxide group (1.2) or another silanol group (1.3) to produce a siloxane linkage:

$$\equiv Si - OH + EtO - Si \equiv \; <\cdots> \; \equiv Si - O - Si \equiv + EtOH \qquad 1.2$$

$$\equiv Si - OH + HO - Si \equiv \; <\cdots> \; \equiv Si - O - Si \equiv + HOH \qquad 1.3.$$

Continued condensation leads to an increase in the density of siloxane crosslinks until the solution eventually becomes a rigid gel. Heating the gel to drive off residual organic content produces a porous oxide which can then be sintered to form a dense silica glass. The firing temperature needed to form a dense glass varies, depends on the reaction conditions, but is usually around 1050 C.[15,16] (The lowest reported densification temperature comes from Nogami and Moriya,[14] who claim to have densified acid catalyzed TEOS derived silica at 700 C.)

Changes in the catalyst, solvent, water concentration, and temperature have been shown to affect the mechanisms, rates, reversibility, and extents of reactions 1.1 - 1.3,[11, 14-17, e.g.] which in turn alters a variety of characteristics of the final materials. For example, varying the catalyst concentration changes the solution pH, which significantly affects the hydrolysis reaction mechanism. Under acidic conditions, the reaction proceeds via an electrophillic interaction.[15,18] As depicted in Figure 1.1a, the protons of a hydronium ion are attracted to the electron rich oxygen atoms of a TEOS molecule. Simultaneously, a partial bond forms between the water oxygen and the silicon atom to

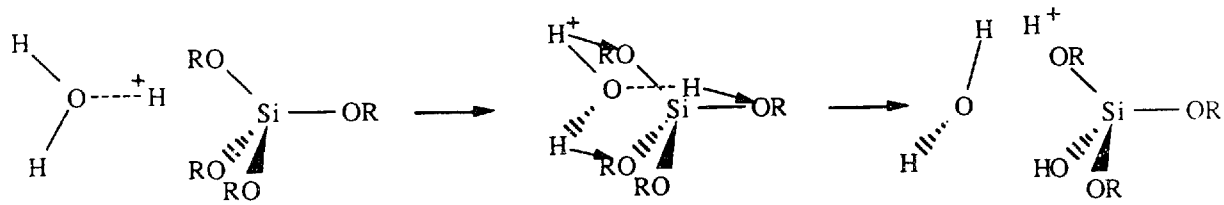

a.

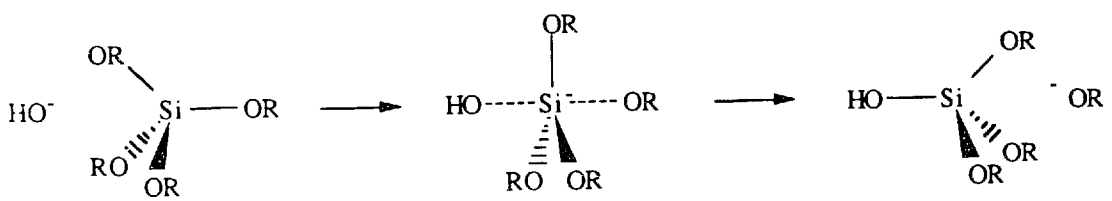

b.

Figure 1.1: Models of hydrolysis of TEOS under (a) acidic and (b) basic conditions. (After 15)

form a quinquevalent transition state, which decomposes either into an alcohol and a hydrated TEOS molecule, or back into the water and unhydrolyzed TEOS molecules.[15,18] The electrophillic nature of this reaction means that the most basic, i.e. electron donating, molecules are hydrolyzed preferentially. Thus, the tetraalkoxide (TEOS) is hydrolyzed faster that the trihydroxydialkoxide, which is hydrolyzed faster than the dialkoxidedihydroxide, etc. As a result, if we ignore the effects of condensation, the formation of monosilicic acid, $Si(OH)_4$, is not favored when TEOS is hydrolyzed with small amounts of water under acidic conditions. Instead, all TEOS molecules should tend to be evenly hydrated with roughly the same number of silanol groups before condensation begins.

Under alkaline conditions, the hydrolysis of TEOS proceeds by a nucleophillic substitution reaction.[15,18] As pictured in Figure 1.1b, a negatively charged hydroxide ion attacks the positively charged silicon atom, producing a tetravalent intermediate. To provide for maximum charge separation, the opposite side ethoxide ion leaves, producing an inverted, hydrated TEOS molecule and an ethoxide ion which is quickly reprotonated by a water molecule to regenerate the hydroxide ion.[15] The nucleophilic nature of this hydrolysis reaction means that the most acidic molecules are favored for hydrolysis, so that a the susceptibility of a molecule to hydrolysis increases as its extent of hydrolysis is increased. As a result, if we again ignore condensation, the formation of monosilicic acid is more favored than the formation of evenly hydrolyzed species when TEOS is hydrolyzed in basic conditions, even with small water concentrations.

It is important to keep in mind that these reaction mechanisms only bias the systems toward one morphology or another;[15] and changes in other reaction parameters, such as the reaction rate, can affect polymer development. The condensation rate, for

example, goes through a minimum around pH = 2. At this pH, the condensation reaction is so slow that hydrolysis may go to completion (forming monosilicic acid if enough water is used) before any condensation takes place. The water concentration, via LeChatelier's principle, can also bias the system toward one extreme or another; at high water concentrations, hydrolysis is heavily favored over condensation, so that monosilicic acid formation is favored under both acid and alkaline conditions. As the water concentration is reduced, the differences discussed in the two preceding paragraphs become more pronounced.

Under both acidic and basic conditions, condensation is forced to build on the molecules produced during hydrolysis. Low-water, acid generated monomers therefore tend to polymerize into lightly crosslinked, relatively linear species. High water or alkaline generated monomers, on the other hand, often condense into highly crosslinked, relatively compact particles. As mentioned above, such changes in polymer morphology can, in turn, affect material characteristics such as firing temperatures. The highly crosslinked colloids formed under alkaline conditions, for example, do not pack as well as, and form more porous gels than the lightly crosslinked linear arrays formed during acidic reaction.[11,16] As a result, the temperature needed to densify low water, acidic gels has been reported to be as low as 700 °C,[11] while temperatures of well over 1000 °C are needed to densify high pH, high water content gels.[11,16]

Many other material characteristics, such as primary particle size, particle size distribution, oxide content, vibrational spectra, and residual carbon content, are affected by the reaction condition changes outlined above,[11, 14-17] so that there is tremendous variability in the products formed, even in a simple, one component system such as silica.

While this variability can be a complicating factor, especially in multi-component materials, it is also one of the advantages of using sol-gel processing techniques.

The processing steps discussed above are radically different from the traditional melt process which must be carried out at well over 1700 °C in the case of SiO_2.[19] Nevertheless, many physical properties - such as density, refractive index, hardness, thermal expansion coefficient, and vibrational spectra - have been examined; and very little difference is noticed between fully densified melt derived and alkoxide derived silica.[11-13] One factor that makes the alkoxide technique particularly interesting, though, is the ability to form siloxane bridges not only between molecules in solution but also between the solution and an oxide surface. As depicted schematically in Figure 1.2, condensation between a solution silanol and a substrate silanol (or a solution alkyl and a substrate silanol) can lead to the formation of a strong covalent bond between the coating and substrate to produce a well bonded coating. Such coatings have been used for optical applications,[5] oxidation resistance,[20] microelectronics planarization,[21] and glass heat-sealing.[22]

1.3 Glass Strength

1.3.1 Fracture Mechanics

Thermodynamically, a material will fracture whenever the stored elastic strain energy released surpasses the increase in surface energy due to the creation of new surfaces. On this basis, we can calculate the theoretical strength of solids by setting the stored energy per volume, W, equal to twice the surface energy, γ, (assuming two surfaces are produced)

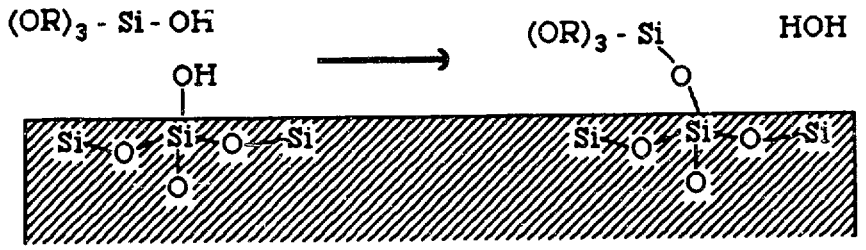

Figure 1.2: Schematic representation of primary bond formation between alkoxide coating solution and oxide substrate.

$$W = \int_0^x \sigma \, dx = 2\gamma \qquad 1.4,$$

where x is the separation of the surfaces and σ is the elastic stress. For purely elastic materials such as glass, we can apply Hooke's Law,

$$\sigma = \varepsilon E \qquad 1.5$$

where ε is the strain and E is Young's modulus. Since the molecular forces act over a distance about equal to the atomic separation, a_o, the strain can be written

$$\varepsilon = \frac{x}{a_o} \qquad 1.6.$$

Differentiating 1.5 and 1.6 and substituting into 1.4 gives

$$W = \frac{a_o}{E} \int_0^\sigma \sigma \, d\sigma = \frac{a_o \sigma^2}{2E} = 2\gamma \qquad 1.7,$$

so that the theoretical strength, σ_{th}, is

$$\sigma = \sqrt{\frac{4\gamma E}{a_o}} \qquad 1.8.$$

Inserting typical values[23] of $E=3\times10^{11}$ dynes/cm^2, $\gamma=10^3$ ergs/cm^2, and $a_o=3\times10^{-8}$cm, equation 1.8 predicts a strength of about 1-2 $\times10^6$ psi for silicate glasses. Such strengths are seldom observed in practice, however, as most commercial glasses are two to three orders of magnitude weaker than the theoretical strength.

It is generally agreed that this discrepancy between the calculated and actual strengths is a result of small flaws which act as stress concentrators. Based on the work of Griffith[24] and Inglis,[25] for a surface flaw of length c in an isotropic body under an applied uniaxial tension σ_{app}, the actual stress felt at the tip of the flaw, σ_{tip}, is given by:

$$\sigma_{tip} = \sigma_{app}\sqrt{\Omega c} \qquad 1.9,$$

where Ω is a geometric term which is roughly proportional to the inverse radius of curvature of the flaw tip. That is, the stress felt at the tip of a flaw is amplified beyond the applied stress by the factor $(\Omega c)^{1/2}$. Fracture can therefore occur before the overall applied stress reaches the theoretical strength.

Combining equations 1.8 and 1.9, the fracture stress, σ_f, of a flawed body becomes:

$$\sigma_f = \sqrt{\frac{4\gamma E}{\Omega c a_o}} \qquad 1.10.$$

It is now apparent that the strength of glass is **not** an intrinsic material property. Ω and c are external variables which make the strength a strong function of the mechanical condition of the surface.

Since it is often desirable to discuss the strength of a material in terms of an intrinsic parameter, use is often made of the stress intensity factor, K_I, [§] which is defined as

[§] The subscript I refers to the opening mode, or mode I, crack tip deflection. Although forward sliding, mode II, and sideways tearing, mode III, deformations are also possible, the geometric constraints imposed by the test conditions used in this work will allow us to confine discussion to mode I deformation only.

$$K_I = \sigma_{app}\sqrt{\Omega c} \qquad 1.11.$$

By comparing equation 1.11 with equation 1.9, we see that the stress intensity factor is really just an alternative representation of the stress felt at the tip of a flaw. When this stress reaches the theoretical strength (Equation 1.8) fractures occurs. The stress intensity at which this happens is defined as the critical stress intensity, K_{Ic}, which, for the simple model presented here, is given by

$$K_{Ic} = \sqrt{\frac{4\gamma E}{a_o}} \qquad 1.12.$$

K_{Ic}, also known as the toughness, T_o, is an intrinsic material parameter.

For silicate glasses, $K_{Ic} \approx 0.75$ MPa$\sqrt{m}$, and for crystalline ceramics, K_{Ic} is usually in the range of 3-5 MPa$\sqrt{m}$. It is interesting to note that for metals, which have theoretical strengths roughly comparable to glass, the occurrence of plastic flow at the crack tip greatly increases the effective surface energy term in equation 1.12, and toughnesses can range up to almost 500 MPa$\sqrt{m}$. This large value of K_{Ic} makes metals preferable to glass in many engineering applications, since flaws can grow to macroscopic, routinely detectable sizes (often on the order of millimeters) before fracture occurs. In ceramics, where plastic flow is negligible, critical flaw sizes are usually in the micron range. Such flaws are difficult if not impossible to detect by routine inspection.

1.3.2 Stress Corrosion

Stress corrosion is the process by which flaws grow subcritically under an applied stress. The stress corrosion process is responsible for both "static" fatigue, wherein the strength of glass is diminished with time under load, and "dynamic" fatigue, wherein glass strength is a function of the loading rate. The process is generally believed to be the result of stress assisted chemical attack of water on siloxane bridges, which weakens the glass at the flaw tip and results in subcritical crack growth.

One of the more advanced mechanistic models of the stress corrosion process has been be described by Michalske and Freiman[26] in terms of a three-step process (See Figure 1.3). In the first step, the lone pair of electrons on a water oxygen atom interact with a bridging silicon atom. Simultaneously, a hydrogen bond is formed between this oxygen atom and an adjacent bridging oxygen. In the second step, proton transfer to the bridging oxygen and electron transfer to the silicon atom create two new bonds, while the bridging siloxane bond is broken. Finally, proton transfer to the (broken) bridging oxygen results in the formation of two new surface silanol groups. Atomistically, the reaction is favored at crack tips because of the concentration of stress fields at flaw tips when a sample is put under tension. These stresses decrease bonding orbital overlap, leaving the silicon atom more susceptible to nucleophilic attack by oxygen lone pairs.[26] This model successfully accounts not only for the dependence of crack velocity on applied stress (Figure 1.3) but also for the insensitivity of crack velocity to the removal of

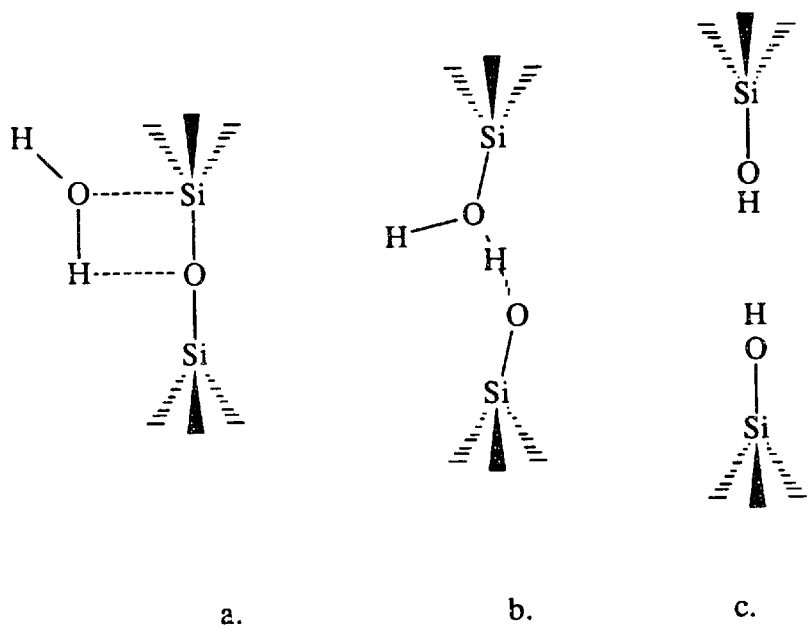

Figure 1.3: Schematic representation of siloxane breaking stress corrosion reaction. In the first step, a, the water molecule is adsorbed onto the siloxane bridge. In step b, simultaneous electron and proton transfer reactions occur, creating two new bonds and breaking the siloxane bridge, resulting in the formation of two new surface silanol groups, c. (After 26)

reaction products and for the effectiveness of ammonia, hydrazine, and formamide, and ineffectiveness of carbon monoxide, acetonitrile, and nitrobenzene in accelerating crack growth.

Wiederhorn[27,28] studied the dependence of slow crack growth in a variety of glasses on stress intensity, atmospheric water content, temperature, and pH. His results for soda-lime-silicate glass are shown in Figure 1.4. For a given temperature, pH, and water concentration, three regions of velocity are found. In the first region, at relatively low stress, the crack velocity, v, is limited by the rate of the stress corrosion reaction (Figure 1.3) and is proportional to the applied stress,

$$v = a_2 \exp\left(\frac{nK_I}{RTK_c} - \frac{E_2}{RT}\right) \qquad 1.13$$

where a_2 and n are material / environment constants, which increase with the water concentration; E_2 is an empirical measurement of the zero stress activation energy for the corrosion reaction; K_I and K_c are the stress and critical stress intensity factors, respectively; and R and T represent the gas constant and absolute temperature, respectively.[29] In the second region, the crack velocity is limited not by the chemical corrosion reaction but by the diffusion of water to the crack tip. As a result, crack propagations in region II is still dependent on overall water content, but is independent of the applied stress. Finally, in the high stress third region, cracks move so fast that the stress corrosion reaction is unable to keep up with the advancing crack front. The onset of region III occurs, by definition, at the critical stress intensity, and reflects the ultimate strength of the load-bearing siloxane bonds.

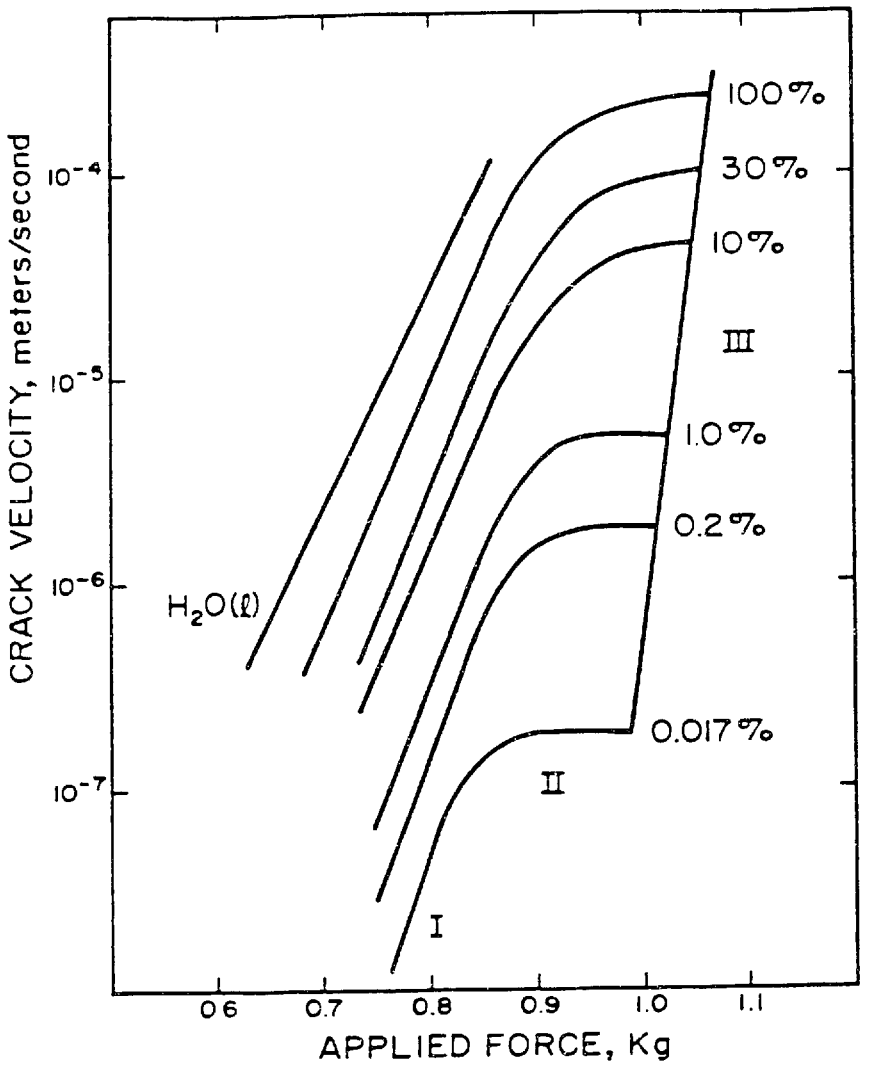

Figure 1.4: Crack velocity in soda-lime-silicate glass as a function of the applied load for a variety of atmospheric moisture contents. (From ref. 26)

In addition to exponential crack growth law, Equation 1.13, subcritical crack growth in region I has often been described in terms of a power law,[30]

$$v = a_1 (\frac{K_I}{K_c})^N \exp(-\frac{E_1}{RT}) \qquad 1.14,$$

where a_1 and N are material / environment constants. While this power law is often more convenient to manipulate than the exponential law, it is more empirical than the former equation, which can be loosely derived from a consideration of the kinetics of the stress corrosion reaction[26] Both equations have been combined with stress intensity equations (such as Equation 1.11) and integrated to solve for the time of failure at constant load (static fatigue) or the failure stress at a constant stress rate (dynamic fatigue). It is interesting that the two different equations can be used to describe so well the same phenomenon, even the same data.[29] This is discussed more fully in Appendix A.

1.3.3 Strengthening of Glass

The theoretical strengths of ordinary glasses do not very substantially from one type of glass to another. Hence, the most effective method of increasing the useful strength of glass is often to decrease the net stress felt at the most critical points, the flaw tips. Referring to equation 1.11, this can be accomplished by either reducing the applied stress, decreasing the flaw size, or altering the flaw geometry to reduce Ω. Almost all present-day strengthening techniques exploit one of the first two methods. The approximate maximum strengthening factors obtainable with most strengthening techniques are listed in Table 1.1.

Table 1.1: Extent by which glass can be strengthened by various treatments. (From 36)

Treatment	Approximate Maximum Strengthening Factor
Rapid Quenching	6
Ion Exchange	10
Surface Crystallization	17
Glazing (ref. 31)	3
Etching	30
Fire Polishing	200

Rapid quenching, ion-exchange strengthening, surface crystallization, and glazing all put a glass surface in a state of compression, and the interior in a state of tension. When such a sample is subjected to a macroscopic tensile stress, the residual stresses are added to the applied stresses to create a net stress profile such as shown in Figure 1.5. The exterior compressive stress can be quite effective in reducing the overall tensile stress felt by the tips of the microflaws, which exist near the surface because of their small size. The tensile stresses in the interior of the body is a drawback, however, since a flaw reaching into this region will find itself under the combined residual and applied tensile stresses, usually resulting in spontaneous failure.

Of these four techniques, rapid quenching is the least expensive to apply, although it is often difficult to quench complicated shapes evenly. Ion exchange strengthening, on the other hand, can be used to strengthen almost any shape, but is often unduly expensive, and is not effective if a body is to be used at elevated temperatures, since interdiffusion of the ions may result, which relieves the stresses built up by the cation size gradients. In addition, the high compressive stresses are present over only a very thin depth; so there is a greater risk of a flaw's reaching the interior tensile region. Surface crystallization is an effective technique in glasses whose crystalline products have a lower thermal expansion coefficient than the bulk vitreous phase. In these glasses significant surface compressive stresses can be introduced upon cooling, although closely controlled crystallization schedules are often necessary and crystallization often results in loss of transparency. Finally, for simple shapes which can be evenly coated, glazes can provide compressive stresses as high as of 25,000 psi and have been used to produce long-life ceramic tableware.[31] These low expansion thick coatings are difficult, however, to apply to complex shapes.

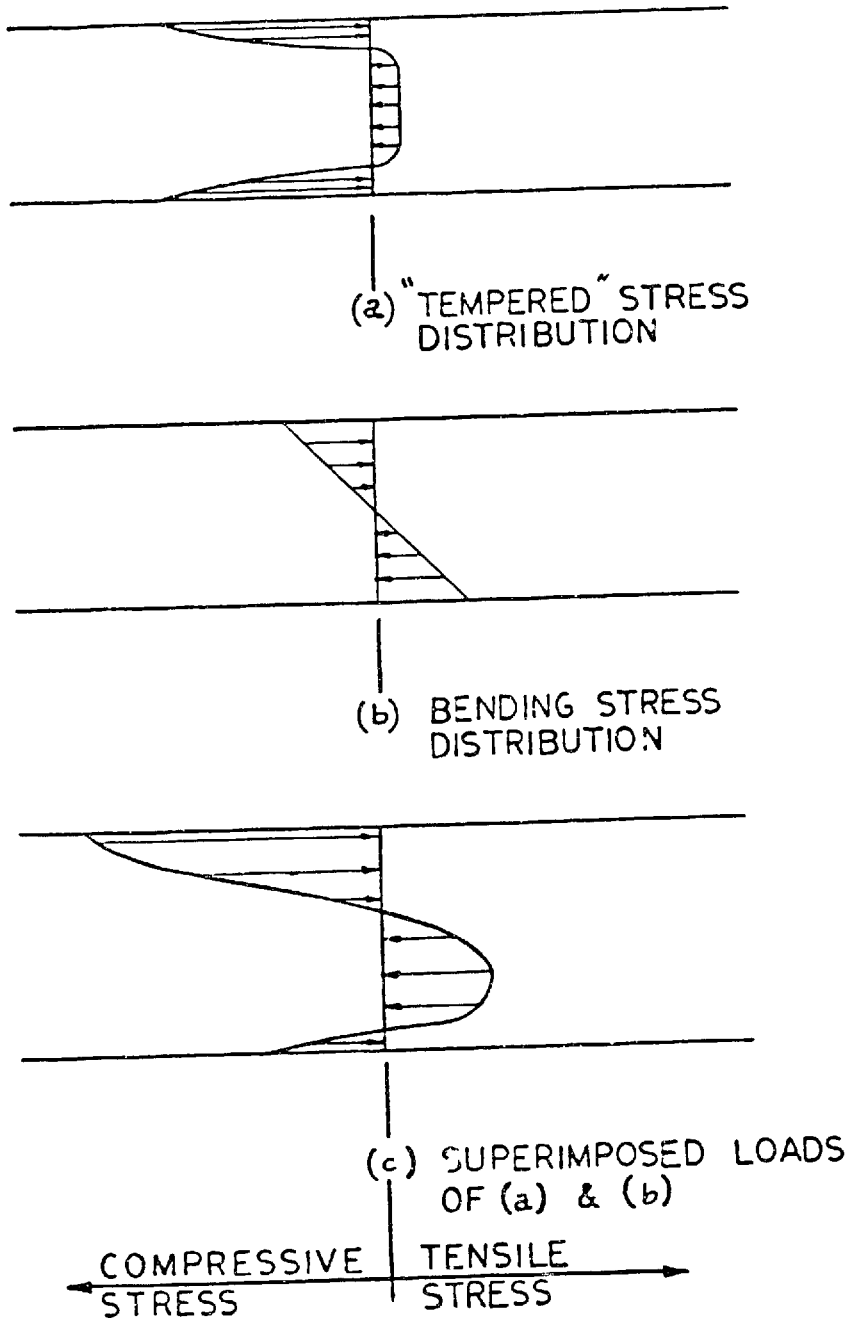

Figure 1.5: Superposition of (a) residual, and (b) applied stresses in a compressively stressed body to produce the net stress profile (c) (From 37).

In flame polishing and acid etching, surface flaws are eliminated from the glass body, resulting in high strengths (in the range of several hundred ksi). Glasses thus strengthened are highly susceptible, however, to the introduction of flaws after the strengthening treatment. Lightly touching etched rods, for example, reduces their strength by almost an order of magnitude.[33]

Finally, protective coatings can be of great use in increasing the practical strength of glass. These treatments are not listed in Table 1 because they do not actually increase the strength of a glass body. Instead, they prevent glass from weakening by protecting surfaces from the introduction of flaws. In the case of glass fibers, where protective, low coefficient of friction coatings can be applied immediately after fiber drawing, strengths approaching 10^6 psi can be maintained.[34]

In the case of glass containers, a two-step coating is generally used to guard against abrasion, primarily on the filling line. These coatings consist of a thin tin oxide film, known as the "hot-end" coating, on top of which an organic "cold end" coating is placed. The organic coating provides lubricity to the fresh glass surface, and the oxide coating improves the adherence of the cold-end coating, resulting in durable, longer lasting protection for the container. While these coatings are unquestionably helpful in preventing damage, their effectiveness is limited, since they are applied after the annealing lehr, when the strength of the container has already fallen from an as-pressed burst strength of 75,000 psi to about 8,000 psi.[35] (These coatings will be discussed in more detail in the next chapter.)

1.4 Sol-Gel Strengthening

The application of alkoxide derived coatings to glass surfaces represents a novel approach to glass strengthening. Such coatings seem particularly promising because of their potential for **both** strengthening already weakened glass by filling in existing microcracks **and** protecting against subsequent damage by altering the coating chemistry to produce abrasion resistant coatings and/or low thermal expansion coatings, all in one step.

The remainder of this thesis will focus mainly on the first possibility, strengthening weak glass by filling in microcracks. Approaches to providing abrasion resistance will be discussed in the appendices.

II. Influences of Thin Oxide Coatings on the Strength of Glass

Thin coatings (< 1μm) have been used, or have been suggested for use, in a number of methods for strengthening glass articles. In this chapter, four such methods - compressive stress coatings, moisture barriers to reduce fatigue, abrasion resistant coatings, and flaw healing coatings - will be discussed. We will see that sol-gel coatings have potential for application in all four of these methods.

2.1 Compressive Stresses

Coatings, in the form of glazes, are a common and effective method of improving the usable strength of glass; as mentioned in the preceding chapter, compressive stresses as high as 25,000 psi can be produced. Thin coatings, however, are seldom used to create large compressive stresses because the critical flaws in glass are generally larger than the 10,000 Å, and would extend into the tensile stress field of the base glass which is created by a thin coating under compression. This problem could be overcome simply by using a high coefficient of thermal expansion (CTE) coating which would put the substrate under compression. However, to create a substantial stress in the thicker substrate, a thin coating would have to be under tremendous tension.

In microelectronics fabrication, for example, thin coatings of silica, silicon-oxynitride, and silicon nitride have been used as diffusion barriers to prevent oxidation of the underlying silicon substrates.[38,39] As a result of CTE mismatch, these films can be under very high stress, up to 42 ksi,[40] which can cause the coating to crack.[41] The stress

felt in the thicker substrate is much milder; so that the main effect on the underlying silicon is the generation of dislocations, or sometimes bending if the wafer is particularly thin.[41] (For electronic applications, these happen to be important effects.)

For mechanical purposes, it would appear that compressive stresses could be generated in glass substrates by thin coatings, although the magnitudes of the stresses are expected to be small.

2.2 Moisture Barriers

Any coating which protects a glass surface from attack by water should be effective in strengthening the underlying glass by reducing, or eliminating the effects of stress corrosion. With the development of low-permeability polymers, thick (tens of microns) polymer claddings on fused silica optical fibers have been successfully used not only to protect pristine surfaces against abrasive damage, but also to protect against fatigue.[34, e.g.] While thinner polymer coatings are probably too water-permeable to be effective moisture barriers, thin ceramic coatings might be resistant enough to provide protection.

As mentioned above, thin coatings of silica, silicon-oxynitride, and silicon nitride have been used as diffusion barriers in the microelectronics field. Very little data are available on the fatigue behavior of such coated silicon, however, since static fatigue is not a critical issue for the inherently strong, polished substrates used in microelectronics fabrication. For glasses, it seems reasonable that such films could be of significant value in protecting corrosion-susceptible glasses from atmospheric moisture. This possibility

was suggested by Sokolova et al [42] to explain strengthening data on ZnO, Al_2O_3, and Fe_2O_3 coated glass.

Sokolova et al [42] coated flawed (17 ksi) soda-lime-silicate glass plates with aqueous solutions of Zn, Al, and Fe chlorides, acetates and nitrates. These coated plates were fired at temperatures between 300 °C and 650 °C, resulting in 0.1 μm oxide coatings. The samples were then broken in bending at a rate of ~12 ksi/sec. For plates coated with ZnO, a 70 % increase in bend strength was observed. Only minor strength increases were observed for the Al_2O_3 or Fe_2O_3 coated samples. Sokolova et al correlate this behavior with differences in the rate of reabsorption of water after heating; after heating to 300 °C and cooling to room temperature, very little water is reabsorbed onto ZnO coated glass. Al_2O_3 and Fe_2O_3 coatings, on the other hand, readily reabsorb moisture from the atmosphere. "It is well known that water lowers the strength of inorganic glasses two to threefold," they comment, "and therefore the partial removal of water from the surface of the glasses is a sort of reserve of strength." In other words, the ZnO coatings protect against fatigue by lowering the water content at the tip of an advancing crack. (The differences in moisture reabsorption between the ZnO, Al_2O_3 and Fe_2O_3 coatings are probably due to porosity variations which are hinted at by Sokolova.)

The correlation between strength and adsorbed water must be treated with caution, however, since strength tests were all conducted in the open atmosphere, where one would expect the water concentration at the crack tip to be much more sensitive to the humidity than to the amount of adsorbed water on the sample surface. (Recall Figure 1.4)

There does exist independent data which support of Sokolova et al's contention that thin oxide coatings provide resistance to fatigue is some data of Williams[43] on SnO_2 coated glass containers. Williams coated fresh, hot containers on-line with ~200 Å of

SnO_2 by a standard CVD process. His data are reproduced in Figure 2.1. Both the impact strength and bu[illegible]ength were improved by their coatings; but the impact strength was markedly reduced, eventually back down to the uncoated value, as the coating thickness was increased. The burst strength, on the other hand, increased with the coating thickness. Since a sample is under stress much longer for the bursting test than for the impact test , a coating which served to protect against fatigue would be more effective for the burst-tested samples (unfortunately, the reference does not contain quantitative data on the rate of pressure application). Again these data must be treated with caution, since frictional effects, such as an increased coefficient of friction (μ) for coated samples, could dominate the impact testing. In similar experiments by Southwick et al,[44] for example, where the coatings were shown to decrease μ, the impact strength was improved more than the burst pressure. Southwick has explained this effect by showing that the tensile stress imparted to a surface by a horizontally translating abrader is directly proportional to μ. Thus, unless the impact tester strikes the sample perfectly perpendicular to the surface, high μ samples will appear weaker on impact than will low μ samples.

In an effort to quantify the fatigue properties of coated glass, Davis et al [45] coated 200 gr Vickers indented soda-lime-silicate glass with 140 Å of SnO_2 using a CVD process very similar to that of Williams. Constant loads were then applied to the coated specimens, and the times to failure were measured. They found no statistical difference between the static fatigue characteristics of coated vs. uncoated samples.

In summary, it is likely that thin oxide coatings could be used to increase the strength of glass by providing a moisture barrier and decreasing the effects of stress corrosion. To date, however, such an effect has yet to be demonstrated conclusively.

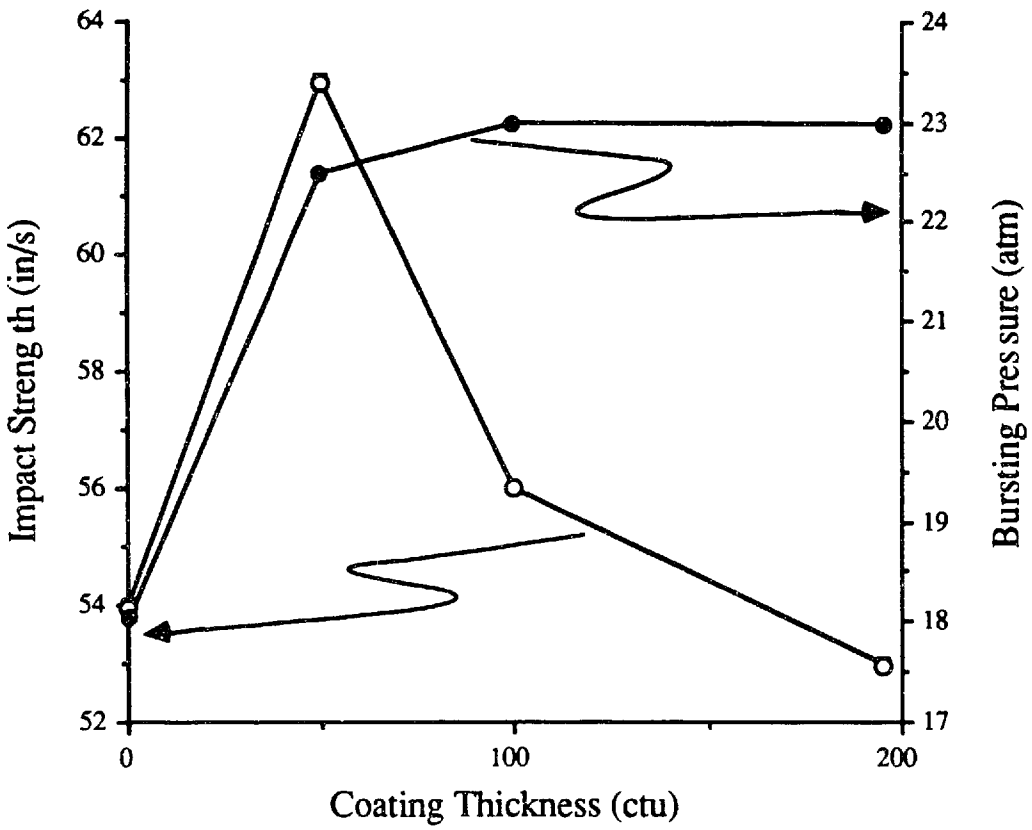

Figure 2.1: Bursting pressure and impact strength for SnO_2 coated soda-lime-silicate containers. (Data from reference 43. One "ctu" equals about 2 Å [25])

2.3 Abrasion Resistant Coatings

A great deal of information on the mechanical effects of thin oxide coatings is available from studies of tin oxide and titanium oxide, used as hot end coatings, on soda-lime-silicate glass containers. However, the effects of these coatings on the strength of glass is not agreed upon. Southwick,[44] for example, reported that glass containers coated with about 500 Å of tin oxide were roughly 50% stronger under impact than uncoated containers. Williams[43] and Evans and Davidge[46] both coated fresh, hot containers on-line, and found a 20% to 35% increase in strength, depending on the method of strength testing - bursting, bi-axial, or impact. When the coating thickness was decreased to 20 - 40 Å, on the other hand, Howes[47] saw no effect of the tin oxide coating. In an effort to isolate thoroughly the effects of the tin oxide coating alone, Davis[45] indented ordinary microscope slides with a Vickers indenter, coated them with 140 Å of tin oxide, and then compared the four-point bend strength and susceptibility to static fatigue of coated and uncoated slides. He found no difference between the coated and uncoated samples. Finally, for HF etched and coated glass plates, Ohta et al[48] observed a 30% decrease in the bi-axial strength; and Swindlehurst and Cantor[49] made similar observations for containers sputter coated with tin oxide. These studies are summarized in Table 2.1.

The overall lack of agreement as to the effects of these coatings on the strength of glass containers makes generalization difficult. Nevertheless, there must exist some common ground upon which these data can be compared and reconciled. Indeed, one can conclude that these thin oxide coatings increase the abrasion resistance of glass; and if we assume that resistance to minor abrasions constitutes the primary effect of the coatings, then the apparent contradictions can be explained as follows:

Table 2.1: Effect of Thin Oxide Coatings on Strength, Abrasion Resistance, and Coefficient of Friction of Soda-Lime-Silicate Glass.

Reference	Material	Thickness	Strength Change†	Effect on Abrasion Resistance	Effect on μ
Southwick	SnO_2	~500Å	NA_p§ - up	up	down
Southwick	SnO_2	~500Å	NA_b§ - up	up	down
Williams	SnO_2	~200 Å	0.6_p-up	up	down
Williams	SnO_2	~200 Å	NA_i -up	up	down
Evans	SnO_2	~10,000 Å	17_b- up	NA	NA
Howes	SnO_2	20 - 40 Å	NA -none	NA	NA
Davis	SnO_2	140 Å	9_b - none	NA	NA
Ohta et al	SnO_2	~1000 Å	150_b- down	NA	NA
Swindlehurst	SnO_2	30 - 3000 Å	50_b- down	down	up
Dettre	TiO_2	50 - 300 Å	NA	up	down
Gray	TiO_2	50 - 1000 Å	NA	up	down
Carl	TiO_2	150 - 350 Å	NA	up	NA
Ward	SnO_2	50 - 100 Å	0.3_p - NA	up	NA
Dunton	TiO_2	NA	NA	up	NA
Sanyal	SnO_2	NA	NA	none	none

† Strength given in ksi. Subscripts refer to testing method: b-bend test ; p-bursting pressure; i-impact strength. Note that impact strengts can not be represented in ksi.
§ Information Not Available from Reference.

Strength increases were reported in the studies by Williams and Evans[43] and Davidge[46] for coatings which were applied on-line to fresh containers. The containers would have been rather strong at the time of coating, so that the strength losses which usually occur during cooling and handling could have been reduced by the abrasion resistant tin oxide coating. Howe's coatings,[47] which were also applied on-line, provided no increase in strength. His coatings were probably too thin (20-40 Å), however, to provide any noticeable abrasion resistance. In fact, Ward[50] has shown that SnO_2 coatings of less than 3 $\mu g/cm^2$ (~50 Å) are ineffective in providing containers with any protection against abrasion, while coatings thicker than about 100Å are necessary to provide significant protection. In Davis' experiments,[45] the coatings were applied to already flawed (indented) samples, so that increases in abrasion resistance did not effect the strength. Ohta,[48] who noticed a decrease in strength with coating, applied his coatings to pristine glass plates inside a tube furnace and then handled them very carefully until breaking. Since his samples were not subjected to the abrasive rigors of cooling in the dirty atmosphere and extensive handling as were those of Williams and Evans and Davidge, abrasive damage was insignificant. Other effects, such as micro-crystalline regions, grain boundaries within larger crystalline regions, or pin-holes in the coatings were probably influential in Ohta's work. Such defects usually go unnoticed, because the flaws inherent in the glass substrate are more severe. For Ohta's etched and carefully handled samples (strengths of 150 ksi in bending), the intrinsic flaws were likely much smaller than the sizes of the coating flaws. Lastly, Swindlehurst and Cantor[49] likewise observed decreases in strength after coating. They also reported a decrease in abrasion resistance, however, which would be expected to degrade container strength for the same reason that increased abrasion resistance enhances container strength.

The degraded abrasion resistance observed in Swindlehurst and Cantor's samples is unique. (See Table 2.2) In most cases, enhanced abrasion resistance correlates with a decrease in the coefficient of friction. As mentioned above, the tensile stress imparted on a surface by horizontally translating abrader is proportional to μ. Indeed, in all of the studies summarized in Table 2.2, changes in abrasion resistance after coating correlate with changes in the coefficient of friction. This includes Swindlehurst and Cantor,[49] who were the only ones to observe an increased coefficient of friction. The cause of their increase in μ is unclear. It is worth pointing out, however, that the coefficient of friction is very sensitive to surface roughness. In fact, Ward[50] has shown that by simply hand polishing fresh SnO_2 coatings with a linen cloth, the coefficient of friction is decreased and the abrasion resistance is raised by over 40%. Moreover, Smay [51] has shown that small changes in processing parameters or atmosphere used to deposit hot end coatings can cause significant changes in the coating morphology. Peculiarities in Swindlehurst and Cantor's deposition techniques may, therefore, have resulted in unusually rough surfaces and increases in μ.

3.4 Flaw Healing

The healing of pre-existing flaws represents another potential way in which thin oxide coatings could increase the strength of glass. This method of strengthening would be advantageous insofar as the surface of a material could be returned toward a pristine state, regardless of preceding damage. The possibility was suggested by Sokolova,[42] "After it [the coating] has filled up the surface defects and become chemically bonded to the surface, a strong metal oxide film can lower the concentration of local stresses." This is only suggested as a secondary effect; and there is no further evidence or suggestion

presented of filling the surface flaws. In describing a polymeric cladding material for silica optical fibers, Beck and Hodge[52] make reference to the formation of "bridge bonds, which tend to heal small surface flaws," although the suggestion is not investigated. Surprisingly, detailed studies of flaw healing by the application of thin coatings are lacking in the published literature.

It would appear that sol-gel coatings might be useful in realizing all four glass strengthening methods discussed - the generation of compressive stresses, barriers to fatigue-causing moisture, the development of abrasion resistant surfaces, and flaw healing. The possibility of healing of flaws seems particularly intriguing, in light of its novelty, its potential for strengthen weak bodies, as opposed to simply reducing the decay of strength, and the possibility of combining it with other strengthening and strength preserving techniques. The remainder of this thesis will therefore focus on the use of sol-gel coatings for increasing the strength of already flawed bodies. The possibility of decreasing fatigue by providing protection from moisture will be considered along the way; and issues regarding the use of such films as abrasion resistant coatings will be discussed in Appendix C.

III. Preliminary Investigations

To probe the possibility of strengthening glass by sol-gel coatings, a set of preliminary experiments was conducted. In these experiments, TEOS derived coatings were applied to abraded silica rods. Upon firing, the alkoxide coatings were converted into dense silica films at temperatures less than that needed to anneal the rods. The silica-on-silica system was chosen so that compositional inhomogeneities and stresses caused by CTE mismatch between the substrate and coating were minimized. The details, results, and implications of these experiments will be discussed in this chapter.

3.1 Experimental Procedures

Coating solutions were prepared by partially hydrolyzing TEOS with 2 moles H_2O per mole TEOS in 1 mole ethanol. Unless otherwise stated, HCl was added to bring the solution pH to 2, after which the solutions were allowed to react for from one to three hours before coating. An effort was made to keep the solutions at room temperature by immersing the reaction flask in a water bath. This method resulted in limited success, however, as the exothermic nature of the hydrolysis reaction tended to raise the temperature of the solution to about 50 °C for a short time, even with the water bath. These low H_2O, low pH solutions have been suggested by Sakka and Kamiya[53] to produce linear, polymeric-type oligomers, which are more coatable than the particulate-like species produced by high H_2O or high pH solutions. As one would expect when understoichiometric amounts of water are used for hydrolysis, the solutions were also

very stable; when stored under nitrogen, gelation was never observed, even after six months.

Silica rods, 6mm in diameter, were used as the substrate material. Using rods avoided edge fracture problems which occurred when flat plates were tried. Because of the large scatter in the strength of as-received rods, and the concomitantly large number of samples needed to obtain meaningful data, the rods were abraded by ball milling with 5 gr. Al_2O_3 pellets at 150 rpm for two minutes prior to coating . As shown in Figure 3.1, such abrasion drastically decreased the scatter in strength values and provided a consistent baseline for the coating study. After abrading, the rods were degreased in methylene chloride, rinsed in acetone, and then wiped clean with ethanol.

About two-thirds of the abraded, cleaned rods were next placed in a beaker of the TEOS solution inside a chamber filled with dry argon. By withdrawing the solution at a rate of 3 cm/min, clear, even coatings, about 3000 Å thick, were produced. A few samples were coated by withdrawing the rods rapidly (about 300 cm per sec) from the coating solution. This produced coatings which were almost one micron thick. All coatings were allowed to dry in the argon atmosphere for at least ten minutes before being exposed to atmospheric humidity. (The uncoated rods were used as control rods, which were run side-by-side with the coated rods through all treatment steps except coating, so as to separate annealing from coating effects.)

After coating, all samples, coated and uncoated, were placed on a stainless steel rack which was put inside a silica tube furnace. Unless otherwise stated, all samples were fired in air at a constant rate of 5 °C/min to the temperature of interest (from 20 to 1050 °C) and then slowly cooled at about 2 °C/min by turning off the power to the furnace. To test for the presence of residual thermal stresses, some samples were

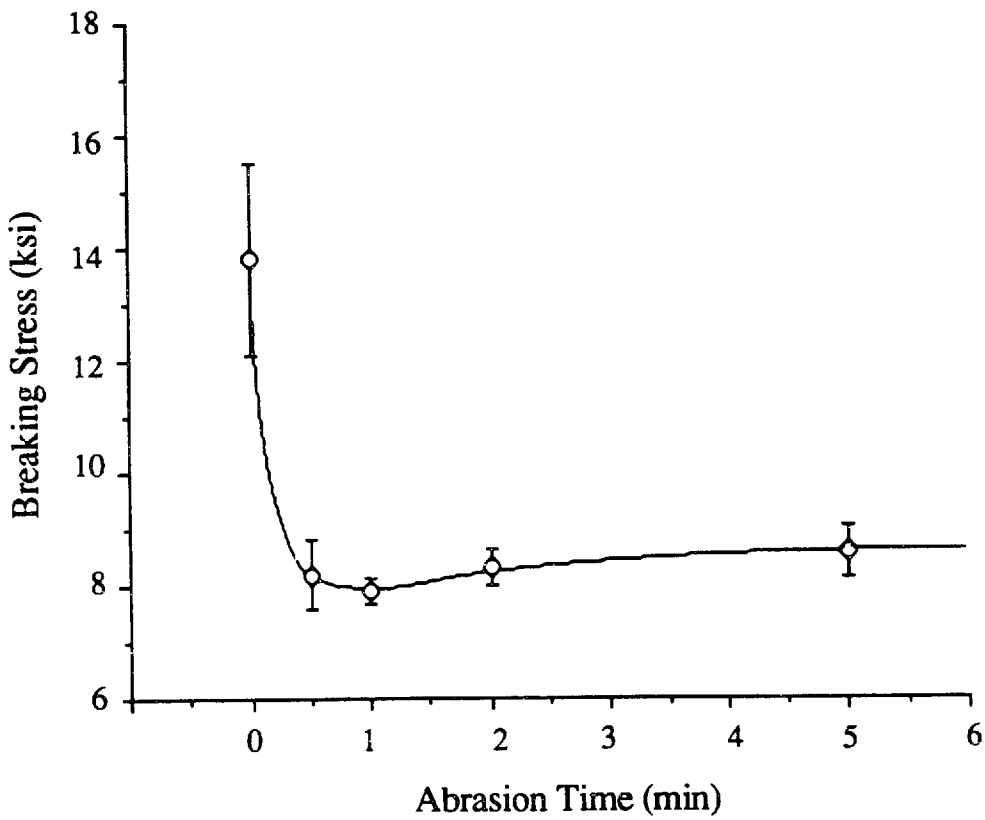

Figure 3.1: Change in rod strength with abrasion time. Notice the drastic decrease in scatter, as well as strength, with increased abrasion time.

quenched by pulling the rack directly out of the hot furnace, resulting in a cooling rate of about 500 °C/min.

The samples were broken in four point bending in air with a crosshead speed of 0.2"/min (~7500 psi/sec). (A detailed description of the four point test fixture is given in Appendix B.) To aid in recovering the fracture pieces, adhesive tape was placed on the compression side of each rod just prior to breaking. (To examine the effects of fatigue, one set of samples was broken while immersed in a bath of liquid nitrogen instead of in air.)

Changes in coating thickness during firing were measured using flat silica and silicon slides as substrate materials. The slides were coated in the same manner as were rods. Profilometry* was used on the coated silica slides which, before firing, had been partially scraped clear of the coating to provide a well-defined step for measurement. These measurements provided a convenient method of monitoring the loss of porosity, i.e. densification, of the coatings as they were fired. Ellipsometric§ measurements on the coated silicon substrates were also used to follow changes in coating thickness. Ellipsometry also allowed changes in the index of refraction to be monitored, providing a better evaluation of the absolute density of the coating.

---

* Sloan DEKTAKII model profilometer

§ Gaertner Scientific Corp. model L117 ellipsometer, operated at a 70 ° angle of incidence

3.2 Results

The increase in strength of coated rods is shown in Figure 3.2 as a function of firing temperature. Increases in strength of more than 120% (from 9 to 20 ksi) were seen when the samples were heated to 900 °C. At higher temperatures, annealing effects in the uncoated glass became significant, obscuring the effects of the coating.

Coating shrinkage vs. firing temperature is also plotted in Figure 3.2. It is apparent that strengthening is closely tied to densification, since larger strengths are obtained as the coatings continue to shrink. Coating thicknesses continue to decrease as the temperature rises above 900 °C, however, indicating that densification is not complete at 900 °C, where annealing effects become significant. As a result, an attempt was made to densify the coatings before the rods annealed. This was carried out by plunging coated rods into a hot (1000 °C) furnace and removing the samples after various intervals of time. The results are shown in Figure 3.3. The fact that the coating thickness (and index of refraction, which is not shown in Figure 3.3§) are constant after about five

§ It was hoped that the ellipsometric measurements of the index of refraction (n) would allow an absolute determination of the coating density to be made. Unfortunately, residual carbon, which was on the order of a few atomic %, raised n, which offset the lowering of n caused by porosity. The effect of this carbon was significant; the index of refraction of the fired coatings 1.8, was significantly higher than that of fused silica, 1.45. It is unknown why Pantano et al[89] did not observe such a dramatic increase in n in their TEOS-derived silica coatings.

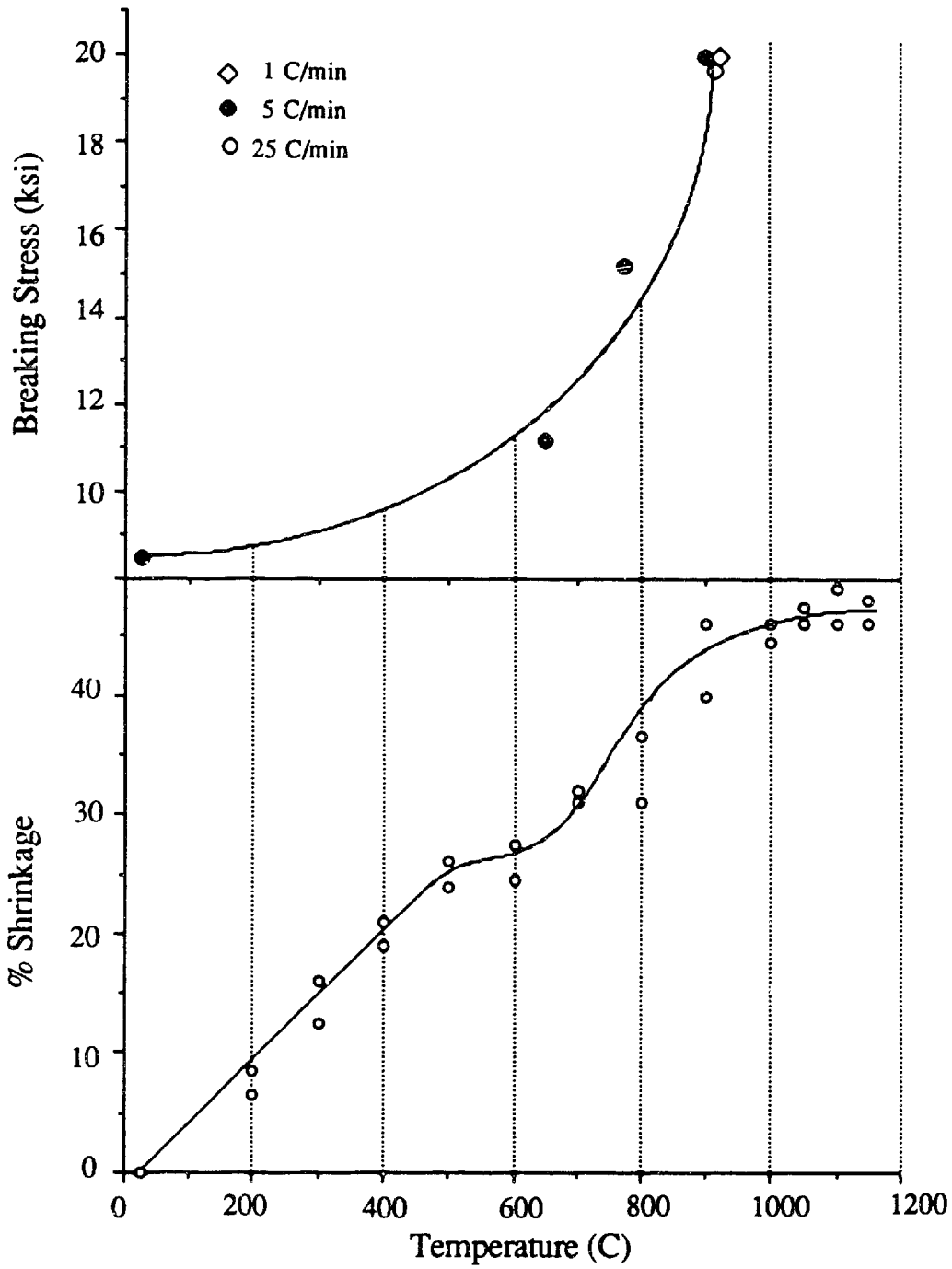

Figure 3.2: Strengthening of coated rods (top) and shrinkage of coatings (bottom) as a function of temperature.

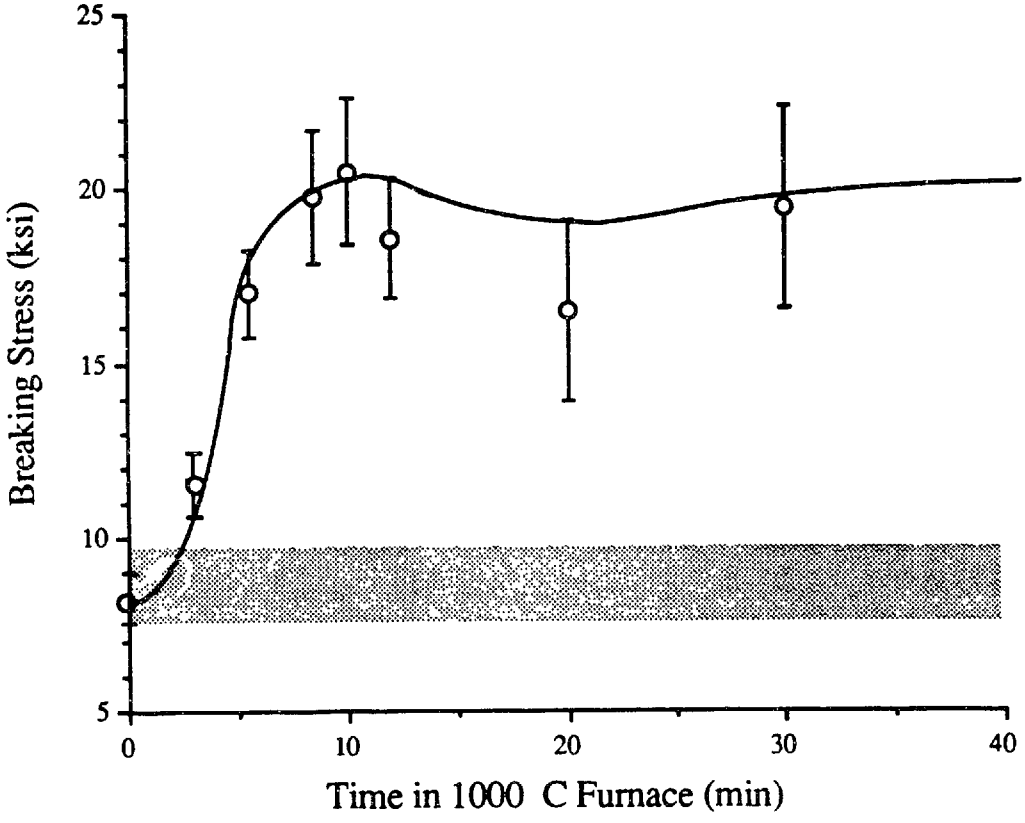

Figure 3.3: Strengthening of silica rods as a function of time in hot furnace. Shaded region represents strength of uncoated, fired control rods, and the full error bars represent one standard deviation.

minutes indicates that the densification process in the coatings effectively stops before any annealing effects on the surface flaws are observed.*

Heating coated samples to 900 °C at 25 °C/min and 1 °C/min was found to produce about the same increases in strength as heating at 5 °C/min and as plunging the samples into a hot furnace. More interesting is the lack of dependence of strengthening on the cooling rate; samples heated to 900 °C and pulled directly out of the hot furnace (~500 °C/min) showed the same strengthening as samples which were allowed to cool slowly, ~2 °C/min, from 900 °C.

After firing, most coatings appeared featureless under a light microscope (Figure 3.4a), although the thicker coatings produced by rapid sample withdrawal appeared specular as a result of cracking (Figure 3.4b). Despite this difference in morphology ofthe coatings, there was no discernable difference in the strengthening effect of cracked vs. uncracked coatings.

Finally, samples broken under liquid nitrogen were strengthened by about 130 %, from 12.5 ksi to 29 ksi after firing at 1000 °C.

* For these 6mm rods, densification probably takes place in a bit more than five minutes, since heat transfer is expected to be slower in the thick rods than in the thin, 1mm slides on which the changes in coating thickness were measured. However, annealing effects on the sample flaws, as reflected in the strength of uncoated rods, were not noticed, even for long times, in the constant temperature experiments. The thermal mass differences are therefore expected to be insignificant.

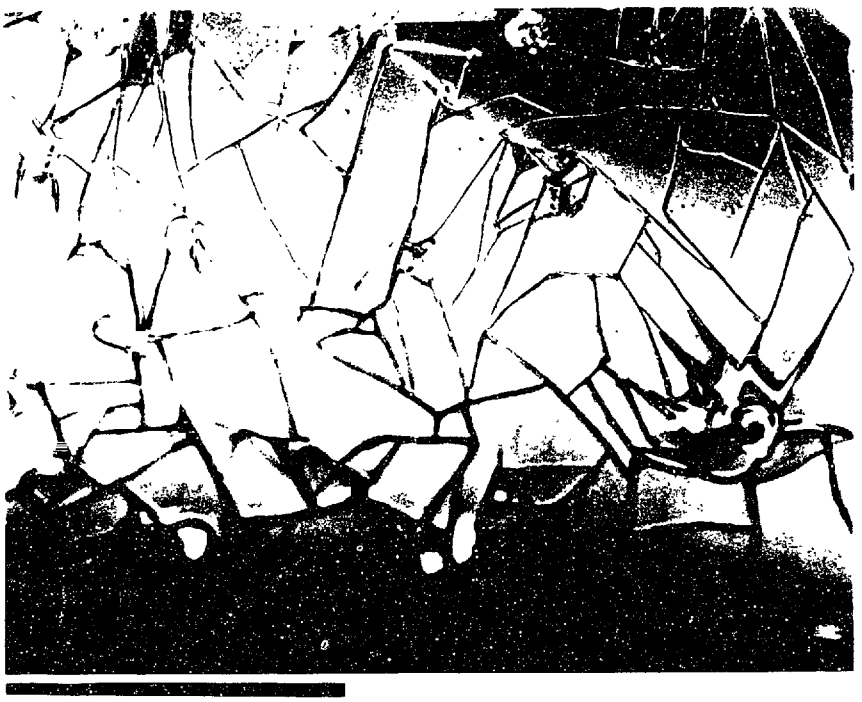

a.

b.

Figure 3.4: (a) specular coating and (b) clear coating, both of which exhibited similar increases in strength. Bar indicates 200 μm.

3.3 Discussion

The ability to increase the strength of a glass substrate by the application of an alkoxide derived coating has been demonstrated. The strengthening seems limited, however, to about 120%, or 20 ksi. To understand whether or not this is an intrinsic limit of the process, insight into the strengthening mechanism is necessary. In the remainder of this chapter we will try to determine whether the strengthening is a result of protection against stress corrosion, of compressive stresses, or of direct interaction between the solution and microflaws.

When rods were broken under liquid nitrogen, coatings resulted in about a 130 % strength increase, from 12.5 to 29 ksi. Since a substantial increase in strength is still obtained when rods are broken in liquid nitrogen (i.e., when fatigue is eliminated) it appears that the observed strengthening is not the result of the formation of a moisture barrier which protects against stress corrosion. Moreover, the strengthening observed with coatings which cracked during processing (Figure 3.4a) was the same as that for uncracked coatings (Figure 3.4b). If stress corrosion protection were involved at all in the observed strengthening, then we would expect the uncracked sample to be stronger.

The fact that different cooling rates do not change the degree of strengthening indicates that surface compressive stresses caused by rapid quenching are not responsible for the observed strengthening. In fact, the absence of **any** appreciable bulk stress - whether caused by quenching or film shrinkage during firing - was demonstrated by examining the fracture surfaces as follows.

When one views the fracture surface of a glass sample, three distinct regions are usually visible. As shown in Figure 3.5, the smooth inner region, known as the mirror,

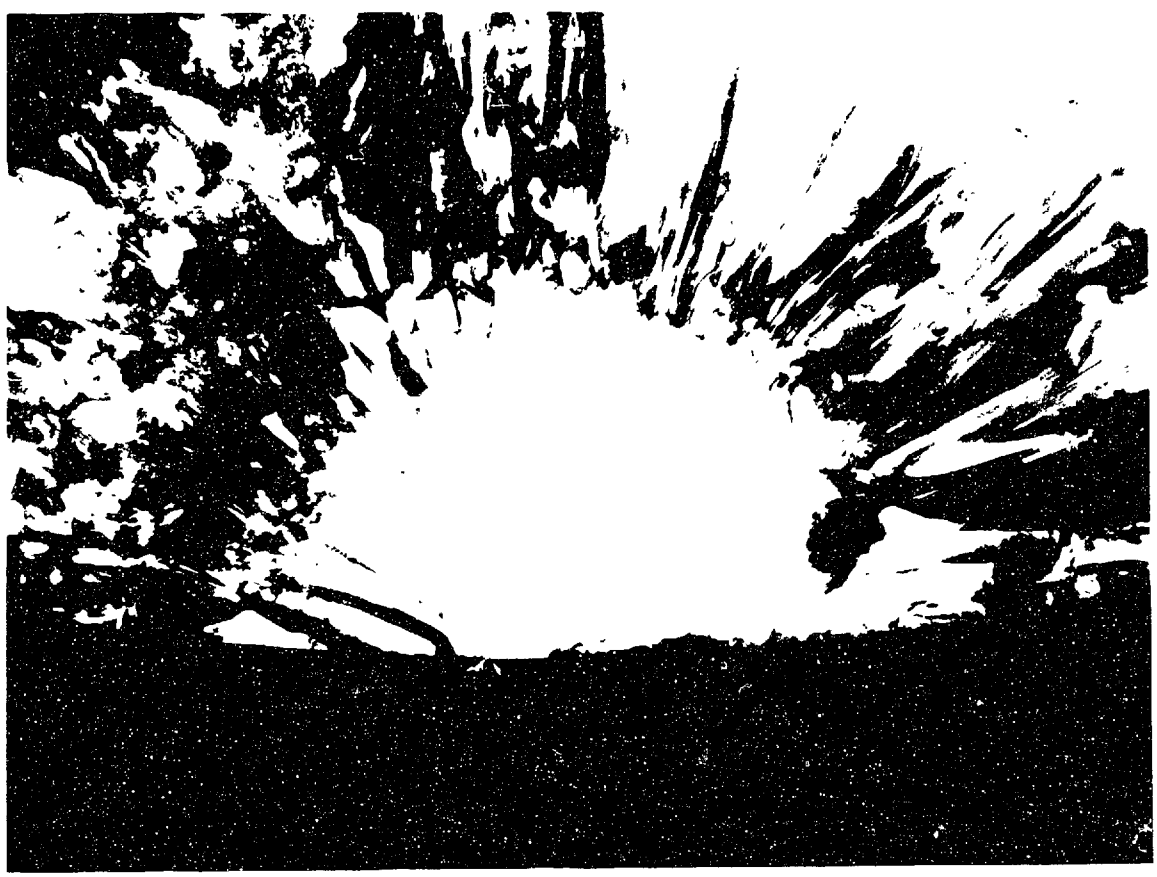

Figure 3.5 Fracture surface of a 6mm glass rod broken at 18 ksi. (Total width of micrograph is 1.5 mm)

is surrounded by a thin, rougher looking area, known as mist, which is in turn surrounded by a very rough, hackle region. The formation of these regions can be explained using the basic principles of fracture mechanics which were presented in Section I. In terms of stress intensity factors, we recall that fracture occurs when K_I exceeds the critical stress intensity factor, K_{Ic}, which is determined by the energy necessary to create the two new surfaces (Equation 1.12). As a flaw begins to propagate through the sample, the stress intensity continually increases (Equation 1.11) as the flaw size increases; and if the sample is broken under relatively high stress, K_I may, at some point, exceed the energy necessary to create **four** new surfaces. At this point, the single crack can branch into two cracks, and since two flaws can't coexist on the same plane, one or both of the cracks must momentarily leaves the original fracture plane. These small wanderings from the main crack plane leave a characteristic ripple mark, known as mist, on the otherwise smooth fracture surface. As the flaw continues to propagate, K_I continues to grow until more surfaces can be generated. The deviations from the main crack plane become more severe and markings known as hackle, which can be regarded simply as severe mist, result.

The stress intensity at which mist occurs, K_m, is a function of the surface energy of the material and is, therefore, a material constant. Since the entire fracture process happens quite rapidly, the externally applied stress is virtually constant, so that the product of the applied (failure) stress and the square root of the length of the flaw when misting occurs, c, should be a constant,

$$M = \sigma_{app}\sqrt{c} \qquad 3.1$$

where M, known as the mirror constant, is, in theory, equal to $K_m/\sqrt{\Omega}$ (see Equation 1.11). Hence a plot of the applied fracture stress, σ_{app}, versus $c^{-1/2}$ should give a straight

line with slope equal to the mirror constant and y-intercept equal to any residual stress present in the glass at the time of rupture. That is, when $c^{-1/2} = 0$, the flaw length is infinite: the sample is completely fractured; and the strength be equal to zero. If, however, there is any residual stress in the glass at this point, the sample will have "residual positive strength" if the stress is compressive and "negative strength" if the stress is tensile.

A plot of σ_{app} versus $c^{-1/2}$ for coated and uncoated glass appears in Figure 3.6. The plot has been corrected for the bending-induced stress gradient into the bulk of the rods by assuming that the applied stress at the advancing flaw tip is $\sigma(r-c)/r$, where σ is the applied stress at the tensile surface and r is the rod diameter.[54] The magnitude of this correction is not insignificant. It ranges from about 5% for the smallest mirrors (strongest samples) to just over 25% for the largest mirrors (weakest samples). Since data for both coated and uncoated samples fall on the same straight line, we conclude that the coated and uncoated samples are under the same state of bulk stress. Furthermore, since this line extrapolates to the origin, the value of this stress is zero. If a compressive stress were present in the coated rods, the data for the coated samples would lie on a line shifted up (remaining parallel, since the slope is a material constant) by an amount equal to the strengthening, roughly 8 ksi for this set of experiments. This line, which is well removed from the data points, is also drawn in Figure 3.6. (The slope, 1.9+/-0.2 ksi$\sqrt{"}$, agrees well with the literature value[55] of 2.0 ksi$\sqrt{"}$ for uncoated fused silica. The slope also agrees well with the value 1.82 ksi$\sqrt{"}$, derived from the simple fracture mechanics arguments discussed above. Such agreement simply indicates that, as one would expect,the coatings do not drastically alter the ultimate strength, reflected in K_c, of the underlying bulk glass.)

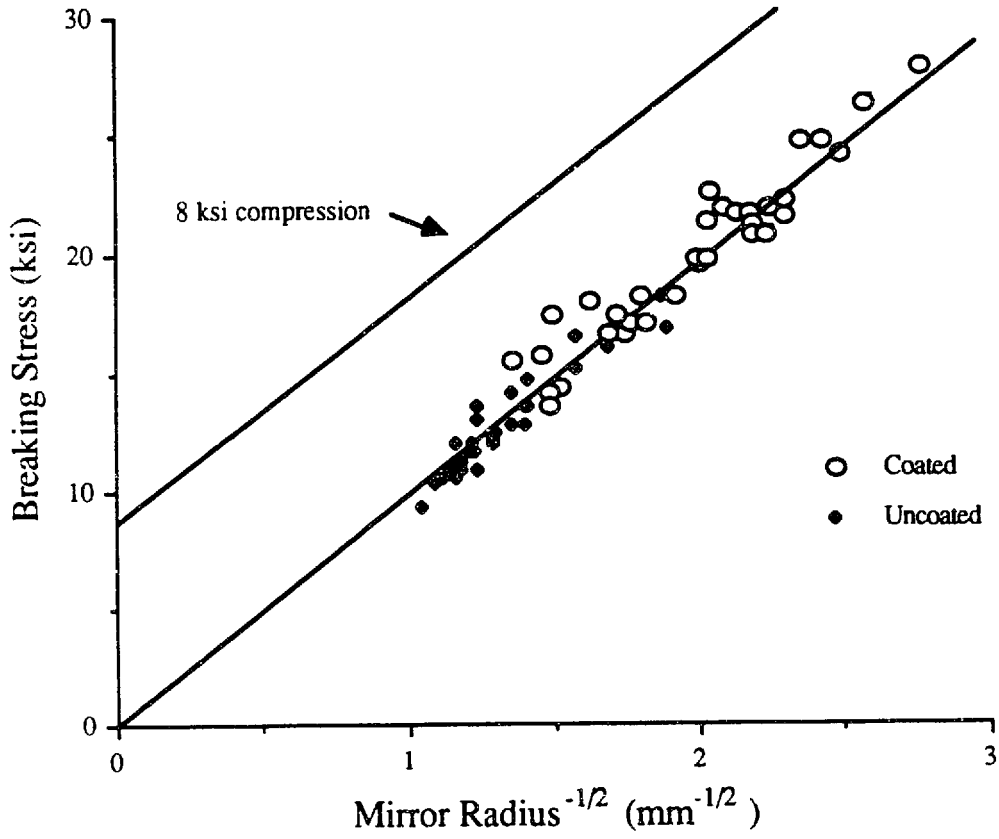

Figure 3.6: Fracture stress versus (mirror radius)$^{-1/2}$ for coated and uncoated rods. Upper line is hypothetical shift for a sample under ~8 ksi compression.

Further evidence for the insignificance of surface compressive stresses is provided by the similar strengths observed in cracked and uncracked samples (Figure 3.4). Despite the extreme difference in morphology, i.e. cracked and uncracked coatings, both samples showed the same strengthening (~100%). This similarity indicates that surface compression is insignificant in the strengthening, since the compressive stresses would be relieved by cracking. Moreover, any mechanism which involves bridging over the top of the flaw, as depicted in Figure 3.7 a, must be inappropriate, since the large number of flaws in the abraded rods ensures that many potentially fatal flaws would lie underneath a crack for cracked coatings. Such flaws would be unaffected by the coating, and rods with cracked coatings would not be strengthened. It appears, therefore, that the strengthening mechanism must involve some sort of penetration into the flaws, such as that drawn in Figures 3.7 b-d.

Establishing that flaw penetration is involved in the strengthening mechanism is quite interesting, insofar as we have now obtained evidence for a novel strengthening process, flaw healing by alkoxide derived coatings. Our understanding of the mechanism based on the data presented above stops there, however; and the limit on strengthening of about 20 ksi is still unknown. Is the chemistry of the TEOS solution limiting the strengthening? Or are the flaws produced by the alumina abrasions only slightly penetrable? Or is the strengthening the result of a unique solution/abrasion combination? In the next chapter, the effects of changes in chemical parameters of the TEOS solution will be investigated. In the final chapter, steric, or penetration, issues will be explored, all with the ultimate goal of gaining further insight into the strengthening mechanism and its limits.

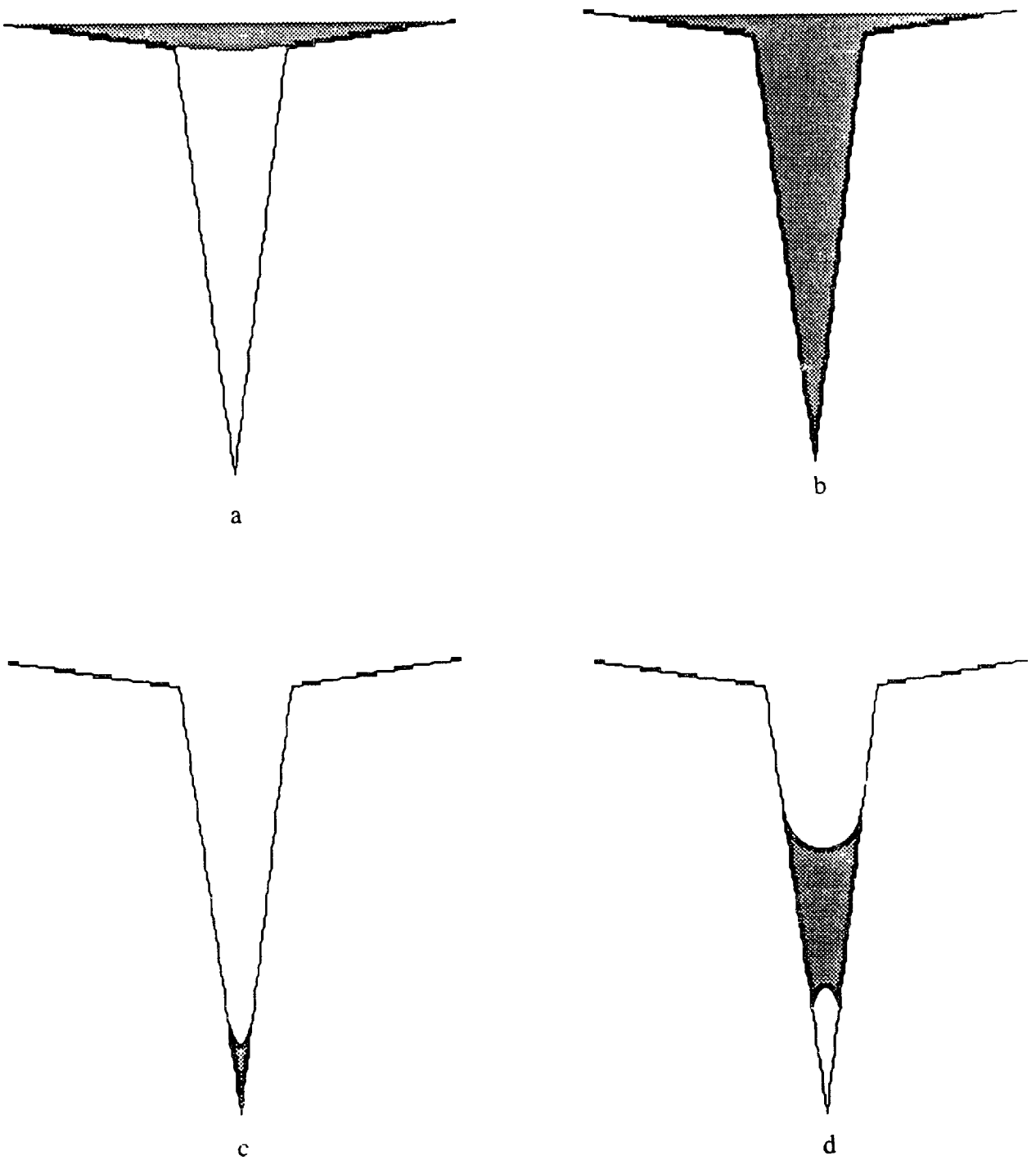

Figure 3.7: Schematic representations of hypothetical coating/substrate interaction morphologies: (a) surface bridging; (b) flaw filling; (c) tip blunting; and (d) flaw bridging.

IV. Chemical Effects

In Chapter I, it was pointed out that the mechanisms, rates, and extents of the hydrolysis and condensation reactions (1.1 to 1.3) are strongly affected by changes in water concentration, catalyst, temperature, and dilution. If chemical interaction between the solution and glass substrate limits the strengthening attainable with alkoxide-derived coatings, it is likely that these chemical effects will, in turn, affect strengthening by sol-gel coatings. In this chapter, we will attempt to define the important chemical parameters involved in the sol-gel strengthening process.

4.1 Degree of Hydrolysis

In the preliminary experiments, TEOS was partially hydrolyzed before coating. Partial hydrolysis was used so that silanol groups, which are presumed to be necessary for condensation between the coating and substrate, would be present in the coating solution. Since increasing the amount of water available for hydrolysis raises the silanol concentration (Equation 1.1), higher water concentrations might be expected to enhance strengthening. Increasing the amount of water in solution changes more than just the silanol content, however, so that it is possible that there exists an optimal concentration of water for maximizing strengthening. This possibility was explored in the following experiments.

TEOS solutions were prepared in the manner described in the vacuumhyd section, except that the amount of water added for hydrolysis was varied from 0 mole H_2O per

mole TEOS to 5 moles H_2O per mole TEOS. Silica rods were then coated, fired, and broken in four point bending, along with control rods, as before. The results are presented in Figure 4.1 as a plot of strength versus degree of hydrolysis, n, which is defined as mole H_2O per mole TEOS. It is apparent that the degree of hydrolysis has a strong effect on the strengthening, especially where $n \leq 2$. For $n \geq 2$, this dependence flattens out, as there appears to be a critical concentration of water, $n \approx 2$, above which the degree of hydrolysis is unimportant.

As expected, hydrolysis is necessary to achieve any strengthening, and increasing the silanol content (up to $n \approx 2$) enhances the strengthening. At $n = 2$, each silicon atom has, on average, two hydroxyl groups attached (see Section 1.2). It is not unreasonable that two silanol ligands per silicon atom are adequate for condensation onto the hydrated substrate. The extra silanol groups produced above n=2 might then be redundant, so that the strengthening saturates at n=2. Other effects, such as changes in the molecular size, may, however, also be important.

Keefer,[15] for example, used small angle x-ray scattering (SAXS) to study changes in the size§ of the siloxane oligomers formed in TEOS solutions under various conditions of hydrolysis. Changes in the electronic radius of gyration for TEOS solutions hydrolyzed for 48 hours* at a variety of pH's with different amounts of water

§ One must be cautious in interpreting the electronic radius of gyration as a definite molecular size, especially for the polymeric species formed in low pH / low water solutions. These species, as Brinker[56] points out, may become overlapped and entangled, especially near the gel point and at high concentrations, resulting in erroneously small measured radii of gyration. This apparent complications turns out to be fortuitous, however, since it is actually this overall size of the tangled polymer which is important in penetration into a flaw.

* A constant hydrolysis time of about 2 hours was used in our experiments. However, since hydrolysis takes about 20 minutes to go to completion[18] and condensation is virtually non-existent at pH=2, we expect very little difference in molecular size between TEOS hydrolyzed for 2 hours and 48 hours.

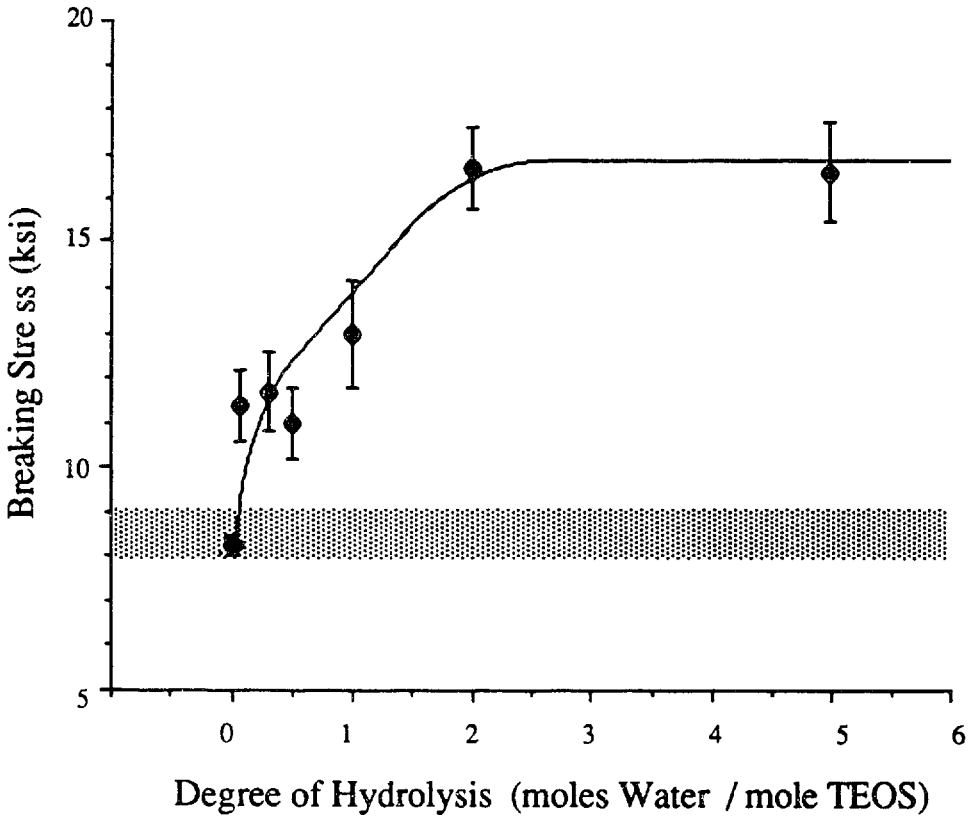

Figure 4.1: Change in strength as a function of degree of hydrolysis. Shaded region represents strength of uncoated, fired control rods, and the full error bars represent one standard deviation.

are summarized in Table 4.1. We see that at the pH used in this study (pH=2), increasing the water content above n=2 increases the molecular size. Since increases in molecular size are expected to hinder penetration of the solution into flaws, the constant level of strengthening observed for $n \geq 2$ indicate that the molecular size does not, by itself, control the strengthening in the high n range. Below n=2, we have no data on molecular size, although there is no reason to suspect that the increasing trend in oligomer size with increasing water content should be different in the n=0 to n=2 range. If this trend is still valid then at low n, where the strength increases steadily with water content, then oligomer size is certainly unimportant, and solution silanol content may be limiting the strengthening.

To examine further the importance of silanol groups for effective coating/substrate interaction, experiments were run in which the silanol content of the substrate was changed, while that of the solution was kept constant. In these experiments, coating solutions were prepared, as above, at pH=2 and n=2. The solutions were then coated onto rods prepared in the usual manner in either the laboratory atmosphere, or in a stream of steam, or onto exceptionally dry rods in a dry Ar atmosphere. The dry rods were prepared by either vacuum baking at 300 °C for one hour or by heating in chlorine gas at 250 °C for three hours. Such treatments have been shown to remove all of the physically adsorbed water and a substantial fraction of the chemically bound surface silanol groups.[57] The rods were then coated, fired, and broken in the usual manner, The results appear in Table 4.2.

Again, the importance of silanol groups for favorable substrate/solution interaction is indicated. Iler[58] points out that water molecules are readily adsorbed onto hydroxylated silica, but not onto bare siloxane surfaces. In fact, dehydroxylated silica

Table 4.1: Radius of gyration (Å) of TEOS solutions containing different water and catalyst concentrations after 48 hr. (From 15).

H_2O:TEOS	pH=2	pH=3	pH=4	pH=5
4	5.9	6.7	41.0	0
3	4.8	4.2	0	-
2	3.4	2.3	0	-

Table 4.2: Effect of changes in surface hydration on strengthening.

Treatment	Firing Temperature (°C)	Breaking stress (ksi)
standard prep / air coated	800	15
standard prep / steam coated	800	16
vacuum bake / dry coated	800	10
hot chlorine / dry coated	800	9

can be so hydrophobic that "A surface dehydrated to 0.66 OH nm^{-2} at 900 °C for 10 hr required several years in water at ordinary temperature to become rehydrated." [59] If one assumes that the condensation reaction of a solution silanol with a silica surface is analogous to the rehydration reaction, then the need for surface silanol is not surprising.

In conclusion, the importance of silanol species in both the solution and the substrate has been demonstrated. Moreover, the sensitivity of the strengthening to changes in surface hydration emphasizes the importance of the coating / substrate interface and hence surface preparation in the sol-gel strengthening process. Although a detailed investigation into different surface preparation techniques will not be included in this thesis, the potential significance of the substrate surface condition must be acknowledged.

4.2 Solution pH

Hydrolysis and condensation reactions have been shown to be very sensitive to the overall pH of the reacting TEOS solution. The effects include not only changes in molecular size and morphology, but also changes in the temperature at which densification takes place and in the amount of free silanol in solution. Having already established the importance of densification (Section 3.2) and solution silanol (Section 4.1), it is not unexpected that changes in solution pH would also affect the strengthening. To examine this possibility, coating solutions were prepared in the usual manner, except that a variety of HCl concentrations was used to produce solutions with pH's ranging from 1 to 7. These solutions were allowed to react for two hours and then coated onto

abraded silica rods, fired and broken in the usual manner. The results are shown in the top of Figure 4.2.

As expected, the solution pH has a strong effect on the strengthening. The most dramatic affect is the sudden loss of strengthening when the pH exceeds 4. This might be due to changes in oligomer size caused by pH changes; although the molecular size, as shown in Table 4.1, decreases with increasing pH for the reaction conditions, n=2, used in these experiments. Further, since smaller molecules are expected to help penetration, it appears that changes in oligomer size are not the primary cause of the drop in strength.

Both Brinker[60] and Nogami and Moriya[11] have shown that the temperature necessary to densify TEOS-derived silica increases with the solution pH. We recall from the preliminary experiments that densification of the coating is crucial for strengthening. It is, therefore, quite possible that the coatings hydrolyzed in the higher pH range ($pH \geq 4$) are not adequately dense after firing. Neither study examined more than two pH's; so a functional dependence of densification with pH is unknown. Another problem with this explanation is that there is no evidence of a decrease in densification temperature for the 1-3 pH range, where a definite increasing trend in the strengthening exists. Thus, if changes in the temperature required for densification are responsible for the strength decrease above pH=4, a separate explanation must be sought for the strength increases in the 1-3 pH range.

Changes in the silanol content of the coating solution represent a third possible explanation for the strengthening behavior seen in Figure 4.2. Aelion et al[18] showed that for a given time of reaction, the silanol content decreases as the solution pH increases within the pH=1.2 to pH=4.7 range. This behavior is due to a decrease in the rate of hydrolysis (which produces silanol) as the pH is raised within this acidic range, along

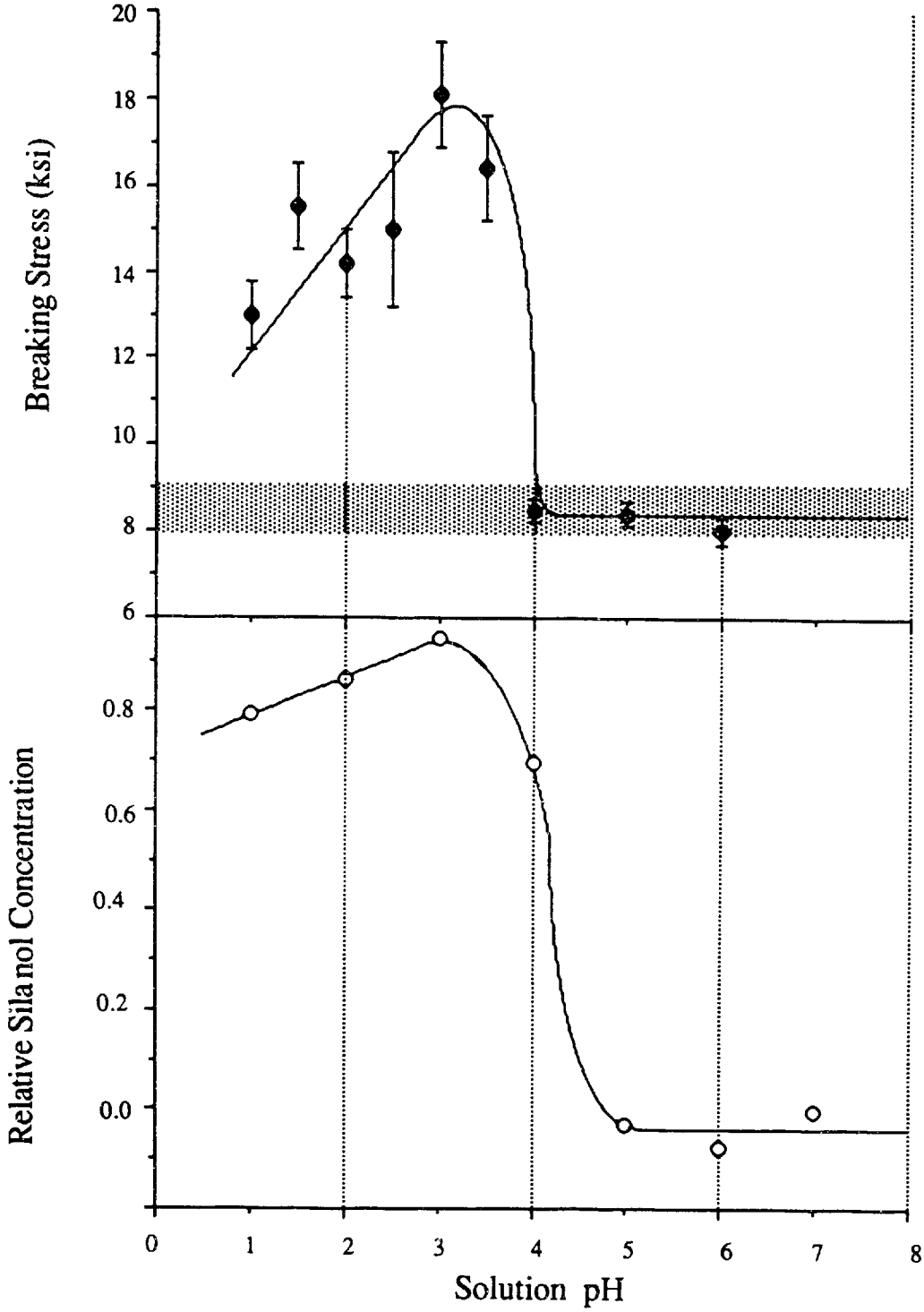

Figure 4.2: Effect of solution pH on strengthening (top) and relative silanol content in solution (bottom) for TEOS solutions with n=2. Shaded region is the uncoated, fired baseline, and the full error bars represent one standard deviation.

with an increase in the rate of condensation (which destroys silanol) as the pH increases above about 2.5. No more than three applicable points were examined by Aelion et al, however, so that a functional dependence of silanol on pH is unavailable. In addition, Aelion et al used a solvent, dioxane, which has a significantly lower dipole moment and higher viscosity than ethanol. Such differences can significantly effect solution chemistry.[32] Their solutions also contained a relatively large amount of water (n≈6). A quantitative comparisons with their experiments are therefore impossible.

As a result, a quantitative determination of the effect of solution pH on silanol content was made for our solutions using infrared spectroscopy. The ratio, R, of the free water peak at 1640 cm^{-1} to the C-C stretch at 1450 cm^{-1} was determined for each solution. The value of this ratio was arbitrarily set to 1 for a solution with pH=7, where it is known that the hydrolysis reaction is extremely slow. Since the organic content of each solution is the same, R is a measure of the water concentration, relative to that at pH=7, of each solution; and assuming that each hydrolysis event creates one silanol group, the silanol content scales with 1-R. This value, which we have called the relative silanol content, is plotted below the strengthening curve in Figure 4.2; and the agreement between the two curves is excellent.§

In summary, both the degree of hydrolysis and the solution pH have been studied; and both parameters have been shown to produce a marked effect on strengthening. In both cases, the effect can be well described by the necessity for silanol groups for effective substrate/solution condensation. The role of oligomer size appears to be

§ This analysis ignores the variable rate of condensation, which destroys two silanol groups and produces only one water molecule. However, the condensation rate rises roughly linearly with pH above pH≈2.5, so that the rise in silanol in the pH=1-3 range and the decrease in the 3-4 range would be sharpened by this effect, thereby improving the agreement between the two curves in Figure 4.2.

secondary, in both cases, to the effect of silanol content. While these experiments have been useful in defining important reaction parameters, and have provided some insight into the sol-gel strengthening process by indicating the importance of substrate/coating interface, the maximum strengths obtained are still only in the 20 ksi range. The limiting step, and key to further insight into the mechanism, must therefore lie elsewhere. In the next chapter, a fracture mechanics approach will be taken to analyze the steric, or penetration, issues to attempt to gain further insight into the process.

V. Mechanics of Coating Penetration

In the previous chapter, it was shown that although solution processing parameters of the coatings can affect the strengthening obtained, the solution chemistry does not, in itself, appear to limit the strengthening to 20 ksi. In this chapter, we will examine the physical interactions between the alkoxide coating solutions and surface flaws, focussing mainly on developing a quantitative description of the penetration of the solutions into flaws, with the objective of gaining a better understanding of the mechanism and limitations of the strengthening process.

5.1 Experimental Procedures

Vickers indented silica slides (1" x 1" x 1mm) were chosen as the substrate material for the experiments to be described in this chapter. Such hardness indents provide relatively ideal flaws for quantitative study of fracture because of their ability to provide a characterizable critical flaw before fracture, their reproducibility, and the wide range of flaw sizes which can be produced. In the experiments, each slide was indented once, in the center, with a load of 3 to 20 Kgr. The indented slides were then coated and fired in the usual manner. A ring-on-ring test fixture, which avoided edge effect problems, was used to fracture the samples in bi-axial stress with the indented side in tension. (As in the rod experiments, adhesive tape was placed on the compression side of each slide to aid in recovering the fracture pieces.) The test fixture and the pertinent stress equation are described in Appendix B.

5.1.1 Fractography of Vickers Indents

The microfracture patterns formed in soda-lime-silicate glass substrates by Vickers indents have been quantitatively described in a large collection of publications by Lawn and others[61-65, e.g.] Following the description of Lawn and Swain,[61] the formation of these patterns is drawn schematically in Figure 5.1 and described as follows.

During the initial loading (Figure 5.1a), an area of severe deformation is created directly below the indenter. The details of this deformation are, in general, poorly understood. It is often called the "plastic" region, although viscous flow and densification are probably the most active processes in the region[62]. For our purposes, the concept of a "plastic" zone which, after loading, exerts an effective outward force on the residual cracks will suffice[63]. Eventually, as the load is increased, a crack is initiated (Figure 5.1b) where the stress concentration is greatest. For the square pyramid indenter, this crack consists of two orthogonal vents perpendicular to the sample surface and in line with the edges of the indenter. The downward extensions of these cracks are known as the median vents; and the surface projections are called the radial vents. The complete median and radial systems produce two half-penny shaped flaws which grow (Figure 5.1c) as the indenter load, P, is increased. The stress intensity which drives this growth, K_e, is given by

$$K_e = \frac{\chi_e P}{c^{3/2}} \qquad 5.1,$$

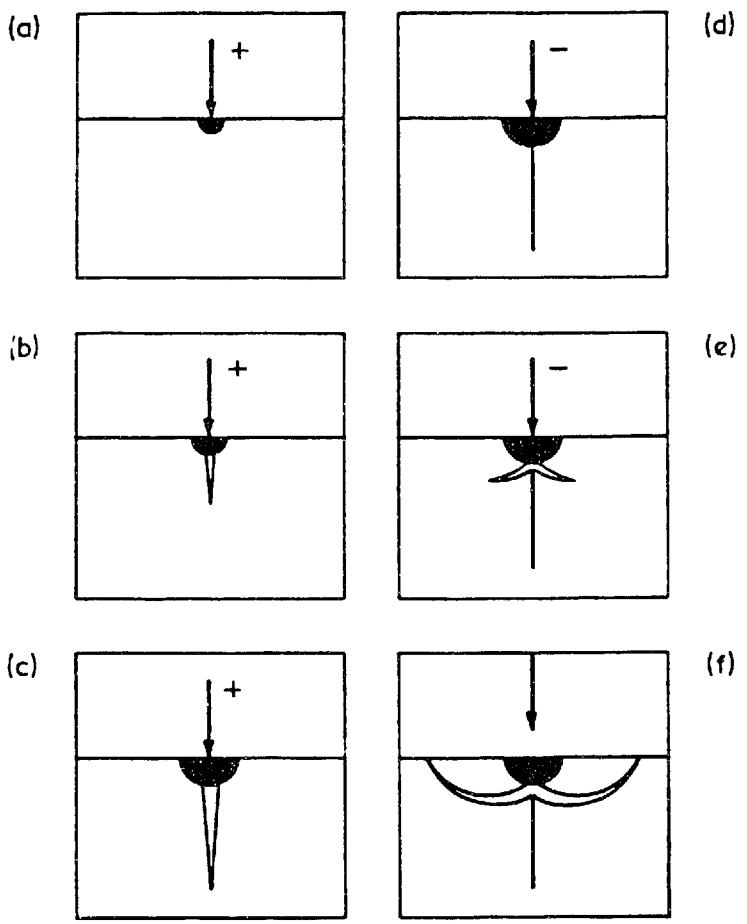

Figure 5.1: Schematic of vent formation during indentation loading (a-c) and unloading (d-e) half-cycles. (From ref. 61.)

where c is the crack half-length and χ_e is the elastic indenter/specimen constant. for silicate glasses indented with a Vickers diamond, χ_e is equal to about 0.03,[71] a value which is relatively insensitive to the indentation load.[63]

As the indenter is unloaded, the flaws begin to close, and even appear optically to heal (Figure 5.1 d). Mechanically, however, the re-closed surfaces have only a fraction of the strength of bulk glass, since they are held together by simple hydrogen bonding.[66] Finally, near the end of the unloading process, sideways extending lateral cracks (Figure 5.1e), roughly parallel to the surface, begin to appear. These vents are a result of the elastic mismatch between the bulk glass and the deformed material underneath the indenter. The mismatched material also acts as a wedge which holds the median/radial vents open, resulting in an effective residual stress intensity, K_r, across the medial/lateral system,

$$K_r = \frac{\chi_r P^*}{c^{3/2}} \qquad 5.2,$$

where χ_r[§] is the residual plastic indenter/material constant and P^* is the peak load. The final flaw structure, which is our main interest for the ensuing strengthening experiments, is thus composed of the lateral vents, perpendicular to which partially closed (but not healed) median/radial vents extend in a half-penny geometry (Figure 5.1 f).

Under a Vickers Indenter, silica glass behaves much the same as soda-lime-silicate glass. The most noticeable difference is that, for a given load, flaws are smaller in

§ For high hardness to modulus materials, such as silicate glasses, χ_r is about equal to χ_e.[63] A detailed description of the factors which effect the indenter/specimen constants, χ_e and χ_r, is given in reference 63.

silica glass than in soda-lime-silicate glass. This is simply a reflection of the fact that silica is a harder material. The only other significant difference is that the open structure in silica results in greater densification than in soda-lime-silicate.[67,68] This compaction has two effects. First, the indenter stress is distributed over a wider area, so that cone cracks, characteristically formed by blunt indenters, nucleate and propagate into the sample. The compaction also increases the elastic mismatch under the indenter, usually to the point that the lateral vents intersect the surface. When this happens, the deformed material is separated from the rest of the sample so that it chips away, taking with it the "wedge" that holds open the median/lateral vents thereby greatly reducing the residual tensile stress.

An SEM micrograph of an indented silica plate is shown in Figures 5.2. Median, radial, lateral, and cone cracks are visible in the micrographs. Although the cone cracks dominate the fracture pattern, it will be shown in the next section that, when broken under bending, the strength is controlled by the radial (surface) vents, and not the larger cone cracks.

5.1.2 Bi-Axial Fracture of Indented Silica

During loading, the stress intensity, K_I, at the tip of a crack of length a is given by Equation 1.11. For the Vickers indented silica plates, the question immediately arises as to which crack length should be used as the flaw length, c. It would appear, at first glance, that the cone crack is the most severe, and that its length should be the basis for calculating the stress intensity. When a finite plate is broken in bending, however, the tensile stress decreases as the neutral plane is approached. Hence, the tips of the cone

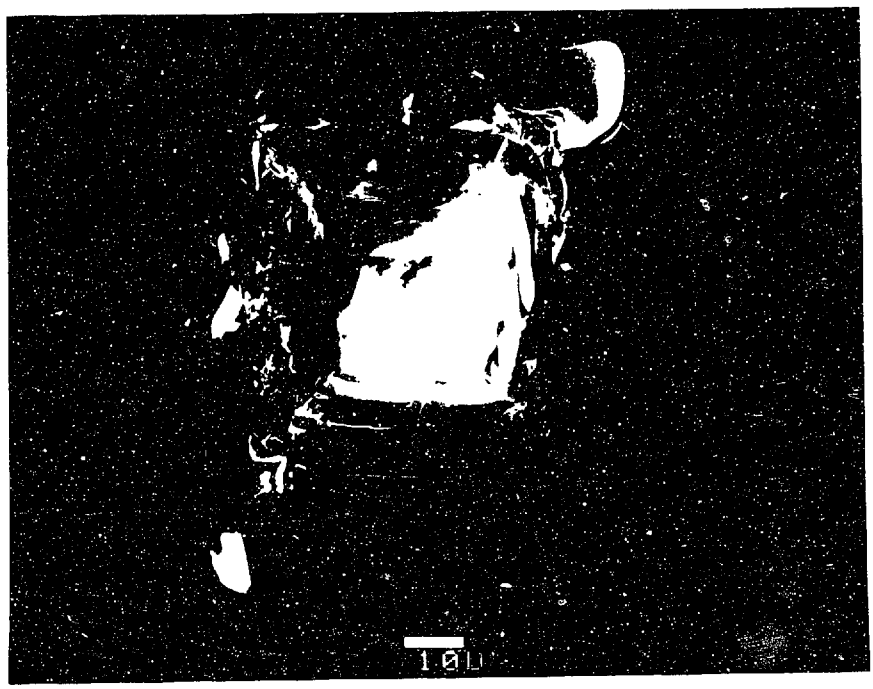

a.

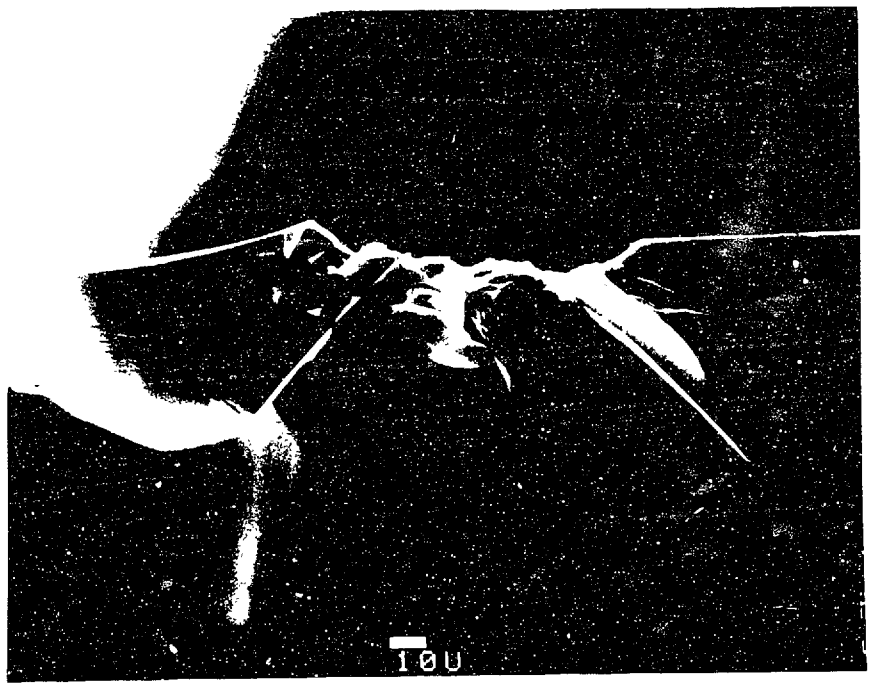

b.

Figure 5.2: SEM Micrographs of silica glass indented with 2000 gr. Vickers Indent. (a) top view and (b)cross-section

cracks are not under the same stress as the tips of the radial vents. Newman and Raju[69] have analyzed this problem using finite element techniques. According to their analysis, for a finite plate in bending, the stress intensity anywhere along a surface flaw can be described by equation 1.11 only when the applied stress, σ_{app}, is replaced by

$$\sigma_{act} = S_b[HF(c,a,t,b,\phi)] \qquad 5.3,$$

where σ_{act} is the "actual" stress applied at a certain point on the crack, S_b is the bending moment, and HF is a boundary correction factor, a function of the crack depth, c, half-width, a, plate thickness, t, width, b, and ϕ, the elliptical angle (See Figure 5.3)* . For a plate in bending, it turns out that the maximum stress is **always** at the surface until the flaw width is much greater than its depth. Thus, for a combined cone/radial system under bending, the stress, depending on HF, is often greatest at the tips of the radial cracks.

The stress distribution around a median/radial system can be visualized by the plot in Figure 5.4, where the boundary correction factor is plotted as a function of the elliptical angle for the conditions of a 5 Kg Vickers Indent in a 1" x 1" x 1mm silica slide (c = a =

* What Newman and Raju have really done is to define more precisely the constant, Ω, in Equation 1.11 to take into account the stress field gradient and free surface effects. To maintain consistency with their analysis, we will discuss the boundary correction factor in terms of modifying the applied stress. Whether the applied stress is multiplied by HF or the geometric constant is multiplied by $(HF)^2$ is irrelevant for calculating the stress intensity factor.

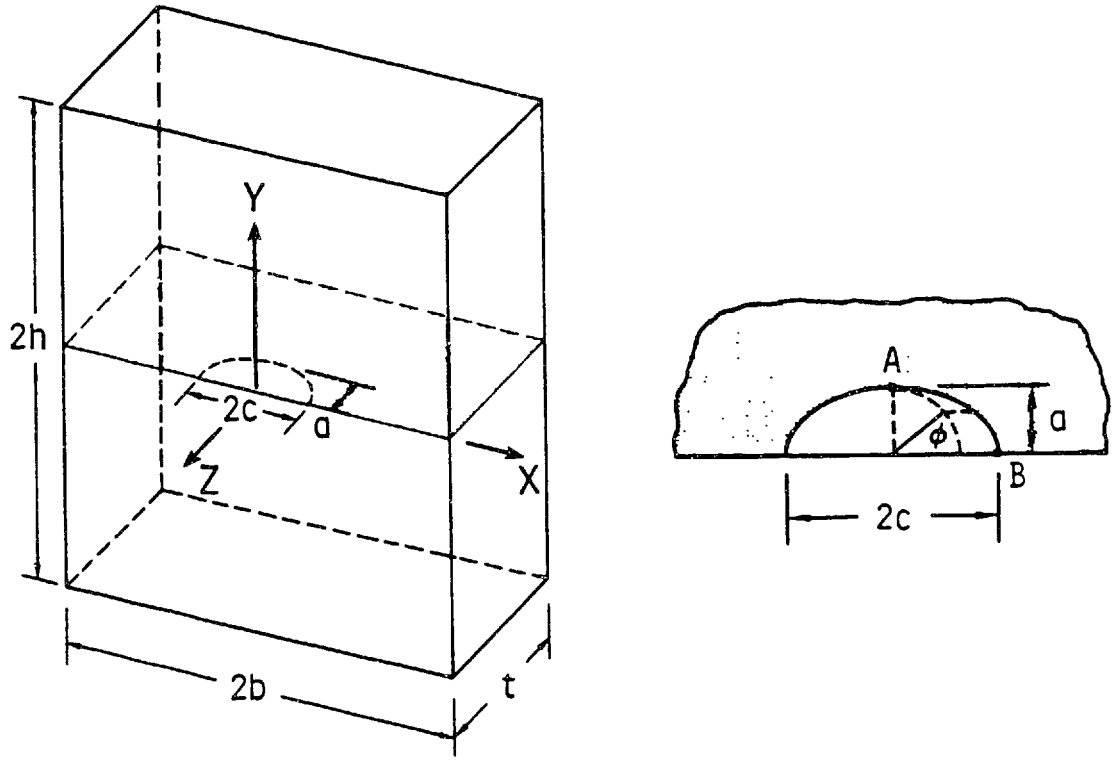

Figure 5.3: Definition of variables in Newman and Raju's analysis of stresses in a finite plate in bending. Notice that the variables a and c are reversed from Newman and Raju's definitions. (From ref. 69)

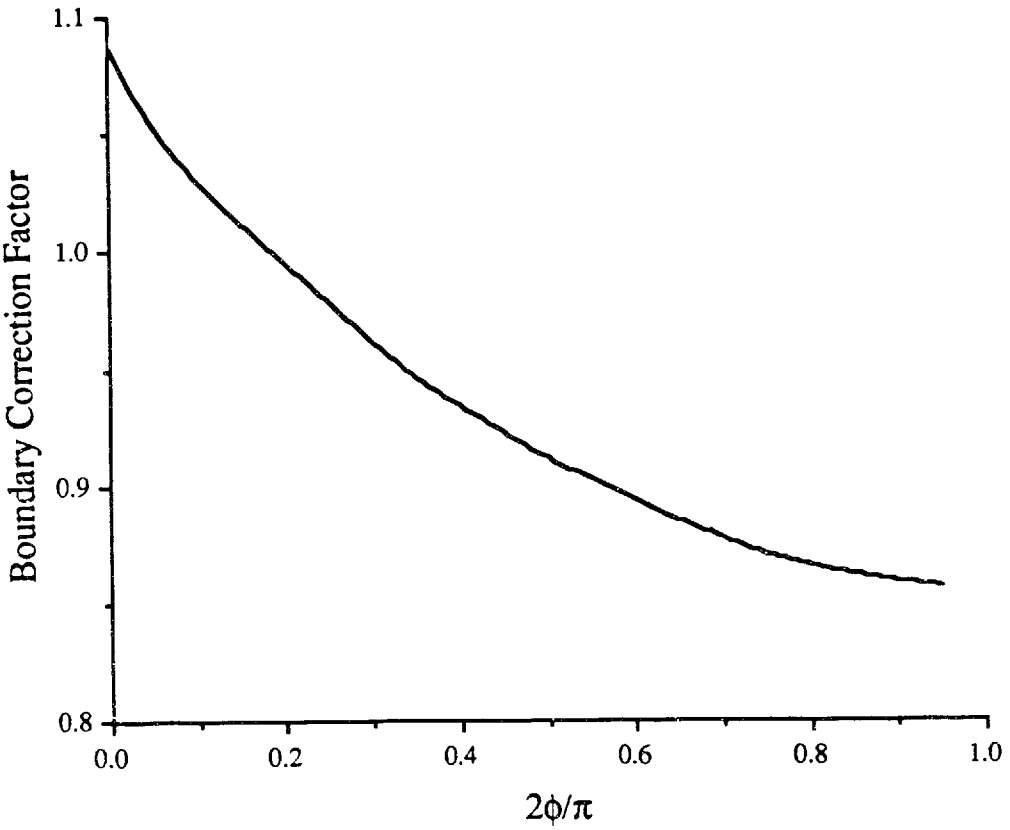

Figure 5.4: Boundary correction factor, HF, as a function of elliptical angle for the conditions of a 5 Kgr Vickers indent in silica.

130 μm). We see that the stress intensity at the tip of the radial vents surpasses the stress intensity at the median tips by more than 25%. Calculating the corresponding stress felt at the tip of 5 Kg cone crack is somewhat complicated by the facts that both I, opening, and II, sliding, modes of fracture are active, and that the crack will, in general, not propagate in bending along its original angle of inclination, α. These difficulties can be overcome by applying the method outlined by B.R. Lawn et al[70] to calculate an effective flaw length. (That is, the length of a perpendicular flaw, $\alpha = 90^{o}$, which would result in the same strength as the longer, but inclined cone crack.) For the 5 Kgr cone crack in silica (cone length = 170 μm and $\alpha \approx 35^{o}$) the effective flaw length is 95 μm. Applying Newman and Raju's method to this "effective" flaw, the stress at the tip of the cone cracks turns out to be about 30% less than the stress at the tip of the radial vents. For lighter loads, the shorter flaws remain near the surface, so that the bending stress gradient is not as noticeable; while for heavier loads the effect is more severe. In the following experiments, the effect ranges from about 15% for a 3 Kgr load to over 60% for a 20 Kgr load. We thus expect that in these experiments, the shorter radial vents will control fracture

In Figure 5.5, the fracture surface of an indented and then broken silica slide is shown. Indeed, the surface striations indicate that the surface (radial) flaw propagates much more rapidly and extensively during fracture than does the cone crack, even though the cone crack is initially longer.

Figure 5.5: Fracture surface of Vickers indented silica slide broken in bi-axial bending. Top edge is in tension; half of the indent is visible in the upper left corner of the photograph. Note rapid propagation of the surface flaw. (total sample width = 1mm)

5.2 Fracture Mechanics Model of Alkoxide Strengthening

Having established that indented plates fail under bending by the surface propagation of radial vents greatly facilitates the development of a model of the strengthening process, since solution penetration into the flaws can be, to a large degree, directly observed by looking at the indented and coated surface with the SEM. Based upon such observations, reasonable assumptions about solution/flaw interactions will be presented in this section. How these interactions are expected to affect material strength will be calculated, and these calculations will then be compared to experimental data and discussed in the subsequent sections.

SEM micrographs of 3 Kg indented silica slides, before and after coating, are shown in Figure 5.6. One half of the flaw has been drawn schematically in Figure 5.7, and labels have been assigned to important points along the length of the radial vent. The indenter imprint half-length (0 to d in Figure 5.7) is easily filled with the coating solution. However, This region is so deep (on the order of 25 μm for a 3 Kgr indent) that the coatings consistently crack during drying or firing (Figure 5.6); and we must therefore assume that this part of the total flaw length is unaffected by the coating solution. The main length of the radial vent, d to c, is apparently penetrated by the coating solution. We will assume, therefore, that this length is "healed" by the coating, but only up to an arbitrary length, l, beyond which the flaw is too narrow to to be perfetrated by the solution. (Since the flaw width there is probably on the order of the diameter of the coating oligomers, <100 Å, this portion of the flaw is invisible in the micrographs in Figure 5.6.) Finally, the length from c to c^*, which represents the flawed but optically healed length of the crack, is totally inaccessible to the coating solution.

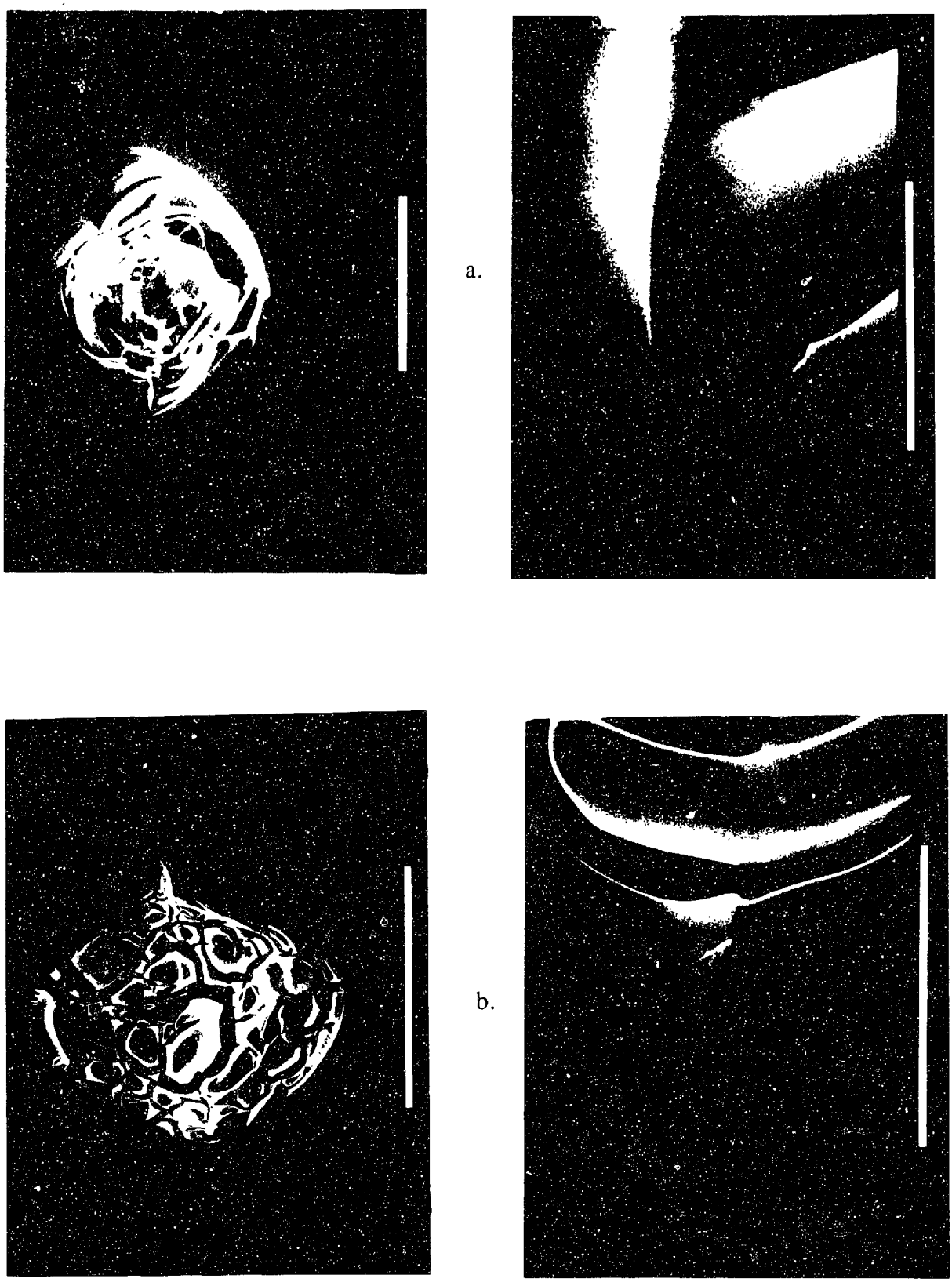

Figure 5.6: SEM micrograph (top views) of typical 3 Kgr Vickers indent in a silica slide (a) before and (b) after coating and firing. Micron markers are 100 μm on the left micrographs and 10 μm on the right.

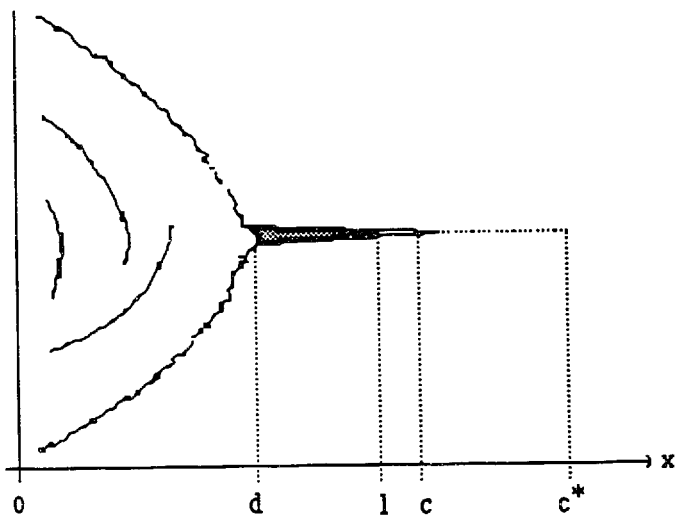

Figure 5.7: Schematic representation of Vickers indent in silica showing length of indent impression damage area, d, length to whcih the coating solution penetrates, l, length of optically healed flaw, c, and length of flaw at maximum indenter loading, c^*.

When a coated flaw such as the one drawn in Figure 5.7 is put under a uniform tensile stress, the region between c and c^* is expected to open up immediately, since it has very little mechanical integrity.[66] If we model the resulting flaw length between l and c^* as an ellipse, we arrive at the situation in Figure 5.8, in which there exist three critical points - d, l, and c^* - from which failure of the glass can result. The stress intensity at each of these points can be derived using Equation 1.11 if the characteristic length c is appropriately modified for each of the critical points. At d, the appropriate length is d (one half of the total impression length) and at both l and c^* the appropriate length is one half of the length of the ellipse, $(c^* - l) / 2$. Inserting these characteristic lengths into Equation 1.11, we obtain the following expressions for the stress intensities:

$$K_d = \sigma\sqrt{\pi\Omega d} \qquad 5.4$$

and

$$K_l = K_{c^*} = \sigma\sqrt{\pi\Omega\left(\frac{c^* - l}{2}\right)} \qquad 5.5.$$

By setting the stress intensity equal to the appropriate critical stress intensity (or toughness, T_o) equations 5.4 and 5.5 can be solved for the failure stress, σ_f. For failure at c^*, the toughness of silica, T_s, is appropriate, while for failure at d or l, an apparent sol-gel bridge toughness, T_b, is appropriate. Inserting these values, we obtain the following failure stresses:

$$\sigma_{f,d} = \frac{T_b}{\sqrt{\pi\Omega d}} \qquad 5.6,$$

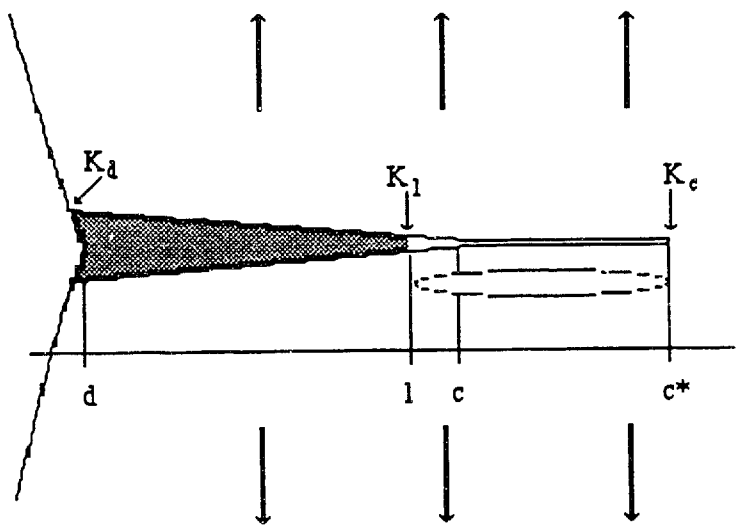

Figure 5.8: Schematic drawing of the surface of a Vickers indented silica plate under an applied tensile field. The flaw length between c and c^* is modeled as an ellipse, so that the three critical points for fracture are d, l, and c^*

$$\sigma_{f,l} = \frac{T_b}{\sqrt{\pi\Omega(\frac{c^* - l}{2})}} \qquad 5.7,$$

and

$$\sigma_{f,c^*} = \frac{T_s}{\sqrt{\pi\Omega(\frac{c^* - l}{2})}} \qquad 5.8.$$

Our task now is to try to write Equations 5.6 - 5.8 as functions of an experimentally controllable variable, such as the indenter load, P. If we can write $\sigma_{f,l}(P)$ and $\sigma_{f,c^*}(P)$, we can compare Equations 5.6 - 5.8 to experimental data and determine the most accurate fracture model. To do this, we need to obtain $c^*(P)$, d(P), and l(P), which can be accomplished in the following manner.

The easiest function to determine is the variation of the indent imprint length with load. One simply observes the length for different loads using an optical microscope, in the same way that the Vicker's Hardness Number is determined. Such data are plotted in Figure 5.9, from which it was determined that $d = \beta P^{2/3}$, where β has a value of 34 $\mu m\ Kg^{-2/3}$.

c^* is, of course, not visible on the sample surface; so that $c^*(p)$ is not so easily determined as d(P). It is possible, however, to determine c(P) easily by optical observations; and since it has been shown[71] that

$$\frac{c^*}{c} = (1 + \frac{\chi_e}{\chi_r})^{2/3} \qquad 5.9,$$

c^* can be determined with a knowledge of χ_e / χ_r. For the case of soda-lime-silicate glass, Marshall and Lawn[71] have determined this ratio to be 1.2. For silica, chipping around the indent relieves much of the residual stress; so that χ_r is expected to be lower than for soda-lime. χ_e is also expected to be lower for the silica experiments, since the radial vents important in this study do not extend as far as the median extensions examined by Marshall and Lawn. Fortunately, only the one-third power of the ratio is important in Equations 5.7 and 5.8. Hence, these uncertainties are relatively unimportant; and Marshall and Lawn's value of 1.2 will be used in the present model. Using Equation 5.9, $c^*(P)$ can be determined by measuring the residual crack lengths for different loads c(P), and inserting into Equation 5.9. c(P) is also plotted in Figure 5.9, from which it was determined that $c = \alpha P^{2/3}$, where $\alpha = 45\ \mu m\ Kg^{-2/3}$.

Determining the length, l, to which the coating solution penetrates involves the most uncertainty. Only the square root of l appears in Equation 5.9, however, so that uncertainties are somewhat lessened in importance. If the assumption is made that a coating solution penetrates until the width of the flaw is equal to the diameter of the molecules in solution,* we can determine the length of penetration from a quantitative knowledge of the flaw shape. For cracks under equilibrium conditions, one half the crack opening displacement u(x), where x the distance from the flaw origin (open end), is given by [72]

$$u(x,c) = \frac{T_{oc}}{E}\sqrt{\frac{8}{\pi}\ (c - x)} \qquad 5.10$$

* While this assumption may be a bit extreme, contact angle measurements have shown that the cleaned silica slides are wet by the TEOS solutions (contact angle ~ 10°). Thus, it is reasonable that coating solutions may be driven into the flaws by strong capillary forces.

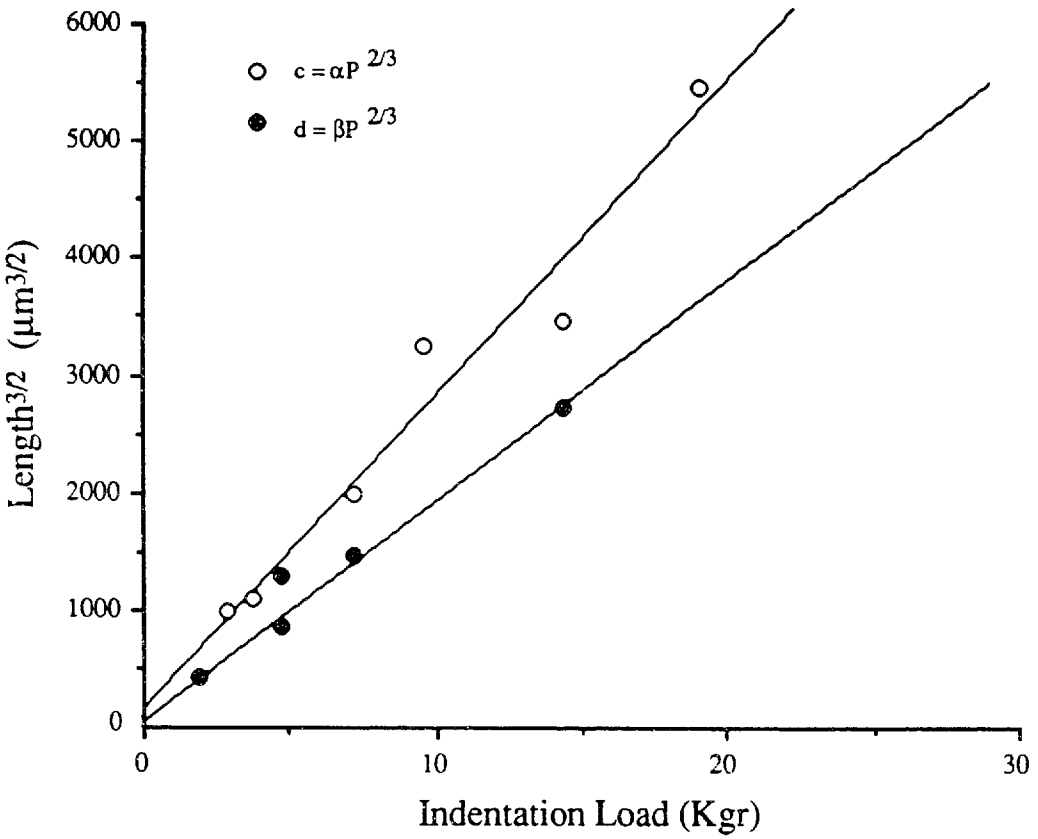

Figure 5.9: Indentation crack length, c, and indenter imprint damage length, d, as a function of indentation load for Vickers indented silica plates.

where T_{oc} is the toughness of the optically healed material and E is Young's modulus. At u(x,c) = r, x is, by our definition, equal to l, so that the length of penetration, l, is

$$l = c - \frac{\pi}{8}\frac{E^2 r^2}{T_{oc}^2} \qquad 5.11.$$

It is interesting that the penetration length, l, is given by simply the flaw length minus a constant. That is, the "gap" between the end of the coating solution and the end of the flaw is only a function of material constants, and, for a given molecule size, is always the same length ($\pi E^2 r^2/8T^2$) no matter how severe the flaw. This is a result of the fact that the penetration was determined from the equilibrium flaw profile, which would not be affected by the method and/or severity of the flaw-forming process.

Inserting Equations 5.9 and 5.11, along with d(P) and c(P), into Equations 5.6, 5.7, and 5.8 provides the predicted strengths as a function of indenter load,

$$\sigma_{f,d} = \frac{T_b}{\sqrt{\pi\Omega\beta P^{2/3}}} = \frac{T_b}{k_1 P^{1/3}} \qquad 5.12$$

where $k_1 = (\pi\Omega\beta P^{2/3})^{1/2}$ and

$$\sigma_{f,l}\,(\sigma_{f,c^*}) = \frac{T_b\,(T_s)}{\sqrt{\alpha P^{2/3}\frac{\pi\Omega}{2}[(1+\frac{\chi_e}{\chi_r})^{2/3} - 1] + \frac{\Omega\pi^3 E^2 r^2}{16 T_{oc}^2}}} = \frac{T_b\,(T_s)}{\sqrt{k_2 P^{2/3} + k_3 r^2}} \qquad 5.13,$$

where $k_2 = (\alpha\pi\Omega/2)[(1 + \chi_e/\chi_r)^{2/3} - 1]$ and $k_3 = \Omega\pi^3 E^2 r^2/16 T^2_{oc}$.

5.2.1 Molecular Size Effect

Equations 5.12 and 5.13 are very similar. The predicted strength in both is presented as the ratio of the sol-gel bridge toughness over the square root of a length term. The difference is in the length term. For failure at d, this term involves the indentation load raised to the two-thirds power. For failure at l or at c^* the length term involves two terms. The first, indentation load dependent term, represents the healed but re-opened length, c - c^*. The second term, dependent on the particle radius but not on the indentation load, represents the open length between l and c. Using a value of $\Omega = 0.3$ [73] and the previously discussed values for α, β, χ_e/χ_r, and T_{oc}, we find that $k_1 = 5.7 \times 10^{-3}$ $m^{1/2}Kgr^{-1/3}$, $k_2 = 1.4 \times 10^{-5}$ $mKgr^{-2/3}$, and $k_3 = 3 \times 10^{11}$ m^{-1}.

In Chapter IV we discused the apparent insensitivity of strengthening to particle size. Comparing Equations 5.12 and 5.13 now provides us with a reasonable explanation. If failure occurs from point d (Equation 5.12) the strength is independent of penetration ($\sigma \neq f[r]$). For failure at l or at c^*, if we substitute the appropriate values for k_2 and k_3, and a typical value of particle radius as 10 Å (see Table 4.1), the size term in Equation 5.13 is about two orders of magnitude smaller than the indentation load term. That is, the fraction of the total flaw length due to the optically healed material is much larger than that due to the gap between the penetration length and the end of the open flaw. Even if we use a conservatively high value of 30 Å for the radius, the size term is still about an order of magnitude smaller than the indentation load term.

Another consequence of the small size term is that differentiating between fracture at l (or c^*) and d may be difficult using the present fracture mechanics approach. This can be illustrated best by rearranging Equation 5.13 as follows:

$$\sigma_{f,l}\ (\sigma_{f,c^*}) = \frac{T_b(T_s)}{k_2 P^{1/3}}\left[1 + \left(\frac{k_3}{k_2}\right)\frac{r^2}{P^{2/3}}\right]^{-1/2} \qquad 5.14,$$

It is seen that the predicted strength at l (or c^*) follows the same functional relationship as at d, except for the denominator constant and a multiplicative factor, the size factor, f, which we define as $f = [1+k_3(r^2/P^{2/3})]^{-1/2}$. Again assuming a conservative particle radius of 30 Å, the size factor can be evaluated for a range of indenter loads and is plotted in Figure 5.10. It is apparent that f is significant only for very small indenter loads (P<1 Kgr). (For smaller, more realistic particle sizes, the critical load is even smaller.) In our experiments, the smallest indenter load used is 3 Kgr, since lighter loads do not always produce critical flaws after the samples are heated. Thus, for the loads used in this study, f ~ 1, so that Equations 5.12 and 5.14 predict the same functional dependence of strength on load, $\sigma \alpha P^{-1/3}$. The only difference is in the constants k_1 and k_2; and since we don't know T_b, we have no way of choosing between fracture Equations 5.12 and 5.14.

5.2.2 Residual Stress

Although fitting the data to the predicted strength equations may not lead to differentiation between fracture at l and fracture at d, we may obtain some useful insight into the strengthening process by attempting such a fit. In Figure 5.11, the strength of indented, coated and fired silica plates is plotted as a function of indentation load, along with plots of Equation 5.12 for three different values of T_b. (Assuming the size factor is insignificant, the plots also represent fits to Equation 5.13, for different values of T_b.)

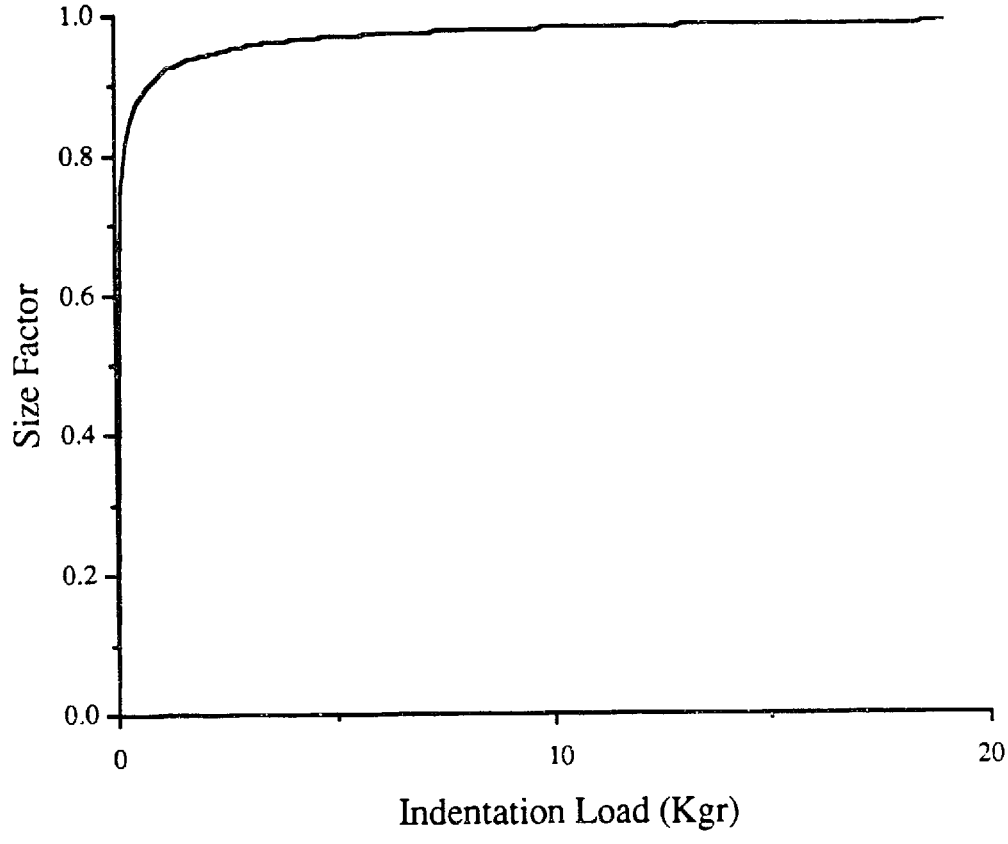

Figure 5.10: Size Factor, f, as a function of indenter load for 30 Å particles.

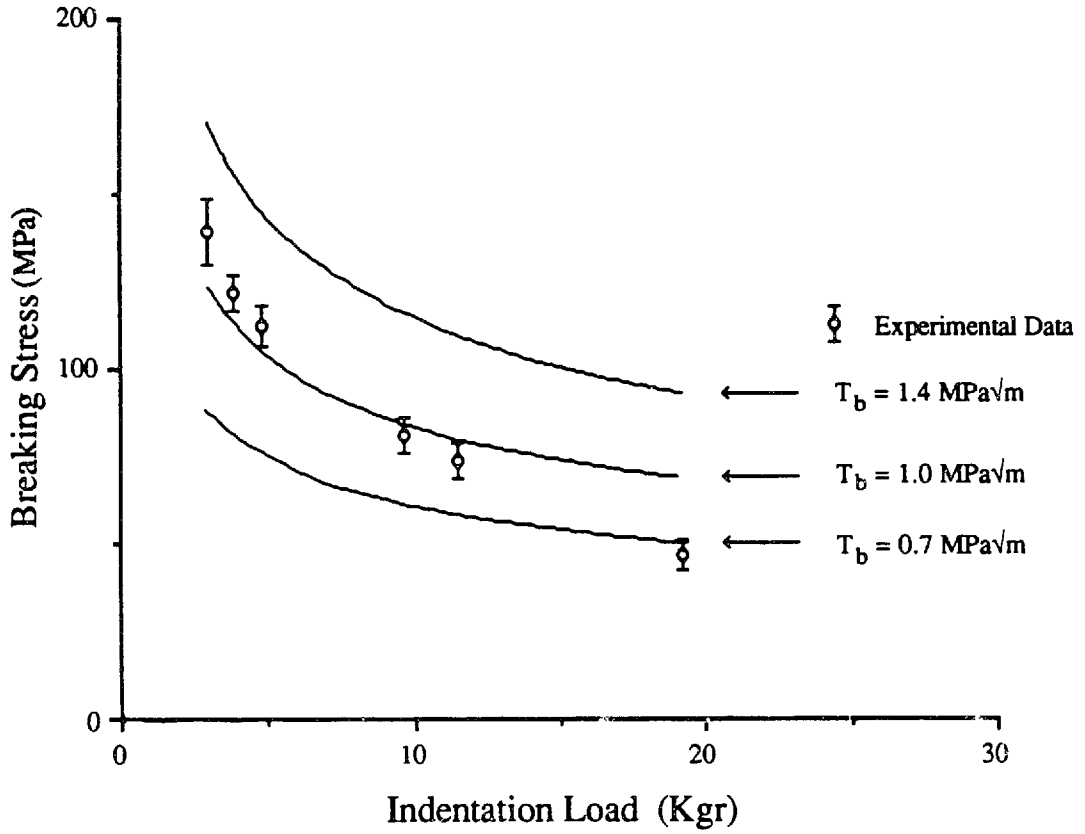

Figure 5.11: Breaking stress of indented, coated, and fired silica plates as a function of indentation load. Circles represent data points, and curves are plots of Equation 5.12, for T_b = 0.7, 1.0, and 1.4 MPa √m. (Assuming the size factor is negligible, the curves also correspond to plots of Equation 5.13 for T_b = 0.46, 0.65, and 0.92 MPa√m, respectively.)

The curves is Figure 5.11 follow the general trend in the experimental data. Quantitatively, however, the match between theory and experiment is marginal; for low values of toughness, the theory is in the right range, but the slope is too shallow; while for higher values of toughness the slope begins to fit the data, but the strength values are too high. This problem can be resolved by fitting the data to an equation of the form

$$\sigma = kT_bP^{-1/3} + C, \qquad 5.15$$

where C is an additive constant. Mathematically, this allows us to fit the slope by adjusting T_b and then to bring the curve down to realistic strength values by adjusting the constant C. Physically, C represents a residual stress component in the fracturing material. This is demonstrated by the plot in Figure 5.12, where experimental data for coated and uncoated samples are plotted as a function of $P^{-1/3}$.

As expected from fracture mechanics theory,[64] the strength of indented but uncoated slides increases linearly with $P^{-1/3}$, and extrapolates through the origin. This merely indicates that for an "infinite" indentation load ($P^{-1/3} = 0$), the sample starts out with zero strength. For the coated samples, on the other hand, the samples have a **negative** strength at $P^{-1/3} = 0$; i.e., they start out under an effective tensile stress. The value of this tensile stress is given by the y-intercept in Figure 5.12, -58 MPa. Inserting this value of C into Equation 5.15, we find that

$$\sigma = \frac{T_b}{kP^{-1/3}} - 58 \text{ MPa} \qquad 5.16$$

where $T_b = 1.6$ MPa $\sqrt{m}$ to fit Equation 5.12 and $T_b = 0.9$ MPa $\sqrt{m}$ to fit Equation 5.13. The experimental data are replotted, along with a plot of Equation 5.16, in Figure 5.13.

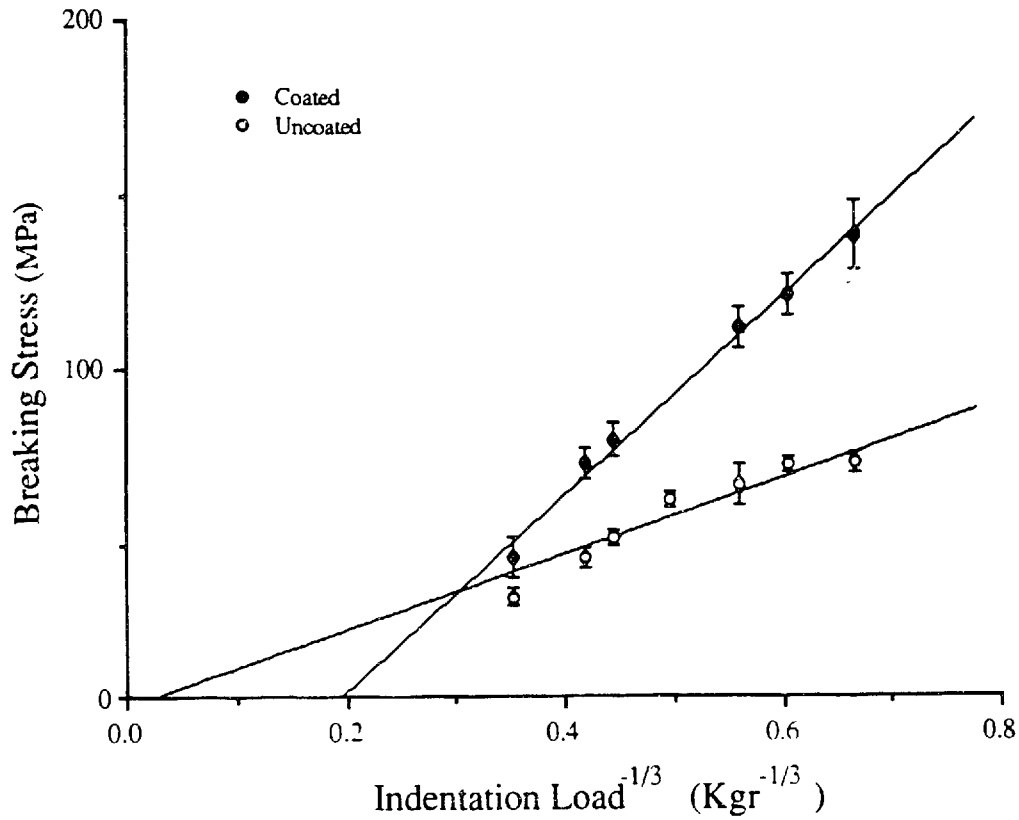

Figure 5.12: Breaking stress as a function of indentation load to the one-third power for coated and uncoated silica plates.

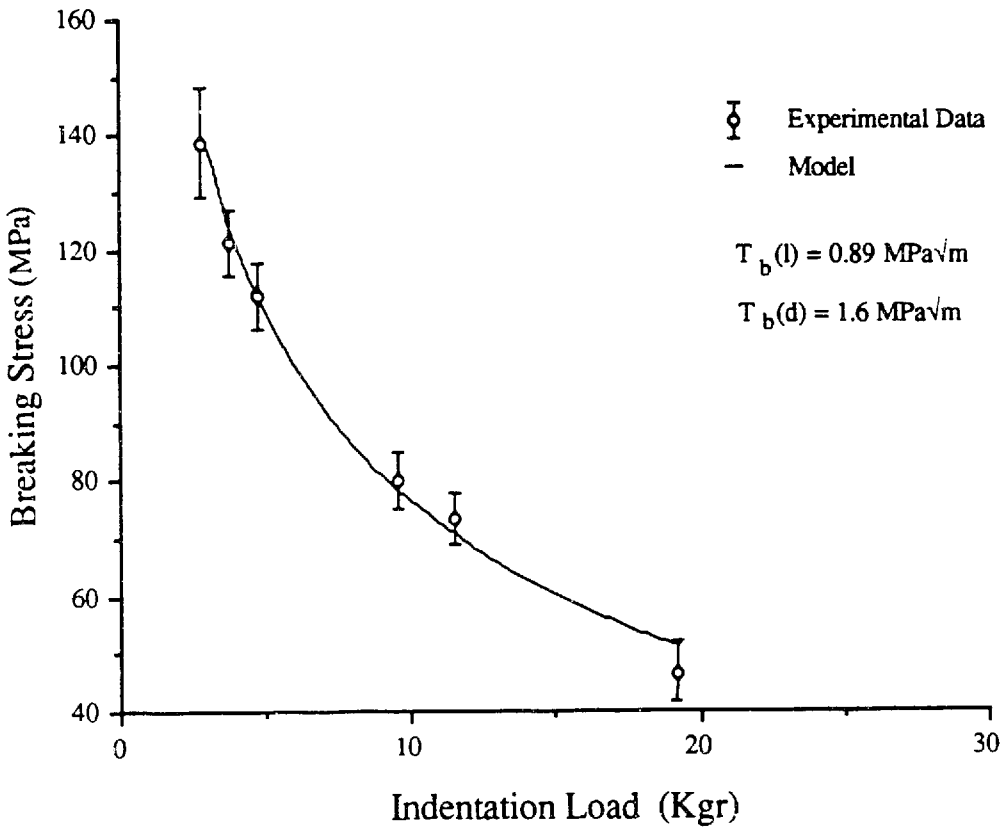

Figure 5.13: Breaking stress versus indentation load for indented, coated, and fired samples. Line is experimental fit of Equation 5.16.

5.2.2.1 Source of Residual Stress

In the previous section we determined that a significant residual tensile stress is produced in sol-gel strengthened silica. In this section, we will try to pinpoint where the residual stress exists and how it is created. Information will also be gained on the fracture path and flaw-tip geometry.

The existence of the residual stress term in Equation 5.16 implies that the point of the flaw/coating composite that controls failure is under tension during fracture. In our model there are only three points to examine - d, l, and c^*. Failure at d and l imply that the sol-gel bridge material is under tension, while failure at c^* would imply that the bulk silica is under tension. Fracture at these three points is drawn schematically in Figure 5.14. Fot the case of failure at c^*, it is difficult to envision a process by which the bulk silica would be left in tension after coating and firing. As we will discuss in detail in the following paragraphs, tension in the bridge material is quite feasible. We conclude, therefore, that the strength of sol-gel strengthened glass is controlled by failure of the sol-gel bridge material, and not by flaw propagation into the bulk silica.

A tensile stress in the bridge material might result from one, or both, of two processes - either a CTE difference between bulk silica glass and the sol-gel coating material or the large shrinkage of the coating during drying and sintering. For the stress to result from CTE mismatch, we can easily calculate the difference in CTE, $\Delta\alpha$, needed to generate a coating stress, $\sigma_{coating}$, of 58 MPa, since

$$\sigma_{coating} = E\Delta T\Delta\alpha(1-3j+6j^2) \qquad 5.17,$$

where ΔT is the temperature difference between room temperature and the temperature at which stresses begin to anneal out and j is the ratio of coating to base glass thickness.[95]

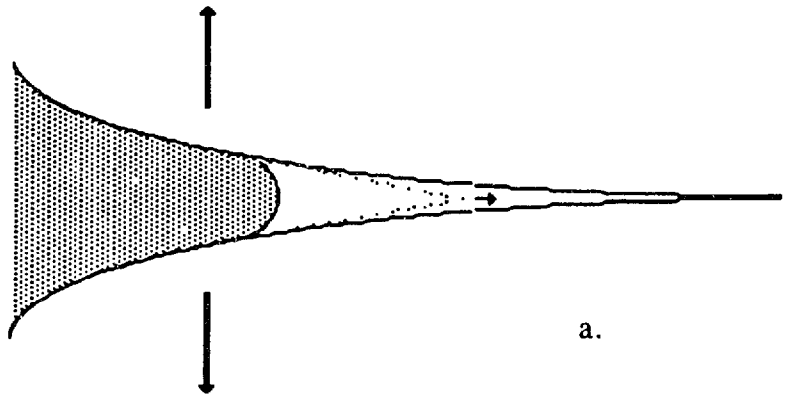

Failure at c^*

σ_r in bulk glass

a.

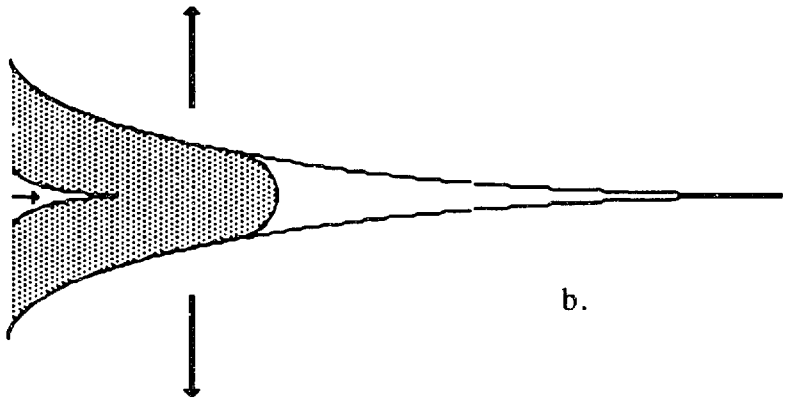

Failure at d

σ_r in bridge

b.

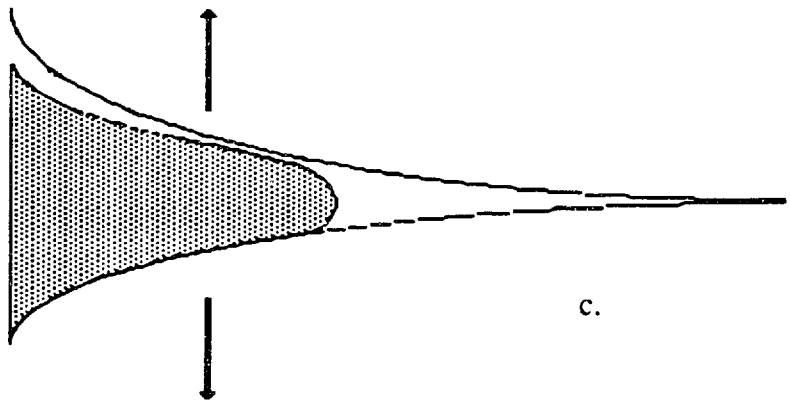

Failure at l

σ_r in bridge

c.

Figure 5.14: Schematic drawing of fracture originating from (a) d, (b) l, and (c) c^* in sol-gel strengthened glass.

with $\Delta T = 1000\ ^oC$, $E = 10^7$ psi, and $j \sim 0$, we find that a CTE mismatch of roughly $1x10^{-6}/^oC$ is needed to generate the tensile stress. This value is much higher than one could reasonably expect from differences in water content between the sol-gel bridge material and the bulk silica; differences in water content usually result in a $\Delta\alpha$ of at most 0.01 /°C - 0.05 /°C. [74]

It would also be possible to create a relatively large CTE mismatch with small changes in coating composition. In fact, washing abraded rods in an alkaline solution prior to coating reduces the strengthening obtained by about 50%. For the straight silica on silica coatings, however, the strengthening appears to be independent of the purity of the TEOS,[§] so that the major portion of the residual tensile stress is probably not due to compositionally produced CTE mismatch.

It appears that the tensile stress must be a result of the large shrinkage which the coatings undergo during drying and sintering. Evidence of the effect of this tensile stress can be seen in Figure 5.15, where both the strengthening and the densification of TOES coated silica plates are plotted as a function of time in furnace. It is apparent that the strengthening saturates **before** the coating fully densifies. This behavior would arise if the densification of the coating not only enhances strengthening but also creates the tensile stress; as densification continues, the tensile stress eventually overwhelms the strengthening effect, and the sample strength levels off before reaching full density. In fact, if we were to extrapolate the strengthening in the first two minutes up to the time at

[§] Coating solutions prepared with distilled TEOS provided the same strengthening as solutions prepared with untreated TEOS, as received from the manufacturer, Alfa Chemical.

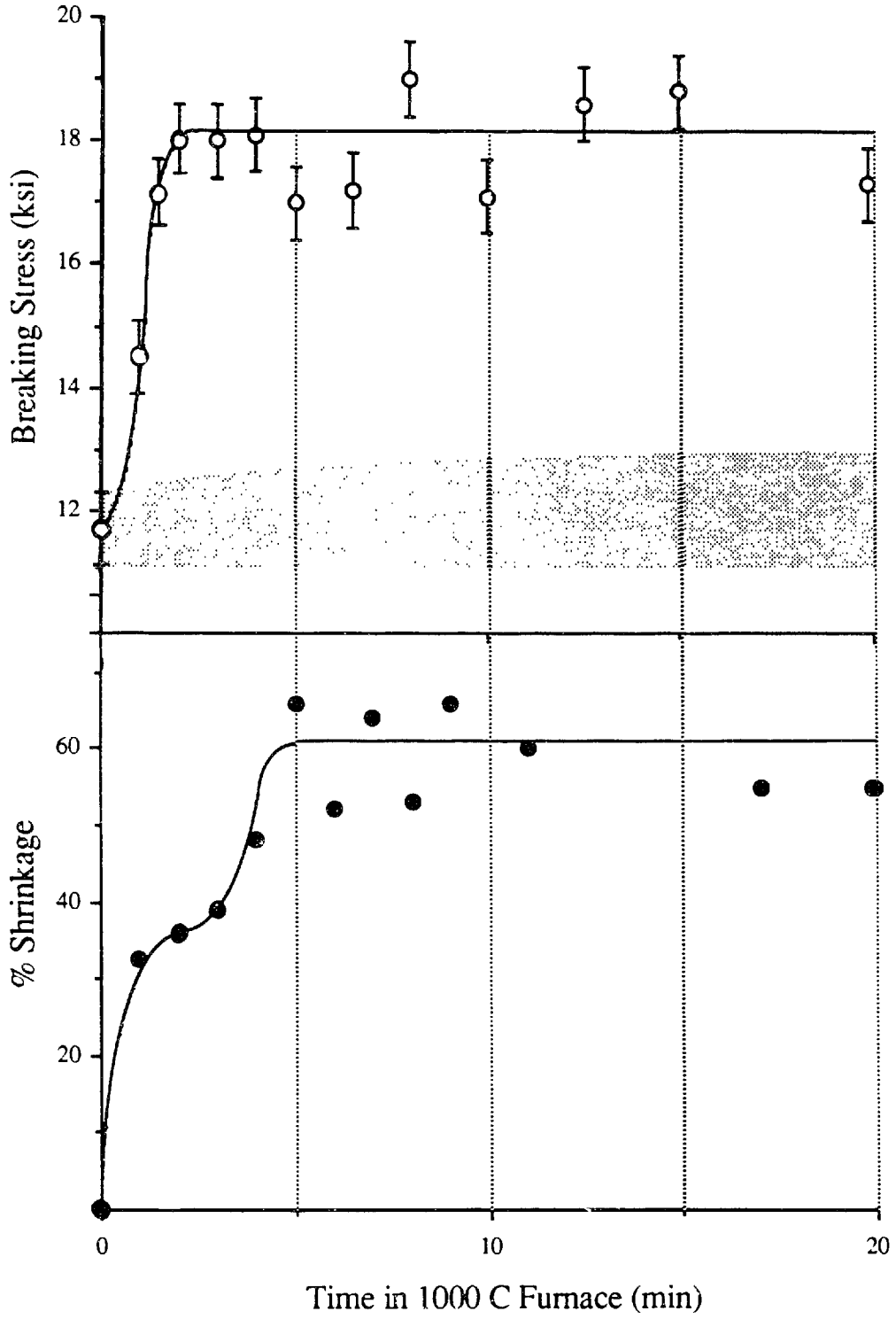

Figure 5.15: Strengthening of 2 Kgr Vickers indented and coated silica plates as a function of time in furnace (top) and shrinkage of the coatings (bottom).

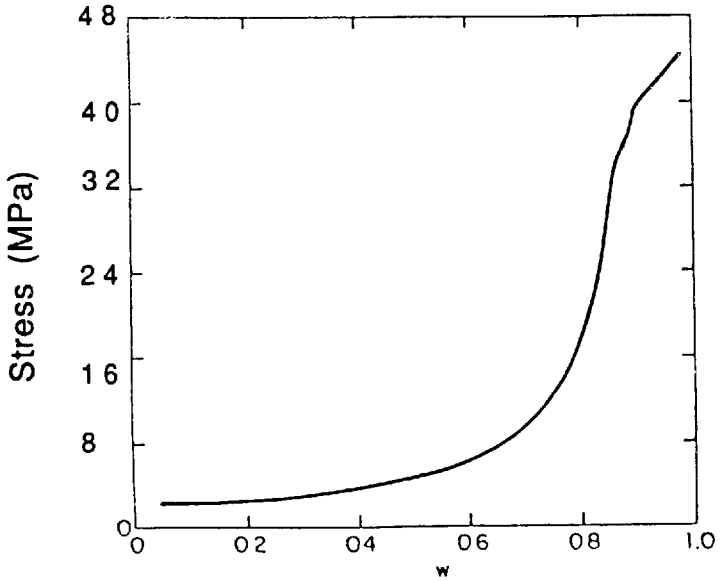

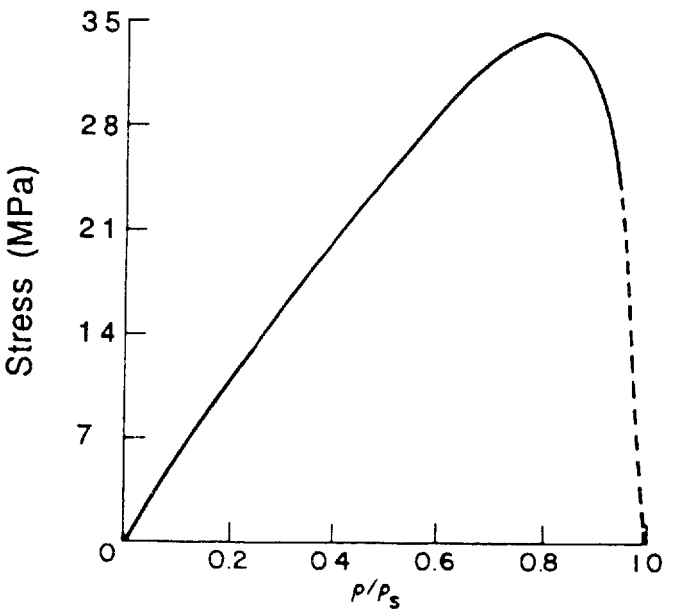

Figure 5.16: Stresses in the coating/substrate plane formed (a) during drying as a function of fraction weight loss during drying(from ref. 96) and (b) during sintering as a function of relative density (from ref. 97).

which densification occurs (about five minutes) we would see that the potential (tensionless) strengthening is about 30 ksi, which is roughly equal to the actual strength plus the calculated residual tensile stress.

The above explanation of the tensile stress would adequately explain the data except for one very important question: Why is the tensile stress not annealed out when a coating is fired to a temperatures (1000 °C) which has been shown to be high enough for the massive structural rearrangement necessary for sintering? To answer this question, we will have to look a bit more closely at the stresses generated in a dried and sintered sol-gel film.

Scherrer has analyzed the stresses which develop in a coating during drying[96] and sintering[97] of gel films. For both analyses, a well-adhering film is assumed, so that strains, ε_x and ε_y, in the x-y plane (parallel to the substrate/interface plane) are zero. The film is allowed to shrink unconstrained in the z-direction, so that σ_z, the stress in the z-direction, is zero. For a "typical" alkoxide-derived silicate coating,[96] the drying stress in the x-y plane at the coating/substrate interface is plotted as a function of weight loss in Figure 5.16a. We see that, when fully dry, a significant stress (~45 MPa) is developed at the coating/substrate interface. During sintering, a similar plot, Figure 5.16b, shows the development of stress as a function of relative density. At its maximum point, 81% of full density, the stress is about 35 MPa. The orientation of these stresses is depicted in Figure 5.17a. It is interesting that the sum of the stresses (80 MPa) is relatively close to out calculated residual stress, 58 MPa.

the above stress analyses apply to a film which is unconstrained in the z-direction. A coating within a flaw, however, is severely restricted from shrinking in the z-direction as a result of attachment to both sides of the flaw. The stress in the z-direction is,

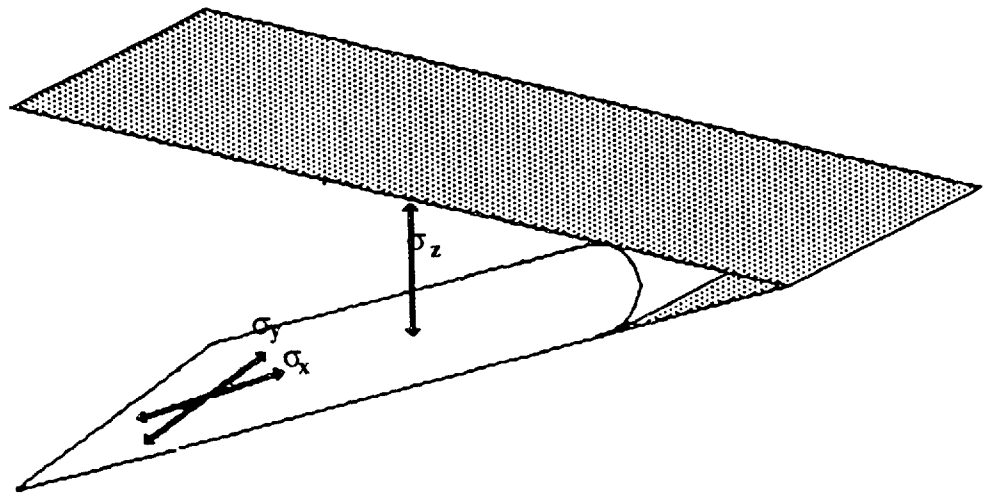

Figure 5.17: Schematic drawing of potential stresses formed during drying and sintering in the x-y and z-directions.

therefore, expected to be significant. To estimate the magnitude of this stress, we can apply Scherrer's analyses with a rotation of the strain constraints; If we assume that the bonding of the coating to both sides of the flaw forces strain in all planes parallel to z to be zero, we apply Scherrer's analyses with $\varepsilon_z=\varepsilon_y= 0$ and $\sigma_x= 0$. As before, this would result in a drying stress of about 45 MPa and a maximum sintering stress of 35 MPa, this time in the z-direction, as depicted in Figure 5.17. In reality, of course, the coating is not at all free to move in the x-direction, so that $\sigma_x \neq 0$. This approximation therefore gives a lower bound to the stresses developed in the z-direction.

We are now ready to address the question of how these stresses remain, even after the coating densifies, as indicated by Figure 5.15. There are two possibilities. The first possibility is that the tensile stress in the z-direction never goes to zero (as indicated in Figure 5.16b) because the coating doesn't densify within the flaw. Recall that the densification data plotted in Figure 5.15 are from a coating which was unconstrained in the z-direction. As we discussed above, this is not the case within the flaw; there is significant tension which suppresses shrinkage. Thus, after a few minutes at 1000 °C the unconstrained film may dense while the constrained film within the flaws may only partially densified. Within the flaw, it quite possible that densification stops at some point around the maximum tensile stress shown in Figure 5.16b. As a result, a residual tensile stress in the z-direction would exist throughout the film thickness (Figure 5.18).

It may also be possible to generate significant residual tensile stresses along the coating/substrate interface. Normally, stresses developed during sintering go unnoticed,

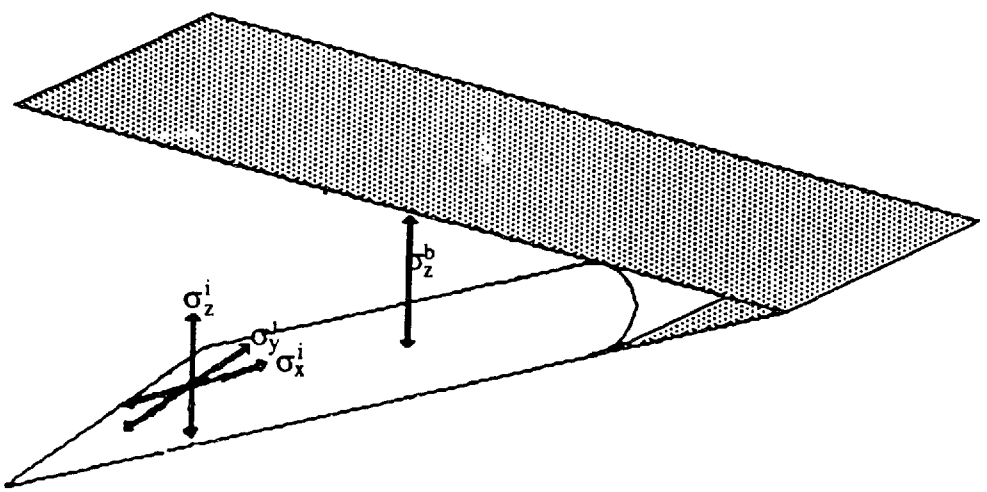

Figure 5.18: Schematic drawing of potential residual stresses throughout the bulk of the coating and in the x-y plane.

since sintering occurs at such a low viscosity that structural relaxation, which relieves the stresses, is virtually instantaneous.[98] In alkoxide-derived glass, however, the driving force for densification is so great that sintering can occur at viscosities significantly higher than is normally required.[98] At such high viscosities, structural relaxation is not at all instantaneous, and sintering and relaxation probably occur concurrently. In addition, it has been shown that the viscosity of TEOS-derived silica is extremely time-dependent, rising from about 10^{14} P to that of silica, about 10^{14} P after firing for 1000 min at 800 °C.[99] As a result, there is probably a significant viscosity gradient across the thickness of the film; when firing begins, the first few atomic layers of the coating, which are attached to the silica substrate, probably have a viscosity similar to that of fused silica. Meanwhile, the remaining, unattached, portion of the coating could have a viscosity two orders of magnitude less. Thus, sintering, and structural relaxation could occur throughout the bulk of the coating, while the interface region is at too high a viscosity for any substantial stress relief to occur. Residual stresses in both the x-y and z-directions, localized at the coating/substrate interface, would result (Figure 5.18).

It is worth noting that the explanations given above also account for the unexpectedly high values of T_b (both greater than the toughness of fused silica) obtained by fitting the experimental data to Equation 5.16. Both explanations of the residual stress would require that samples fail by flaw propagation through undensified material. Such porosity is expected to blunt crack tips and significantly change the value of Ω, which we have assumed to be constant throughout. Hence, T_b is probably better thought of as a work of fracture than as the critical stress intensity factor for the bridge material.

5.2.2.2 Stress Corrosion

In Section 1.3.2 some effects of stress corrosion were discussed. Static fatigue, it will be recalled, is a process whereby the strength of glass degrades with time under a subcritical loading. In the case of sol-gel strengthening, the fact that the rate of stress corrosion is a strong function of the stress intensity turns out to be critical, since constant driving force for sub-critical crack growth is provided by the residual stress. Thus, a piece of sol-gel strengthened glass under no apparent external load may experience severe strength degradation.

By integrating Equation 1.14 with the appropriate substitution made for the stress intensity factor as a function of crack length (Equation 1.11) Wiederhorn[28] has derived the total time to failure, t,

$$t = 2RTc/K_I bv_1 \qquad 5.18,$$

where b is equal to n/K_c in Equation 1.14 and v_1 is the initial crack velocity. The initial crack length can be determined from Equation 1.11, using the liquid nitrogen strength of coated and fired samples, σ_{LN2}, to determine the stress corrosion free strength, so that Equation 5.17 can be written as,

$$t = \frac{2RTT_b^2}{\sigma_{LN2}\sigma_r \pi \Omega n a_2}\left[\exp\left(\frac{E_2}{RT} - \frac{n\sigma_r}{RT\sigma_{LN2}}\right)\right] \qquad 5.19$$

where σ_r is the residual sol-gel coating stress and Equation 1.14 has been substituted in for the initial velocity.

Using Wiederhorn's[28] experimentally determined values for the stress corrosion constants for silica, $\sigma_{LN2} = 29$ ksi, and our calculated residual stress of 58 MPa, the time to failure is plotted for a range of assumed bridge toughnesses in Figure 5.19. Experimentally, we find that coated rods left in the lab for about two days are indistinguishable from uncoated rods. That is, it takes about two days for static fatigue to completely eliminate the strengthening. With this result, we can calculate the bridge toughness necessary to cause failure in about two days. It is apparent in Figure 5.19 that this toughness corresponds closely to the toughness, 0.89 MPa$\sqrt{m}$, calculated for fracture at l. Extreme caution must be exercised here, however, since the time to failure is so sensitive to uncertainties in the residual stress, which appears in the exponent. Precision in the geometric constant W is also a concern, since it is not under the square root in Equation 5.19, as it is in Equations 5.12 and 5.13. This would not be an issue if we could establish that Ω maintains its value of 0.3; but we already indicated in the previous section this is probably **not** the case, and the high values of T_b are likely a result of a substantial decrease in Ω.

The effects of static fatigue are also evident in the scatter of strengthening data in Figures 3.3 and 5.15. In these figures, each data point and error bar represent the mean and one standard deviation, respectively, of a set of at least eight samples. From one set of samples to the next, however, the mean values often deviate by more than one standard deviation, even at long firing times, when the thermal effects should have come to equilibrium. In Figure 5.15, for example, the standard deviation of any particular set of samples is about 1.5 ksi after 5 minutes at temperature. The mean values of the data, on the other hand, vary from 17 to just over 19 ksi after 5 minutes at temperature. This effect is probably due to our allowing each set of samples to sit for anywhere from 0.5 to

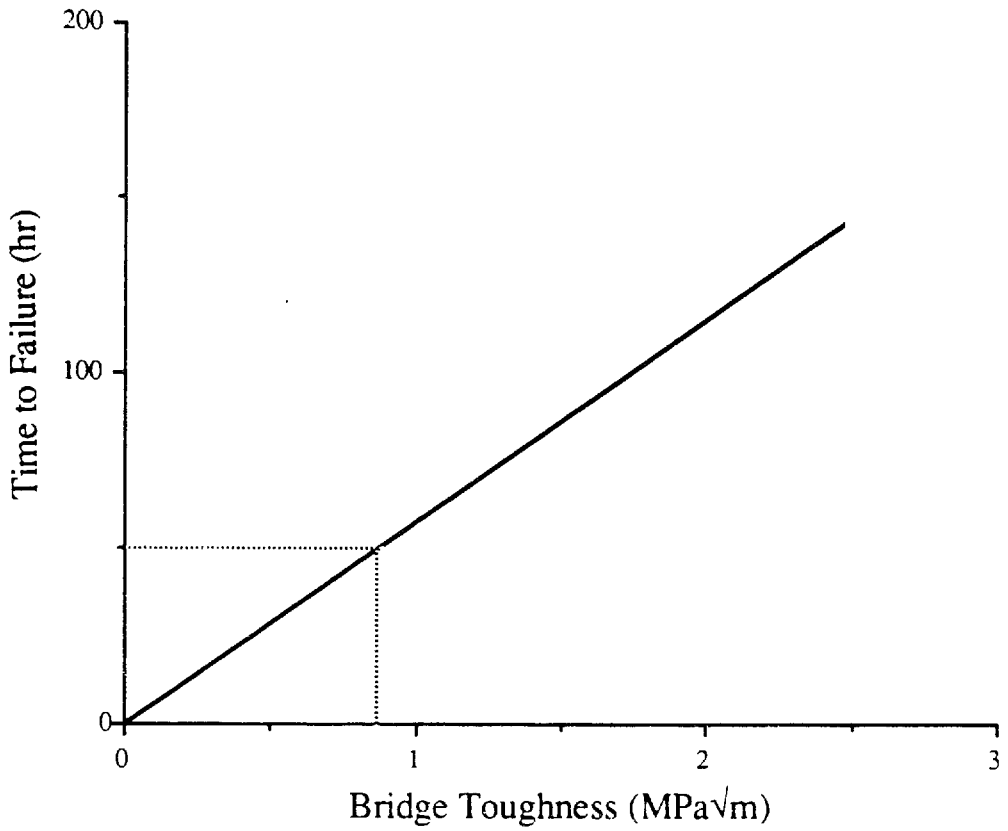

Figure 5.19: Time to failure predicted from Equation 5.19 for a range of assumed bridge toughness values.

about 6 hours before breaking. Because of this "ageing," the severity of static fatigue is expected to vary from one set of rods to another.

To estimate the magnitude of this effect, we recall that the strength of a flawed sample is proportional to the inverse of the square root of the flaw length. The flaw length is, to a first approximation proportional to time (assuming a constant crack velocity for the short times involved) so that the strength of aged samples should be proportional to the inverse square root of time. This is plotted in Figure 5.20 for the boundary conditions of no strength degradation at t=0 (breaking stress = 20 ksi) and complete bridge failure at t = 50 hrs (breaking stress = 8 ksi). For our range of ageing times, we see that the mean strength deviation should be just under 3 ksi, as we observe in Figures 3.3 and 5.15.

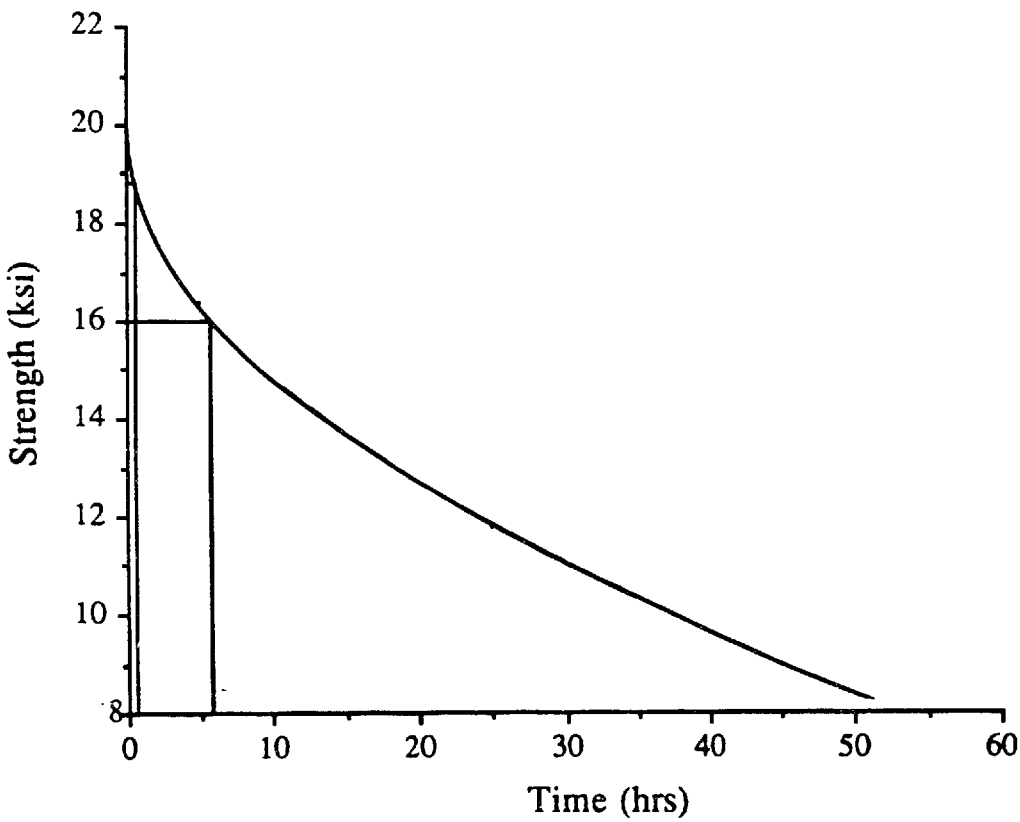

Figure 5.20: Approximate decrease in strength of sol-gel strengthened silica as a function of ageing time. Shaded area represents the approximate range of times samples were aged before strength testing.

VI. Conclusions and Directions for Future Research

The investigations described in the preceding chapters are summarized in the following general conclusions:

1. TEOS-derived coatings can be used to strengthen silica glass by over 120%, from 9 to 20 ksi.

2. Surface passivation - either chemical or physical - is apparently not involved in the strengthening process.

3. The strengthening mechanism involves penetration of surface flaws by the coating solutions.

4. The magnitude of the strengthening is not limited by the alkoxide solution chemistry as long as there exist an adequate concentration of silanol groups in the coating solution and on the substrate surface.

5. A large residual tensile stress (about 8.5 ksi) is developed in the coatings, even after firing to 1000 °C.

6. The residual tensile stress imposes severe limits on the level of strengthening obtained, and renders the strengthened material extremely susceptible to static fatigue.

6.1 Topics for Future Research

While a wide range of possible follow-up projects could be created from this work, five question seem particularly interesting. First, How universal is the healing effect ? In the experiments described in this thesis, only two types of flaws - alumina

abrasions and Vickers indents - were explored. It is easy to envision a list of abrasion processes which would not at all resemble the relatively well-controlled flaws dealt with in these experiments. Such an investigation could start with a closer look at the flaw characteristic ratio, χ_e/χ_r. This fraction represents the ratio of healed (unpenetrable) flaw length to open (penetrable) flaw length. In the analysis, it was assumed to be constant. For the purposes of the derivation in Chapter V, this was probably a reasonable simplification. Allowing the ratio to vary (in a controlled manner) may shed further light on the details of the model presented in Chapter V.

Second, an accurate knowledge of the sol-gel bridge toughness, T_b, would be interesting from both a theoretical and a practical view. Theoretically, the toughness could provide information about the microporosity of the coating along the interface, and about the nature of flaw propagation through this region. From a practical standpoint, T_b would be quite useful in failure prediction. The main problem in determining T_b can be appreciated by considering Equation 5.15. Using this equation, a plot of σ vs $P^{-1/3}$ could (and did in Chapter 5) provide the residual stress, C, and slope, kT_b. The slope is, unfortunately, composed of two variables, T_b and $k(\Omega)$. This problem can be overcome by obtaining an independent measure of the relation between T_b and k, which could be accomplished by accurately monitoring the static fatigue behavior of a coated sample, and then determining an appropriate ratio of T_b^2/Ω. An independent measure of the residual stress would also solve the problem. This could be accomplished by measuring the lattice parameter of small crystalline inclusions,[100] using an imbedded pressure transducer,[100] or measuring the curvature of a thin substrate after coating one side.

Third, an experimental determination of the penetration of alkoxide solutions into flaws would be interesting. High resolution scanning electron microscopy would seem to

provide the most natural approach to this problem, although a host of problems - most notably the difficulty in obtaining proper sample sections and the difficulty in obtaining contrast between a silicate coating and a silicate substrate - await the researcher. The use of scanning Auger microscopy mapping, along with the standard SEM, might be helpful.

Fourth, a detailed analysis of the fracture path of coated samples could provide information on the importance of the different residual tensile stress components (Figures 5.18 a and b) and could help direct future research toward optimizing the strengthening. If it can be shown that fracture occurs through the bulk of the bridge material, as opposed to along the coating/substrate interface, then one can infer that the residual stresses in the z-direction (Figure 5.18a) are more severe than the x-y plane stresses caused by anisotropy in the viscosity of the coating during firing (Figure 5.18b). If the opposite is the case, i.e., if the x-y plane stresses are shown to be limiting, then investigations into different surface preparation techniques would be of great interest.

Finally, a question which should have been asked from the outset but was conveniently ignored is: Does one really need to use alkoxide derived coatings to produce the effects described here? The zeroth order answer appears to be yes, at least in light of the data on SnO_2 and TiO_2 hot end coatings, which suggest no signs of flaw healing. Perhaps the size of the SnO_2 particles is too large to penetrate effectively; perhaps the coatings are not dense; perhaps the coatings themselves are flawed; perhaps the coatings do not adhere sufficiently well to the substrate; perhaps the coatings crack on cooling. This is a large question which is of interest not only for this particular application, but also for the sol-gel field as a whole. Justification for the use of alkoxides over aqueous salt solutions is a question in almost every application.

6.2 Overall Practical Implications

For the alkoxide strengthening technique to be a viable candidate for commercial application, the most immediate issue to be addressed is the residual stress. A process which strengthens for only forty to fifty hours is of very limited practical importance. One must develop coatings which undergo very little, if any, shrinkage during drying and densification. For silica coatings, Iler[75] has shown that coatings with a variety of pre-fired densities can be produced from aqueous sols; some of these even approach theoretical density in the as-coated state. The use of organically modified silicate coatings[76] offers another potential route for applying nearly-dense coatings, although the high CTE of these materials may limit their usefulness.

For practical application of soda-lime-silicate substrates, the firing temperature of the coatings must be lowered. For simple strengthening as discussed in this thesis, changing the coating composition to match that of the substrate should be adequate. Investigating the use of more exotic densification techniques, such as flash heating, laser curing, and plasma densification, might allow the use of high T_g coatings on lower T_g substrates.

To isolate the flaw healing effects, coating and substrate CTE were matched in the experiments described in this thesis. For practical application, this would be a waste. One could get a bonus in strengthening by intentionally mismatching the substrate and coating CTE's to produce a compressive stress in the substrate. Interestingly, an unexpected consequence of the residual tensile stress arises here, in that the application of a high CTE coating, which is needed to put the base glass in compression, would increase the residual tensile stress in the sol-gel bridge. To reduce the residual tensile stress, a low CTE coating is desirable. Thus, a dual-layer coating would probably be

optimal; the first, low CTE film to reduce the residual tension, and the top, high CTE layer to put the substrate under compression.

Finally, if used without some sort of abrasion resistant treatment, a sol-gel strengthening glass is just as susceptible to abrasive damage as an untreated glass. To preserve the strengthening, a protective coating is imperative. Using sol-gel processing, protective coatings might take the form of hard, abrasion resistant coatings, soft, lubricious coatings, organically modified silicate coatings, or a number of other possibilities. In Appendix C, issues concerning the production of hard, abrasion resistant oxynitride coatings will be discussed.

A variety of interesting topics for future research has been suggested by this work. In addition, if a few key issues are addressed, this novel approach to glass strengthening may have practical consequences in the future.

Appendix A. A Quantitative Comparison of the Power and Exponential Laws of Stress Corrosion

In Section 1.3.2 the power law (Equation 1.14) and exponential law (Equation 1.13) of subcritical crack growth were introduced. The fact that both of these equations can be used to describe the same physical phenomenon is unexpected, since this means that Equation 1.14 = Equation 1.13, i.e.,

$$A\left(\frac{K_I}{K_c}\right)^N = Be^{\frac{nK_I}{RTK_c}} \qquad \text{A.1,}$$

where $A = a_1\exp(-E_1/RT)$ and $B = a_2\exp(-E_2/RT)$.[29] Taking the natural log of both sides and solving for K we find that

$$\ln A - \ln B = \frac{nK_I}{RTK_c} - N\ln\left(\frac{K_I}{K_c}\right) \qquad \text{A.2,}$$

so that only for a particular, finite number of K_I's (those that satisfy Equation A.2) are the two laws truly equivalent.

Using literature values [29] of A, B, n and N for abraded soda-lime-silicate glass gives $\ln(A/B) = 33.9$. In Figure A.1 this is plotted along with the right-hand side of Equation A.2 as a function of the "reduced stress intensity," K_r, which we simply define as K_I/K_c, the ratio of applied stress intensity to critical stress intensity. Interestingly, Equation A.2 is never actually satisfied; i.e., the two laws are, strictly speaking, never equivalent.

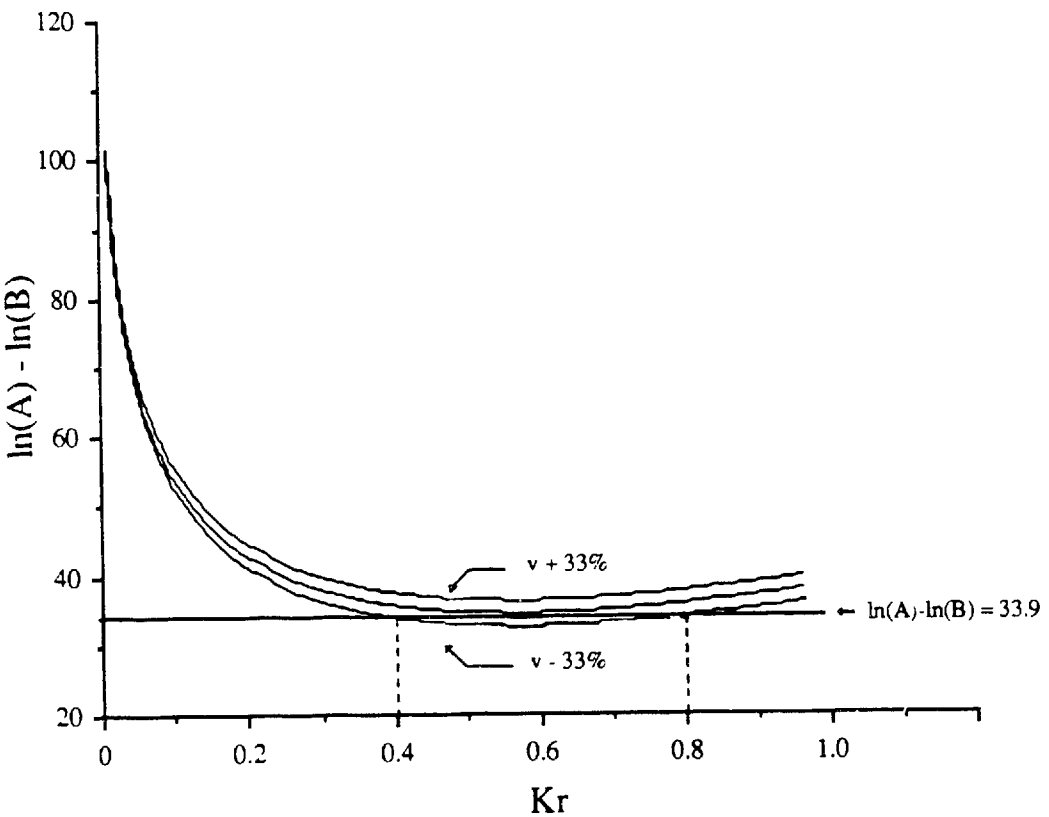

Figure A.1: Equation A.2, plotted as a function of the reduced stress intensity, K_r. The upper and lower bands correspond to an uncertainty in the measured velocity of +/- 30%, respectively.

Experimentally, however, crack velocities are usually determined to within only a factor of about 3. Error bands representing an uncertainty of +/- 33% are, therefore, also plotted in Figure A.1, and we see that, within the experimental uncertainty, there exists a range of stress intensities for which the two laws are indistinguishable. Moreover, this range, from about $K_r = 0.4$ to about $K_r = 0.8$, corresponds to the most conveniently explored range of stress intensities in crack velocity experiments; relative intensities less than 0.4 approach the static fatigue limit, and intensities greater than 0.8 begin to cause spontaneous failure. Therefore, in most of the published literature, both the power and exponential laws of subcritical crack growth appear to describe crack velocity data equally well.

There does exist one example - the static fatigue behavior of optical waveguides - in which an experimental difference between the exponential and power laws has been hinted at. The long-term mechanical stability of these waveguides is an important issue in the practical application of optical communication systems. Therefore, Wang et al[77] and Krause[78] studied the static fatigue behavior of silica at very low loads. While neither study compared the power and exponential laws (they both used the power law to compare their data to literature values of the crack growth exponent, N), they both noted that at long times (low loads) the data seemed to deviate from the power law; failure occurred more rapidly than predicted by a power law extrapolation of the short-time data.

Krause explains this deviation in terms of a different mechanism of failure at long times. However, this deviation can also be explained by the use of an improper subcritical crack velocity function. In Figure A.2, Krause's data, along with a power law fit for silica (N = 16), is plotted. The static fatigue solution for the exponential law, Equation 5.17, is also plotted, using literature values for soda-lime-silicate glass for the

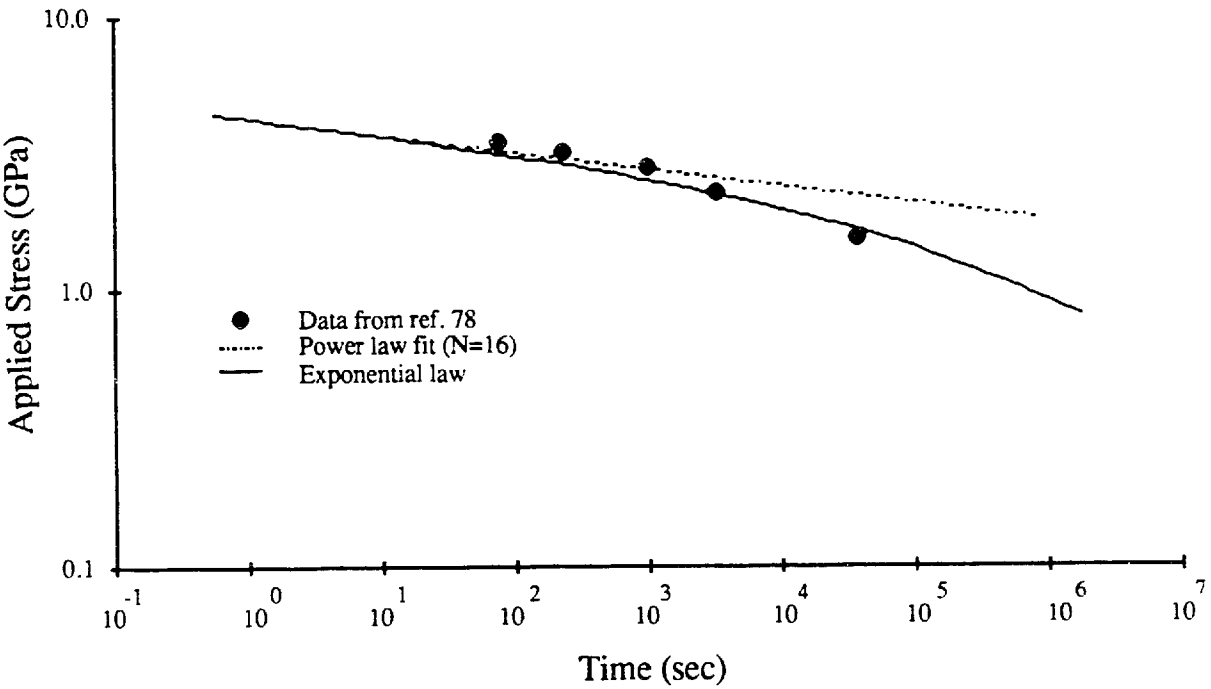

Figure A.2: Static fatigue behavior (data points) from reference 78 for silica optical wave guides. The upper and lower curves represent a fit of the power law with N = 16 (silica) and the exponential law, using soda-lime-silicate values for the constants, respectively.

constants.[29] The curvature in the data is well accounted for by employing the exponential law.*

While this agreement does not rule out the possibility of a second failure mechanism, it does suggest that the concept must be examined in closer detail. In addition, the agreement lends support to the physical "correctness" of the exponential law, which is based on a chemical model of stress corrosion,[26] versus the power law, which is derived from an empirical fit of experimental data.

* The lack of a quantitative fit is due to the use of constants for soda-lime-silicate glass instead of for fused silica. It is expected that the fit would be improved if constants for silica were employed.

Appendix B. Bend Test Fixtures

All fracture testing reported in this thesis was done using a standard Instron Testing machine* using a crosshead speed of 0.2"/min. The testing fixtures were both custom built for these experiments, and are described in the following sections.

B.1 Four-Point Fixture

Most samples in this thesis were 6 mm diameter rods which were broken in uniaxial tension, using a four-point bend fixture with 1" inner and outer spans, for a total span length of 3". The fixture, shown in Figure B.1, is based on the design in Military Standard 1942(MR).[78]

Since the fixture had to be removed after each experiment, an easy, accurate alignment system was needed to ensure that the moment lengths would be equal so that the load distribution was as ideal (flat) as possible. By placing grooves (a) in the base plate (b), the fixture was easily aligned; the upper bearings (c) were simply inserted into the grooves and the crosshead lowered until contact with the upper plate (d) was made. Double-stick tape on the top of the upper plate then fixed the plate to the crosshead. Leveling of the base and upper plates was ensured by a cylindrical bearing (e) which was placed between the base plate and stand (f). Using this set-up, fracture almost always occurred between the inner (top) bearings.

---

* Instron Corp., Canton Mass.

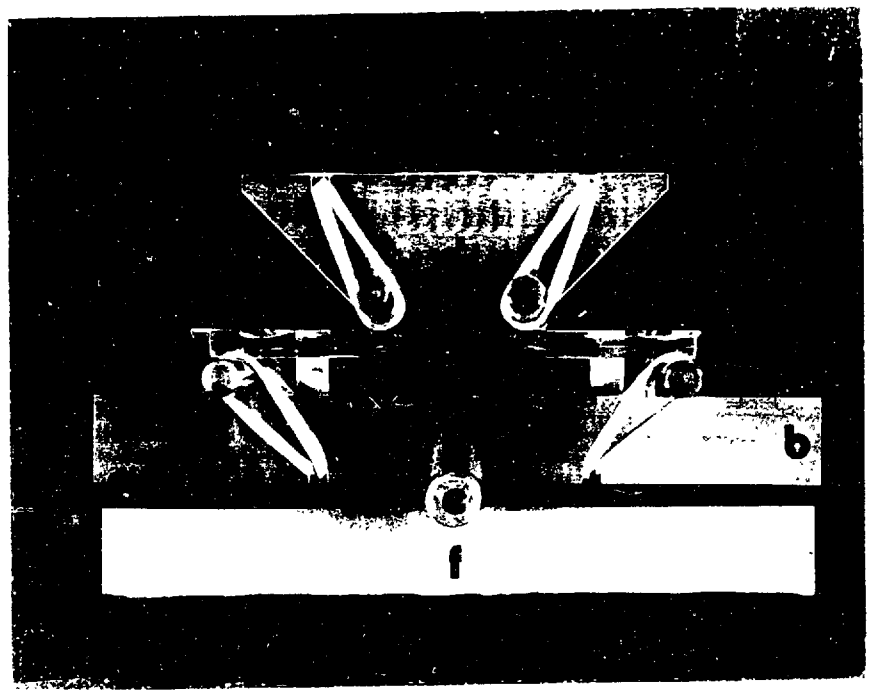

Figure B.1: Four-point bend fixture used for uni-axial strength testing. (See text for datailed description.)

Frictional effects, which can be quite significant in bend-tests,[80] arise upon loading when the sample strains are resisted by the frictional force at the sample/bearing interface. For a rod in bending, for example, the bottom surface would like to elongate during loading. High friction between the rod and bearing may resist this motion, however, producing an effective compressive stress, which makes the sample appear stronger than it actually is. This was accounted for in our test fixture by holding the bearings against posts with loose rubber bands (g). This allowed the bearings to move, out on the tension side and in on the compression side. (While the bearing movements change the inner and outer span lengths, the resulting change in moment has been shown to be minimal[80])

Two final sources of error - twisting and wedging stresses - can be shown to be negligible using the present sample/fixture combination. Twisting, which occurs when a net torque is set up in the sample from skewed loading, is not a concern for cylindrical samples, since the loading is done essentially at a point as opposed to across a line, as in rectangular samples. Wedging stresses arise from the singularity in stress distribution directly beneath the loading bearing. It has been shown[81] that at a short distance from the loading point, an excess tensile stress is present on the tensile side of a sample. The magnitude of this stress is dependent on the rod diameter to outer span ratio. For our 6 mm diameter rods and 1" outer span length, this correction turns out to be only about 0.5 % of the total applied stress.

B.2. Ring-on-Ring Fixture

For studies using controlled flaws, flat plates are preferable since they can be conveniently indented with a Vickers diamond. Twisting stresses, edge effects, and flaw orientation become a problem when such plates are broken in uniaxial tension. A ring-on-ring, biaxial stress test fixture was therefore constructed for the plate samples. The fixture is shown in Figure B.2. The rings are composed of a set of 0.1" dia stainless steel ball bearings placed in concentric grooves (a) in the bottom (base) plate and (b) on the top (loading) plate. The top and bottom grooves are 9 and 18 mm dia, respectively. The use of loose ball bearings for supports helps eliminate frictional effects, as discussed above. To ensure that the top and bottom plates are parallel, the loading plate is attached to the loading rod (d) by a ball bearing and high viscosity grease (e).

The following equation was used for calculating the stress felt on the tensile side of the sample:

$$\sigma_{max} = \frac{3P}{4\pi t^2}\left[\, 2\,(1+\nu)\,\ln\left(\frac{a}{b}\right) + \frac{(1-\nu)(a^2-b^2)}{a^2}\,\frac{a^2}{R^2}\right] \qquad \text{B.1}$$

where P is the loading force, t is the sample thickness, a and b are the radii of the outer and inner rings, respectively, R is the sample radius, and ν is Poisson's ratio.[82] For the square, 1" x 1" samples used, the radius was estimated as one-half the average of the edge and diagonal lengths.[82]

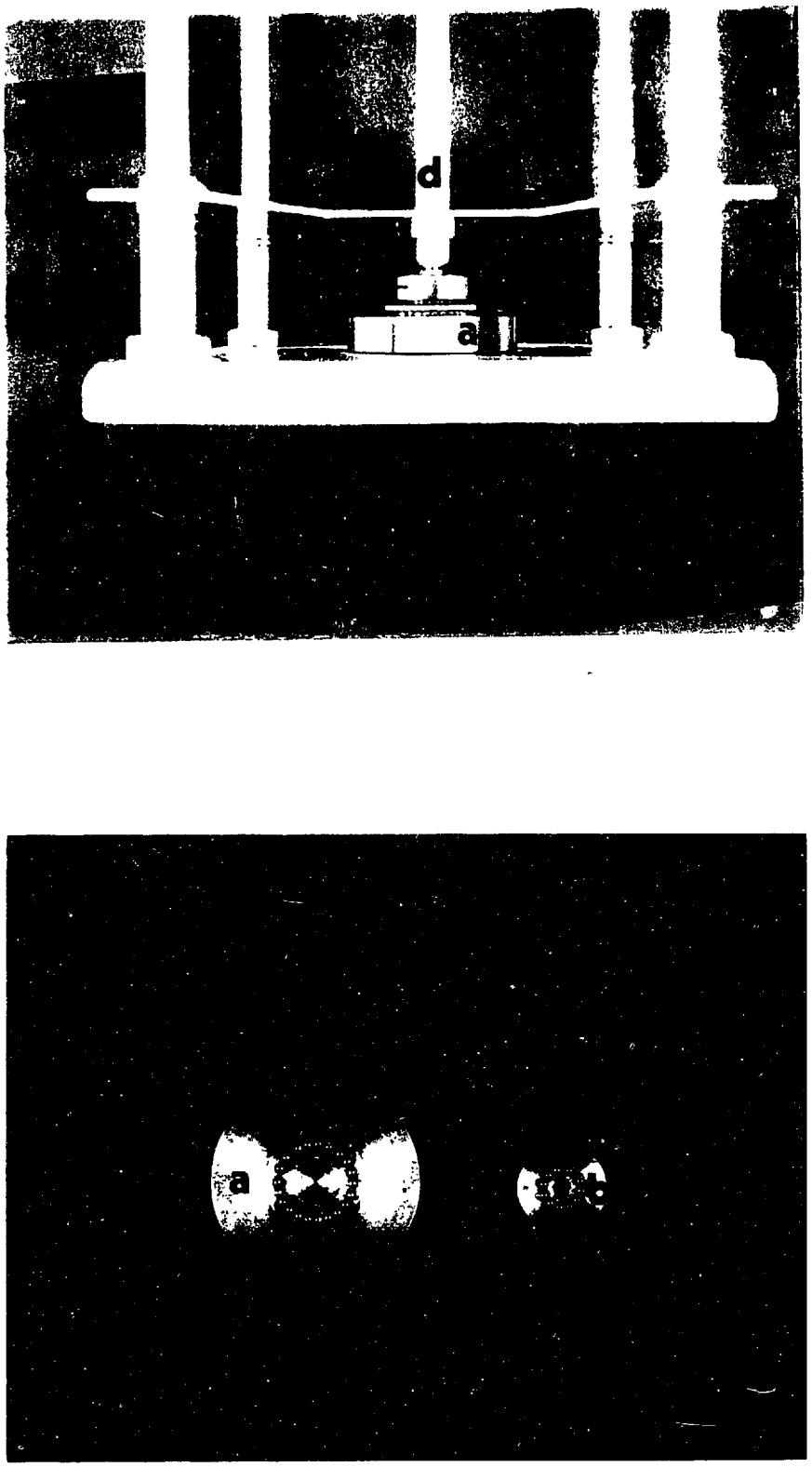

Figure B.2: Ring-on -ring bend fixture used for bi-axial strength testing. (See text for detailed description.)

Appendix C. Sol-Gel Derived Oxynitride Coatings

We have demonstrated the ability to increase the strength of glass by flaw healing; but to take full advantage of such increases in strength, we need coatings which are inherently hard and abrasion resistant so that these improvements can be preserved. Oxynitrides offer outstanding promise for serving as such abrasion resistant coatings* for two reasons. First, the mechanical properties of oxynitride glasses are enhanced in direct proportion to their nitrogen content. These improvements result from the replacement of two-coordinated oxygen atoms with three-coordinated nitrogen atoms, thereby providing a much more strongly bonded network.[83] In particular, the hardness of bulk oxynitride glasses has been reported in the literature to be equal to that of sapphire at only 10 at% nitrogen.[84] We regard this as particularly significant, since sapphire is twice as hard (on the Knoop scale) as silica; and silica is the hardest component of the common dirt which is largely responsible for the degradation of glass strength after leaving the filling line.

Second, sol-gel techniques have been shown to provide a convenient method for producing oxynitride coatings. Conventionally, oxynitride coatings have been made on silicon for electronics applications,[85,86, e.g.] by nitriding thermally grown oxide films at high temperatures (900 - 1000 °C) in ammonia. These films, however, generally exhibit depleted nitrogen contents in the bulk of the film as a result of the difficulty of diffusing the reacting species through the nitrided surface.[85] To overcome this problem, sol-gel

* Oxynitride coatings are also highly resistant to oxidation,[38,39] which also makes them promising candidates for improving the fatigue characteristics of coated glass. This possibility will not be explored here, however.

processing techniques, wherein a porous silica film is applied to the silicon substrate and then nitrided, have been attempted.[39, 87-89] The average decreases in diffusion length provided by the porous films have been successful in producing homogeneous thin films (~500Å when fired) on silicon substrates.

The following sections describe experiments directed towards producing abrasion resistant oxynitride coatings, and an initial survey of the abrasion resistance provided to fused silica substrates by such coatings.

C.1 Nitridation of Thicker Films on Glass

To provide significant abrasion resistance, it is envisioned that protective coatings would need to be much thicker than 500 Å. In addition, since nitridation of thermal oxide is assisted by the faster rate of nitridation of silicon versus its oxide, the use of a glass substrate could alter the kinetics of nitrogen incorporation. As a result, the objectives of the following work were to produce thicker oxynitride coatings, to alter the processing parameters to optimize the homogeneity of nitrogen incorporation, and to investigate the effects of using glass (as opposed to silicon) substrates.

C.1.1 Experimental Procedures

Coating solutions were prepared by partially hydrolyzing TEOS, 2 moles water per mole TEOS, at pH=3, diluted 1:1 in ethanol. The solutions were reacted under argon in a water bath maintained at 20 C.

Both fused silica glass and silicon were used as substrates. The silicon substrates were polished, n-type, (100) wafers. They cleaned using the standard "RCA Procedure," and then spin-coated under argon by placing about 1 ml of solution on the substrate and spinning at 4400 rpm for one minute. The coated samples were allowed to dry, still in argon, under a heat lamp. The silica samples were cleaned by rinsing in methylene chloride, acetone, and ethanol. They were dip-coated, under argon, by withdrawing from the TEOS solution at 5 mm/min. Both coating techniques produced 2400 to 2800 Å coatings. The coatings were further dried by aging in air or by heating to various temperatures (from 20 C to 1000 C) for one hour. By placing directly into a hot furnace at 1050 C, the samples were then fired under flowing ammonia for one hour.

Auger sputter depth profiling,* operated at a base pressure of less than 1×10^{-7} Torr, was used to determine the homogeneity of the nitrogen distribution. An electron current of about 100 na/cm^2, accelerated to 3 KeV, was used; while the Ar^+ ions for sputtering were accelerated to 4 KeV and rastered over a 2 mm x 2 mm area.

C.1.2 Results

An initial set of samples was prepared by drying silica- and silicon-coated samples at 200 C before firing in ammonia. After firing, coatings on the silica substrates were coherent and relatively featureless; those on the silicon substrates were extensively cracked. Both samples had comparable thicknesses after firing, so that this difference is not a result of differences in shrinkage. The difference could also be due to differences in

---

* Physical Electronics model 590 Scanning Auger Microprobe.

CTE caused by enhanced nitridation at the metal/oxide interface on silicon. This is unlikely, however, since interfacial nitrogen build-up was not detected in either sample. Rather, it is likely that a lack of hydrated oxide on the cleaned silicon significantly reduces the ability of the coating to react with and adhere to the substrate. (This result is also consistent with the discussion in Section 4.1.)

The nitrogen profile of both samples is shown in Figure C.1. The nitrogen content is slightly reduced in the coating on silicon. This small difference is probably due to an increase in the silicon signal resulting from the cracks in the coating. Neither profile shows a buildup of nitrogen at the coating/substrate interface, indicating that the faster rate of nitridation of silicon versus its oxide plays little role in the nitridation of these thicker coatings. While this could be due to the high sputter rate (260 Å/min) used, the extent of buildup has previously been shown to be greatly reduced for thick (>500 Å) coatings.[90]

The most significant feature of the nitrogen profiles in the drastic inhomogeneity on the nitrogen content. Within a few hundred Angstroms of the surface, the nitrogen content is greatly reduced. This stands in contrast to the nitrogen profiles, Figure C.2, of a sample which was not dried at 200 C before nitriding. Such a large difference in the nitrogen profiles with a small difference in the drying process was unexpected. In order to examine more closely the effects of coating processing on nitrogen incorporation, samples were prepared with a variety of drying schedules. These schedules are shown in Table C.1. In Figure C.3, the differences in nitrogen incorporation resulting from the various drying schedules are shown. In general, lower drying temperatures enhance the homogeneity of nitrogen incorporation.

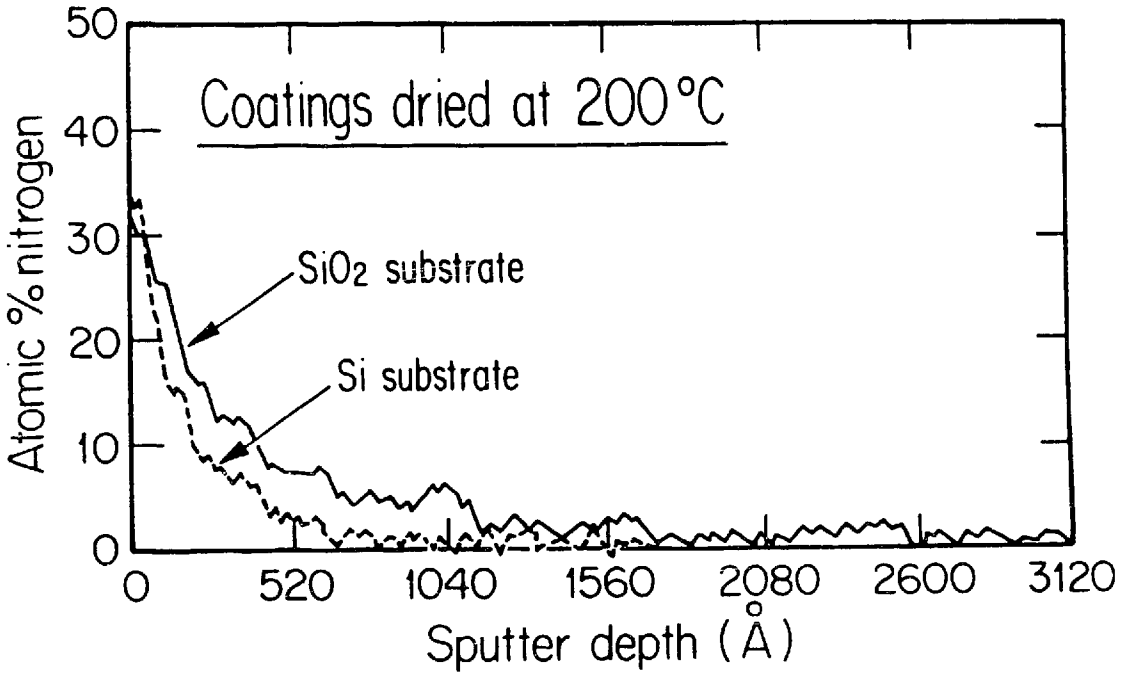

Figure C.1: Auger sputter depth profiles of nitrogen in 200°C-dried ammoniated silica coatings on silica and silicon.

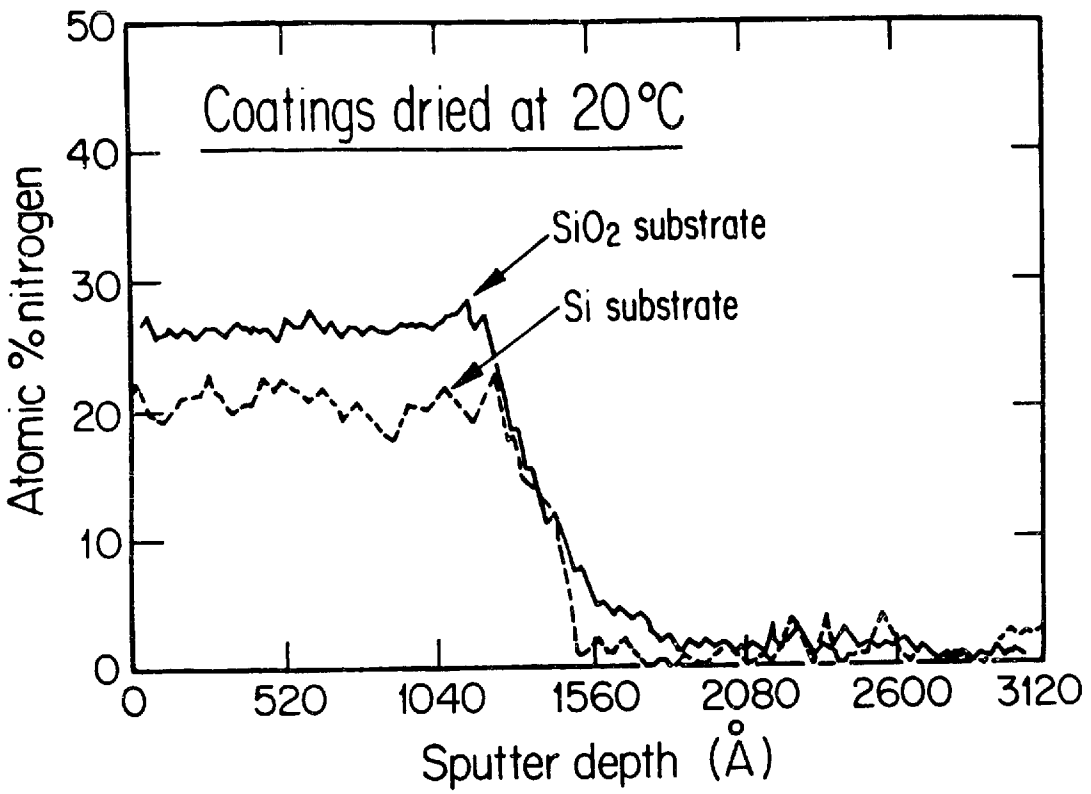

Figure C.2: Auger sputter depth frofiles of nitrogen in ammoniated silica coatings on silica and silicon, dried at 20 C.

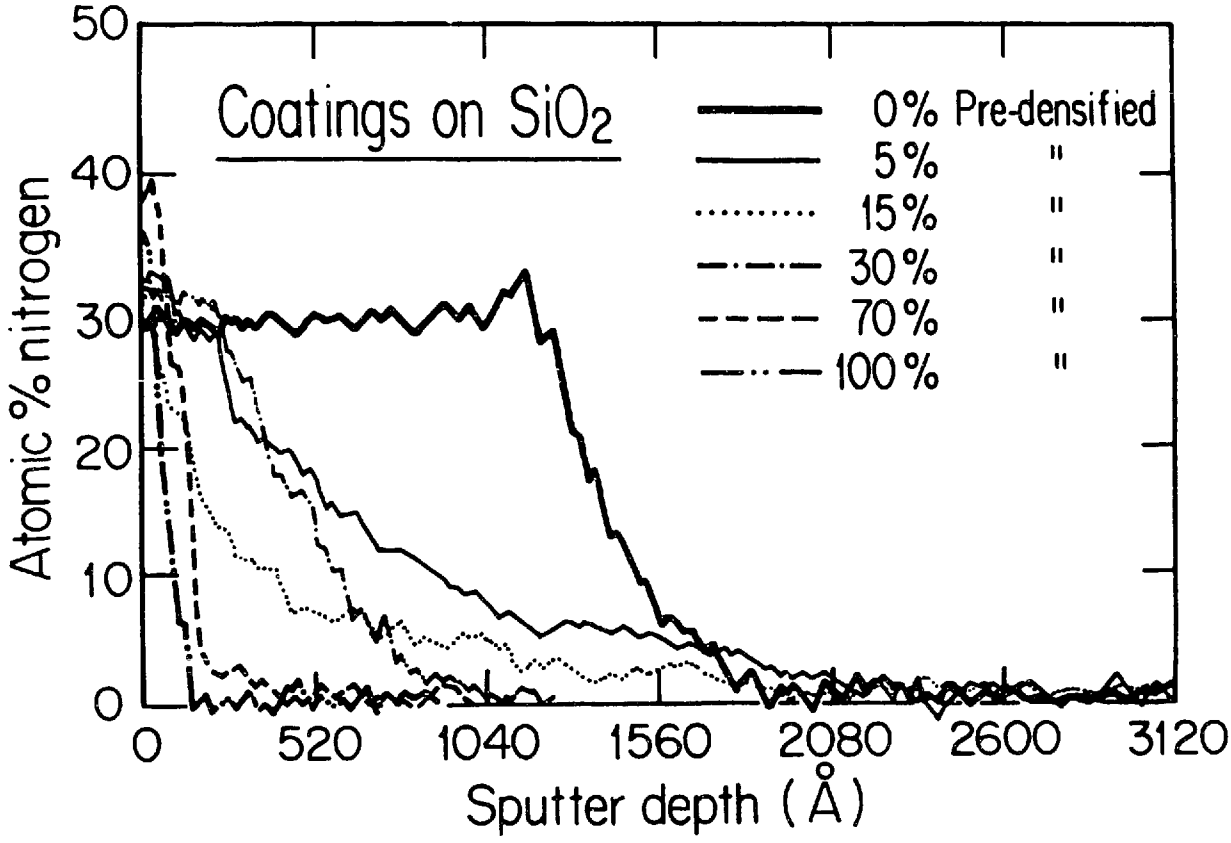

Figure C.3: Auger sputter depth profiles of nitrogen in ammoniated silica coatings on silica, dried with a range of drying schedules. (See Table C.1 for drying details.)

C.1.3 Discussion

During heat treatment, sol-gel fil[illegible]e expected to undergo a variety of changes. Most significantly, condensation between silanol groups or between silanol and alkoxide groups is accelerated. These reactions increase the density of siloxane bridges as well as the overall film density, and decrease the residual carbon content. Changes in the unfired film density with different drying treatments are listed in Table C.1. While the increased density with extent of drying is expected to hinder nitrogen incorporation, one would not expect this to become noticeable until relatively high drying temperatures. The small changes in prefiring density (~5%) obtained by simply aging the coatings would not be expected to change so severely the nitrogen incorporation. Moreover, these coatings were extremely porous; firing in air at 1000 C to densify them resulted in 60 % shrinkage. Coating densification seems feasible as an explanation only if the porosity becomes closed with very mild drying treatments. This is unlikely, however, as closing the porosity at such low temperatures would result in film bloating from the large amount of trapped gas. This was not observed.

Densification occurs rapidly at 1050 C in unnitrided regions of the TEOS coating. Once nitrided, however, densification is negligible at this temperature. If the rate of nitridation were increased during the initial moments of firing, then sintering might be stopped before the coating densifies, allowing more nitrogen incorporation. It is therefore possible that even small increases in the rate of nitridation in undried, carbon containing samples could have a large effect on the depth of nitrogen incorporation.

The nitridation reaction between ammonia and a silanol group,

$$H_3N: + Si\text{-}OH \cdots\cdots> H_2N\text{-}Si + H_2O \qquad C.1$$

Table C.1: Fraction of total densification and carbon content of TEOS coating after various drying treatments.

Drying Schedule	% Predensified	[C]/[Si]
None	0	0.90
Aged in air 1 week	~5	0.59
Aged and fired to 200 C	10	0.43
Aged and fired to 400 C	30	0.22
Aged and fired to 750 C	70	0.16
Aged and fired to 1000 C	100	------

is very similar to that between ammonia and an alkoxide group,

$$H_3N: + Si\text{-}OR \cdots\cdots> H_2N\text{-}Si + HOR \qquad C.2$$

The main differences are the steric demands of the alkoxide group, the polarity of the Si-O bond, the ability of the leaving group, -OH or -OR, to stabilize a negative charge, and the increased basicity of alkoxides over hydroxides, leading to the formation of a more stable product. The first two differences both favor reaction with the hydroxide. The magnitudes of these effects, however, are likely to be small; the nucleophile is small; and alkyl groups are only weakly electron-donating. The third effect, stability of the leaving group, favors reaction with the alkoxide. Its magnitude is also expected to be small, however, since both hydroxide and alkoxide are poor leaving groups. The basicity of the alkoxide is likely to be the most important of the four effects; the energy released by the reprotonation of the alkoxide anion is greater than that released by the reprotonation of the hydroxide ion.

In addition to the factors considered above, the potential for reducing the nitridation product, ethanol, provides another factor which should strongly favor reaction with the alkoxide-containing species (and hence nitrogen incorporation). In the highly reducing, high temperature ammonia atmosphere, the complete reduction of ethanol,

$$OH\text{-}CH_2CH_3\,(g) \cdots\cdots\cdots\cdots> CO\,(g) + CH_4\,(g) + H_2\,(g) \qquad C.3,$$

is possible. Based on bond rupture and formation changes - one H-O, one C-C, and one C-H bonds broken at the expense of the creation of one H-H bond - the net enthalpy change for Reaction C.1 is -189 Kcal/mole.[91] In addition, the formation of three moles of gas at constant temperature and pressure results in an entropy increase,

$$\Delta S = \int_{V_1}^{V_3} R\, d\ln V = R\ln(\frac{3}{1}) = 2.15 \times 10^{-3}\ \text{Kcal/}^{o}\text{K mole} \qquad \text{C.4,}$$

so that the net driving force, $\Delta H - T\Delta S$, may be as high as 192 Kcal/mole. It is likely that this extra driving force for reaction with the alkoxide increases the rate and extent of reaction with the undried coatings. In fact, Brinker has reported that carbon removal is noticeably promoted by the presence of ammonia, "...giving evidence for the proposed reaction between ammonia and =M-OR groups."[92]

We have shown that relatively thick (>1200 Å when fired) homogeneous silicon oxynitride coatings can be produced by the high temperature nitridation of porous silica films, that minimizing drying of the coating is important for full nitridation, and that the substrate composition (silica or silicon) has little effect on the nitrogen incorporation. It does not appear, so far, that there is any intrinsic limit to the thickness of coatings which can be homogeneously nitrided, although the sensitivity of the homogeneity to drying schedules indicates that minor processing changes become important as coating thicknesses increase. Presently, the thickness of homogeneous oxynitride films is limited only by the ability to produce thick, crack-free precursor coatings. In the next section, the abrasion resistance of these coatings will be evaluated and discussed.

C.2 Abrasion Resistance of Oxynitride Coatings

Routine, quantitative determination of the abrasion resistance of thin coatings is often very difficult. Most quantitative techniques rely on measuring the weight loss of a coating after a certain standard abrasion treatment. Unfortunately, a 3000 Å thick coating

on a 1 cm^2 substrate only weighs about .01 μgm; measuring weight loss therefore requires a tremendously sensitive scale. Indentation techniques are also difficult to apply, since, for even the smallest loads (a few grams), 90 % or more of the indenter penetrates into the substrate. In this case, one must rely on extrapolations, which are often inaccurate, to zero load.[93]

Recently, Ludwig and Stoner[94] developed a convenient, quantitative method for evaluating the abrasion resistance of thin, hard coatings. Their method is based on a quantity they call the abradance, γ, which is a scaling factor which relates the area, a, of pits formed on a surface when a volume, V, of abrasive impacts that surface:

$$V\gamma = a \qquad \text{C.5.}$$

γ is essentially the inverse of hardness. A large γ material is easily abraded, while a small γ material is not. (It is important to notice the γ is a material constant only for constant abrasive material and abrasion technique.)

The advantage of using γ to characterize the abrasion resistance of a material is that it is a property which is quite amenable to experimental determination. Following Ludwig and Stoner's derivation,[94] if a sample already has an area fraction, α, of pits formed and a unit area, A, of unpitted surface, then the addition of an extra volume, dV, of abrasive, will create a newly pitted area $(1-\alpha)\gamma dV$. Thus, as long as α is small enough that the pits don't impinge,

$$Ad\alpha = (1-\alpha)\gamma dV \qquad \text{C.6.}$$

Defining the specific volume, v, of abrasive as the total abrasive volume per unit area allows Equation C.6 to be integrated to give

$$\alpha = 1 - e^{-\gamma v} \qquad \text{C.7.}$$

The abradance of a material can now be determined (for a particular abrasive and mode of bombardment) by measuring α. Experimentally, this can be done conveniently if we pass a beam of light through a sample and assume that the pits scatter the beam in direct proportion to their area, so that the light intensity, I, measured on the other side of the sample is simply

$$I = I_o(1-\alpha) \qquad \text{C.9,}$$

where I_o is the incident intensity. Substitution of Equation C.9 into C.8 gives, upon rearrangement,

$$\gamma = (1/v)\ln(I_o/I) \qquad \text{C.10,}$$

so that a plot of $\ln(I_o/I)$ vs. v should be a straight line with a slope of γ.

C.2.1 Experimental Procedures:

Silica slides, 1" x 1" x 1mm, were used as substrate material. The substrates were coated, in the usual manner, using TEOS coatings prepared in the manner described in Section C.1. The coatings were then fired, as described in the preceding section, to produce homogeneous oxynitride coatings. To provide a range of coating thicknesses,

one sample was re-coated with the TEOS solution and fired a second time. Another sample was coated and fired five times.

The samples were abraded, along with an uncoated silica standard plate, by slowly dropping 30 grit silicon carbide* powder through a 1 m long, 2 cm diameter tube. The powder was dropped in 5 ml batches, between which light transmission measurements were made. The light transmission was measured using the apparatus shown in Figure C.4. Columnated light from a halogen lamp was passed through a band pass filter (485nm) and defocussed to 2 cm diameter onto the sample surface; a photodetector with a gain of 10^6 was placed on the other side of the glass sample. By placing the entire apparatus inside a light-tight case, accurate, reproducible data were obtained.

C.2.1 Results and Discussion

The transmission data for the three coated samples and the silica standard are presented in Figure C.5, and the abradances, obtained from the slope of the $\ln(I_o/I)$ vs. v plots, are shown in Table C.2. Interestingly, the uncoated silica slide shows the best resistance to abradance (low γ), and the **thinner** oxynitride coatings are more abrasion resistant than the thicker ones. Since all of the oxynitride coatings were fully nitrided, the differences must be a result of microstructural, as opposed to chemical, differences. Specifically, the coatings are probably not dense.

---

* Obtained from Norton Co., Worcester MA

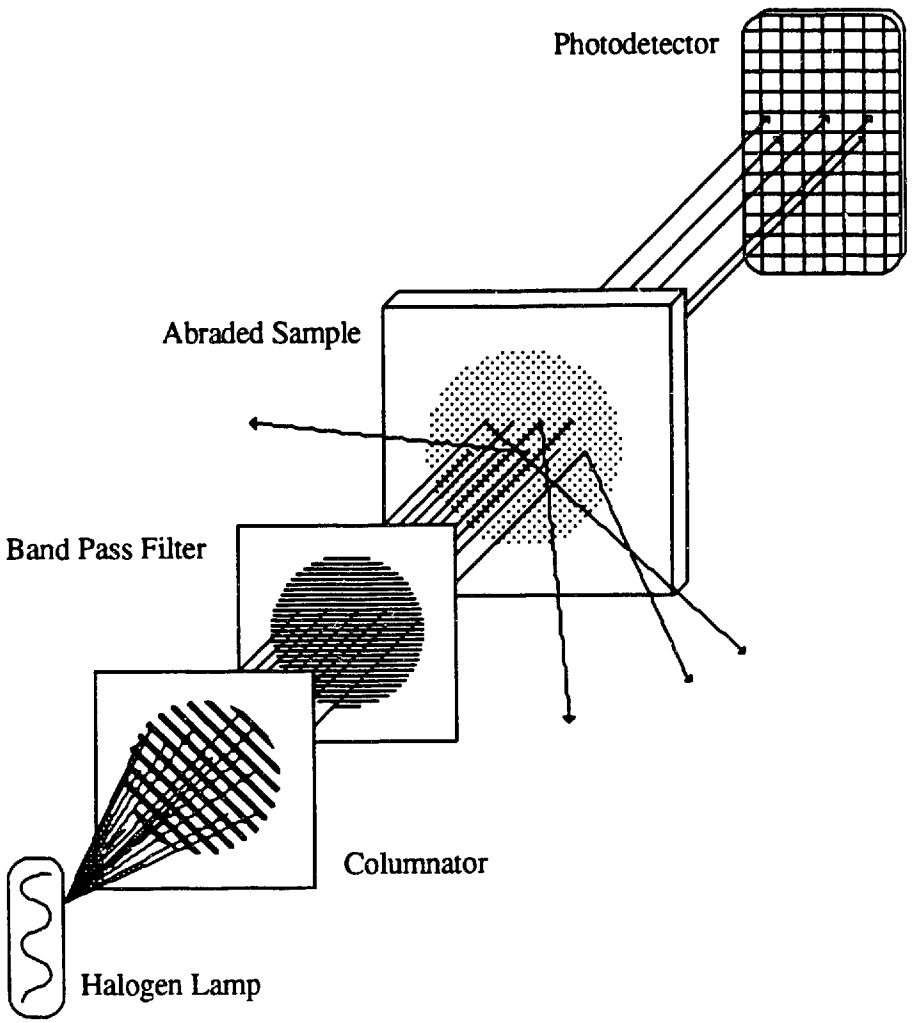

Figure C.4: Schematic drawing of apparatus used to determine abradance of coated and uncoated silica slides. (Suu text for details.)

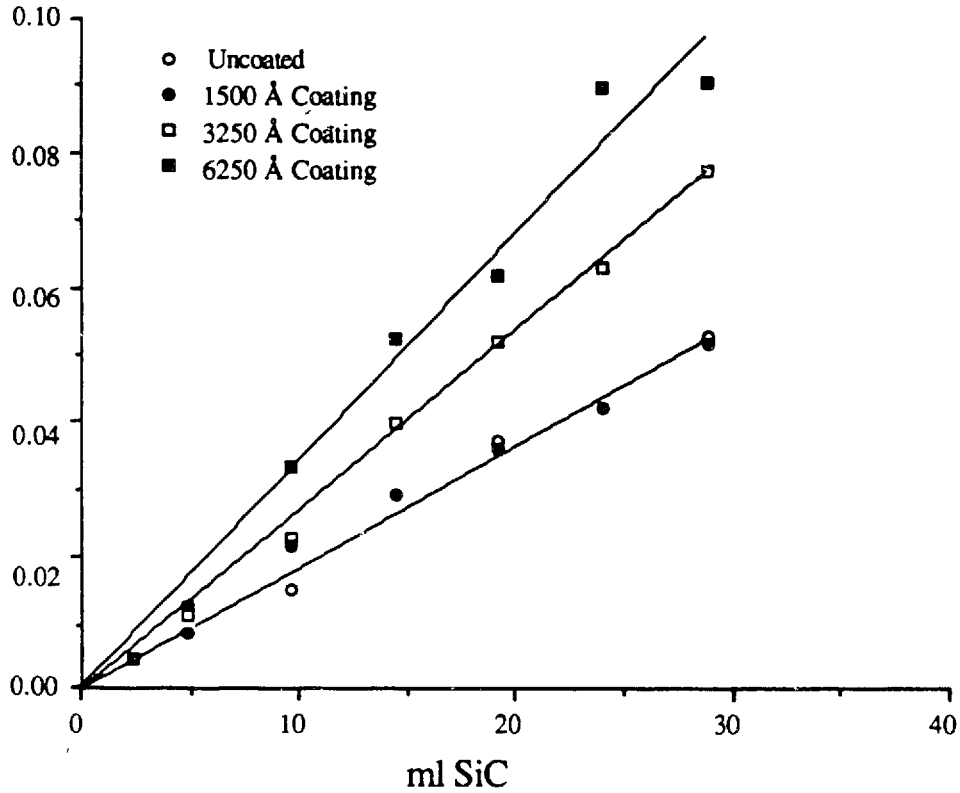

Figure C.5: Abrasion resistance data for oxynitride coated silica plates.

Table C.2: Abradance values for silica and siliconoxynitride-coated silica, as determined from slopes in Figure C.5.

Coating Thickness (Å)	Abradance (cm^{-1}) +/- one std. dev.
0	1.7 +/- 0.1
1500	1.9 +/- 0.3
3250	2.4 +/- 0.4
6250	3.2 +/- 0.2

In the preceding section, we discussed the nitridation of these films. In order to explain the results, we hypothesized that the fully nitrided coatings are homogeneous because early nitrogen incorporation prevents the coating from fully densifying. The abradance data are certainly consistent with this explanation. It thus appears that there exists a competition between nitridation and densification; To fully nitride TEOS coatings, the nitrogen must be incorporated before the coatings densify; once nitrided, however, the coatings can't densify unless heated to much higher temperatures. It would be interesting to densify the porous, nitrided coatings at higher temperatures and then test the abrasion resistance.

Finally, just what effect a porous but nitrided coating will have on the ultimate strength of coated glass is unclear. Even though the abradance is diminished by the porosity, it is possible that the presence of a "hard but crushable" coating may be quite beneficial, as flaws produced in the coating may not be transferred to the substrate. In this case, the coating could act as a "mini impact absorber" which attenuates the energy reaching the substrate when struck by an abrasive.

References

1. A.C. Robinson, *Science*, 233 (1986) 25.

2. H. Dislich *Angew. Chem. Internat. Ed.*, 10 (1971) 363.

3. B.J.J. Zelinski and D.R. Uhlmann, *J. Phys. Chem. Sol.*, 45 (1984) 1069.

4. D.R. Uhlmann et al, *Mat. Res. Soc. Symp. Proc.*, 32 (1984) 125.

5. H. Dislich, *J. Non-Cryst. Sol.*, 63, (1984) 237.

6. D.R. Uhlmann, "Wet Chemical Synthesis of Glasses and Ceramics; Opportunities and Critical Needs," Presented at the 40th anniversary of the Basic Science Division of the Japanese Ceramic Society, 1985.

7. J.D. Mackenzie, *J. Non-Cryst. Sol.*, 48 (1982) 1.

8. H. Dislich and P. Hinz, *J. Non-Cryst. Sol.*, 48 (1982) 11.

9. H. Dislich, *Coatings on Glass*, vol.2, p.251, Academic Press, 1984.

10. H Schroeder, *Physics of Thin Films; Advances in Research and Development*, vol.5, p.87, Academic Press, 1969.

11. M. Nogami and Y. Moriya, *J. Non-Cryst. Sol.*, 37 (1980) 191.

12. T. Kawaguch et al, *J. Non-Cryst. Sol.*, 63 (1984) 61.

13. L. L. Hench in *Science of Ceramic Chemical Processing*, ed. by L.L. Hench and D.R. Ulrich, John Wiley and Sons, 1986, p.52.

14. S. Sakka and Y. Komiya, *J. Non-Cryst. Sol.*, 48 (1982) 31.

15. K. D. Keefer, *Mat. Res. Soc. Symp. Proc.*, 32 (1984) 15.

16. C. J. Brinker et al, *J. Non-Cryst. Sol.*, 48 (1982) 47.

17. L. C. Klein and G.J. Garvey, *Mat. Res. Soc. Symp. Proc.*, 32 (1984) 33.

18. R. Aelion et al *J. Amer. Chem. Soc.*, 72 (1950) 5705.

19. W. D. Kingery, H. K. Bowen, and D. R. Uhlmann, *Introduction to Ceramics*, John Wiley and Sons, 1976, p. 71.

20. R. K. Brow and C. G. Pantano, *Appl. Phys. Lett.*, 48 (1986) 27.

21. S. K. Gupta and C. G. Audain, *Proc. SPIE*, 469 (1984) 179.

22. H. Schmidt, et al, U. S. Pat. 4,374,696 (1983).

23. W. D. Kingery, H. K. Bowen, and D. R. Uhlmann, *Introduction to Ceramics*, John Wiley and Sons, 1976, p. 784.

24. A. A. Griffith, *Philos. Trans. R. Soc.*, A221 (1920) 163.

25. C. E. Inglis, *Trans. Inst. Nav. Arch.*, 55 (1913) 219.

26. T. A. Michalske and S. W. Freiman, *J. Amer. Ceram. Soc.*, 66 (1983) 284.

27. S. M. Wiederhorn *J. Amer. Ceram. Soc.*, 50 (1967) 407.

28. S. M. Wiederhorn and L. H. Boltz, *J. Amer. Ceram. Soc.*, 53 (1970) 543.

29. J. E. Ritter et al, *Phys. Chem. Glass.*, 27 (1986) 65.

30. J. E. Ritter in *Fracture Mechanics of Glass*, vol. 4, ed. by R. C. Bradt et al (1978) p. 667.

31. W. D. Kingery, H. K. Bowen, and D. R. Uhlmann, *Introduction to Ceramics*, John Wiley and Sons, 1976, p.611

32. J. Jonas, *Science of Ceramic Chemical Processing*, ed. by L.L. Hench and D.R. Ulrich, John Wiley and sons, 1986, p.65.

33. B. D. Fabes et al, Unpublished Work.

34. T. S. Wei, *Adv. Ceram. Mat.*, 1 (1986) 237.

35. J. Poole, Private Communication, July 2, 1986.

36. Glass Science by R. H. Doremus, John Wiley and Sons, 1973, p. 310.

37. T. A. Schwattz, Masters Thesis, Massachusetts Institute of Technology (1977) p. 23.

38. S. P. Muraka et al, *J. Electrochem. Soc.*, 126 (1979) 996.

39. R. K. Brow and C. G. Pantano, *Appl. Phys. Lett.*, 48 (1986) 27.

40. C. M. Drum and M. J. Rand, *J. Appl. Phys.*, 39 (1968) 4458.

41. D. J. D. Thomas, *Phys. Status Solidi*, 20 (1967) 131.

42. N. B. Sokolov et al, *Fizaka i Khim. Stekla*, 8 (1982) 29.

43. H. P. Williams, *Glass Tech.*, 16 (1975) 34.

44. R. D. Southwick et al, *Thin Solid Films*, 77 (1981) 41.

45. M. W. Davis et al, to be published in *J. Amer. Ceram. Soc.*

46. A. G. Evans and R. W. Davidge, *Glass Tech.*, 12 (1971) 148.

47. V. R. Howes, *Glass Tech.*, 15 (1974) 148.

48. H. Ohta et al, *Jap. J. Appl. Phys.*, 14 (1975) 1685.

49. W. E. Swindlehurst and B. Cantor, *Glass Tech.*, 19 (1978) 14.

50. J. B. Ward, *Glass Tech.*, 16 (1975) 68.

51. G. L. Smay, *J. Non-Cryst. Sol.*, 38 & 39 (1980) 359.

52. W. B. Beck and M. H. Hodge, *Laser Focus E/O*, 20 No. 12 (1984) 90.

53. S. Sakka and K. Kamiya, *J. Non-Cryst. Sol.*, 48 (1982) 31.

54. A. I. A. Abdel-Latif et al, *Inter. J. Fracture*, 13 (1977) 349.

55. J. J. Mecholsky et al, *J. Amer. Ceram. Soc.*, 57 (1974) 440.

56. C. J. Brinker, "Sol-Gel Derived Thin Films: Critical Issues," Presented at the NATO Conference, Sept., 1986, d'Agde, France.

57. R. K. Iler, *The Chemistry of Silica*, John Wiley and Sons, 1979, pp. 630-638.

58. *bid*, p. 644.

59. *Ibid*, p.645.

60. C. J. Brinker et al in *Science of Ceramic Chemical Processing*, ed. by L. L. Hench and D. R. Ulrich, p. 37.

61. B.R. Lawn and M.V. Swain, *J. Mat. Sci.*, 10 (1975) 113.

62. B. R. Lawn, "The Indentation Crack as a Model Surface Flaw," from *Fracture Mechanics of Glass*, vol. 5, ed. by Bradt et al (1983) p. 1.

63. B. R. Lawn et al, *J. Amer. Ceram. Soc.*, 63 (1980) 574.

64. D. B. Marshall et al *J. Mat. Sci.*, 14 (1979) 2225.

65. B. R. Lawn and E. R. Fuller *J. Mat. Sci.*, 10 (1975) 2016.

66. T. A. Micahlske and E. R. Fuller Jr., *J. Amer. Ceram. Soc.*, 68 (1985) 586.

67. J. T. Hagan, *J. Mat. Sci.*, 14 (1979) 462.

68. A. Arora et al, *J. Non-Cryst. Sol.*, 31 (1979) 415.

69. J. C. Newman Jr. and I. S. Raju, NASA Technical Paper 1578, 1979.

70. B. R. Lawn et al, *J. Amer. Ceram. Soc.*, 58 (1975) 428.

71. D. B. Marshall and B. R. Lawn, *J. Mat. Sci.*, 14 (1979) 2001.

72. Y. W. Mai and B. R. Lawn, *J. Amer. Ceram. Soc.*, 70 (1987) 289.

73. B. D. Fabes, unpublished work January, 1987.

74. D. R. Uhlmann, Private Communication, May 17, 1987.

75. R. K. Iler, *The Chemistry of Silica*, John Wiley and Sons.

76. H. Schmidt, *Mat. Res. Soc. Symp. Proc.*, 32 (1984) 327.

77. T. T. Wang et al, *J. Appl. Polym. Sci.*, 23 (1979) 887.

78. J. T. Krause, *J. Non-Cryst. Sol.*, 38-39 (1980) 497.

79. U. S. Army MIL-STD-1942(MR), 21 November 1983.

80. J. E. Ritter and R. D. Wilson, *Trans. Amer. Soc. Lubrication Eng.* 18 (1974) 130.

81. R. G. Hoagland et al, *J. Amer Ceram. Soc.*, 59 (1976) 189.

82. J. E. Ritter et al, *J. Non-Cryst. Sol.*, 38-39 (1980) 419.

83. R. E. Loehman in *Treatise on Materials Science and Technology*, vol. 26 (1985) 120.

84. D. R. Messier and A. Broz *J. Amer. Ceram. Soc.*, 65(1982) C-123.

85. T. Ito et al, *J. Electrochem. Soc.*, 127 (1980) 2053.

86. Y. Hayafuji and K. Kajiwara, *J. Electrochem. Soc.*, 129 (1982) 2102.

87. R. K. Brow and C. G. Pantano, *J. Amer. Ceram. Soc.*, 70 (1987) 9.

88. D. M. Haaland and C. J. Brinker, *Mat. Res. Soc. Symp. Proc.*, 32 (1984) 123.

89. C. G. Pantano et al, *Science of Ceramic Chemical Processing*, ed. by L.L. Hench and D.R. Ulrich, John Wiley and Sons, 1986, p.161.

90. R. P. Vasquez and A. Madhukar, *J. Appl. Phys.*, 59 (1986) 972.

91. *Organic Chemistry vol. 3*, by J. Hendrickson, D. Cram, and G. Hamnmond, McGraw-Hill Book Co., 1970, p.

92. C. J. Brinker, *J. Amer. Ceram. Soc.*, 65 (1982) C-4.

93. K. Enke, *Thin Solid Films*, 80 (1981) 227.

94. M. A. Ludwig and R. B. Stoner, . *Appl. Phys.*, 60 (1986) 4277.

95. W. D. Kingery, H. K. Bowen, and D. R. Uhlmann, *Introduction to Ceramics*, John Wiley and Sons, 1976, p. 609.

96. G. W. Scherrer, "Drying Gels: II. Film and Flat Plate," preprint of article to appear in *J. Non-Cryst. Sol.*

97. G. W. Scherrer, *J. Amer. Ceram. Soc.*, 68 (1985) 216.

98. G. W. Scherrer et al, *J. Non-Cryst. Sol.*, 72 (1985) 369.

99. T. A. Gallo and L. C. Klein, *J. Non-Cryst. Sol.*, 82 (1986) 198.

100. G. W. Scherrer, "Drying Gels: I. General Theory," preprint of article to appear in *J. Non-Cryst. Sol.*